POLITECNICO
MILANO 1863

SCUOLA DI INGEGNERIA INDUSTRIALE
E DELL'INFORMAZIONE

Microdosimetric Insights: Neutron Capture Enhancement and RBE Variability in Proton Therapy

Tesi di Laurea Magistrale in
Nuclear Engineering - Ingegneria Nucleare

Author: **Gabriele Mentasti**

Student ID: 223158
Advisor: Prof. Stefano Luigi Maria GIULINI CASTIGLIONI AGOSTEO
Co-advisors: Dist. Prof. Anatoly Rozenfeld, Dr. Linh Tran, Prof. Susanna Guatelli
Academic Year: 2024-25

Abstract

This thesis investigates the microdosimetric and radiobiological aspects of proton therapy using Geant4 simulation toolkit. It focuses on Neutron Capture Enhanced Particle Therapy (NCEPT) and the variation of relative biological effectiveness (RBE) along the proton Bragg Peak (BP). This work is motivated by the necessity to establish a link between physical dose distributions and their biological effects, with the aim of improving the assessment of radiation quality and its impact on cancer treatment.

The model of the silicon on insulator (SOI) microdosimeters were used in this work to simulate the energy deposited by proton beams into the micron sized sensitive volumes (SVs). In this work, the detector position, beam size, detector's converters, target materials generating neutrons such as tungsten were investigated in details. The beam energies as well as detector configurations were varied to enhance the production of high Linear Energy Transfer (LET) particles from neutron capture reaction while minimizing the dose to healthy tissue.

The results show that by adding ^{10}B, either uniformly distributed in the SVs, or by placing the $^{10}B_4C$ converter on top of the detector SVs, leading to a dose increase via the $^{10}B(n,\alpha)^7Li$ reaction. This effect was most pronounced for larger beam sizes, which delivered a higher thermal neutron flux to the detector. Both detector configurations exhibited clear peaks in the microdosimetric spectra, and higher dose-mean lineal energy were obtained, indicating more intense, localized biological damage within the volume of interest. The RBE values were observed to increase sharply at the distal edge of the BP correlated with the rising LET values which results in a LET hot spot beyond the physical dose maximum. However, an RBE of 1.1 is currently assumed and implemented for proton therapy, which may negatively impact treatment outcomes. This work emphasizes the importance of accurately deriving RBE values to better reflect the biological effects and improve patient safety.

This thesis highlights the need for experimental validation of simulation results and recommends the integration of microdosimetric data and variable RBE models into clinical treatment planning. Such approach enables more accurate delivery of the biological dose

while reducing risks to healthy tissues. Microdosimetry was demonstrated to be a powerful tool for pratical application of particle therapy.

The results demonstrate that NCEPT can precisely provide a boost dose to the tumor. Overall, this work encourages the move toward biologically optimized planning in hadron therapy.

Keywords: microdosimetry, proton therapy, neutron capture, RBE

Abstract in lingua italiana

Questa tesi indaga gli aspetti microdosimetrici e radiobiologici della proton terapia utilizzando il toolkit di simulazione Geant4. L'attenzione è rivolta alla Neutron Capture Enhanced Particle Therapy (NCEPT) e alla variazione della relative biological efficiency (RBE) lungo il picco di Bragg dei protoni. Il lavoro è motivato dalla necessità di stabilire un legame tra le distribuzioni di dose fisica e i loro effetti biologici, con l'obiettivo di migliorare la valutazione della qualità della radiazione e del suo impatto nel trattamento dei tumori.

Il modello dei microdosimetri silicon on insulator (SOI) è stato impiegato per simulare l'energia depositata dai fasci di protoni nei volumi sensibili (SVs) di dimensioni micrometriche. In questo studio sono stati analizzati in dettaglio la posizione del rivelatore, le dimensioni del fascio, i convertitori del rivelatore e materiali bersaglio capaci di generare neutroni, come il tungsteno. Sono state inoltre variate le energie dei fasci e le configurazioni dei rivelatori, al fine di incrementare la produzione di particelle ad alto Linear Energy Transfer (LET) provenienti dalle reazioni di cattura neutronica, minimizzando al contempo la dose ai tessuti sani.

I risultati mostrano che l'aggiunta di ^{10}B, sia distribuito uniformemente nei volumi sensibili, sia posto sotto forma di convertitore di $^{10}B_4C$ sopra i volumi sensibili, comporta un incremento della dose tramite la reazione $^{10}B(n,\alpha)^7Li$. Questo effetto risulta più evidente per fasci di dimensioni maggiori, che forniscono un flusso più elevato di neutroni termici al rivelatore. Entrambe le configurazioni del rivelatore hanno mostrato picchi distinti negli spettri microdosimetrici e valori più alti di energia lineale media di dose, indicando un danno biologico più intenso e localizzato all'interno del volume di interesse. I valori di RBE sono stati osservati crescere bruscamente al margine del picco di Bragg, in correlazione con l'aumento del LET, che genera un hot spot di LET oltre il massimo della dose fisica. Tuttavia, nella pratica clinica è attualmente assunto e implementato un valore costante di RBE pari a 1,1, il che può avere un impatto negativo sugli esiti terapeutici. Questo lavoro sottolinea l'importanza di derivare valori accurati di RBE per riflettere meglio gli effetti biologici e migliorare la sicurezza dei pazienti.

La tesi evidenzia la necessità di una validazione sperimentale dei risultati delle simulazioni e raccomanda l'integrazione dei dati microdosimetrici e dei modelli di RBE variabile nei sistemi di pianificazione clinica del trattamento. Un tale approccio consente una somministrazione più accurata della dose biologica, riducendo i rischi per i tessuti sani. È stato dimostrato come la microdosimetria rappresenti uno strumento potente per l'applicazione pratica della terapia con particelle.

I risultati dimostrano che la NCEPT può fornire con precisione una dose di boost al tumore. In generale, questo lavoro incoraggia la transizione verso una pianificazione biologicamente ottimizzata nella adroterapia.

Parole chiave: microdosimetria, adroterapia, cattura neutronica, RBE

Contents

Introduction

Radiotherapy is a cornerstone of modern cancer treatment, playing a crucial role in the management of a wide range of tumors. Its primary objective is to deliver a lethal dose of ionizing radiation to tumor cells while minimizing exposure to surrounding healthy tissues. Over the past decades, major innovations in technology and theory, such as the development of intensity-modulated radiotherapy, image-guided techniques, and hadron therapy, have dramatically improved the precision and effectiveness of radiation treatments. Among these, proton therapy and hadron therapy offer key advantages over conventional X-ray therapy: they exploit the unique depth dose distribution of charged particles, characterized by the Bragg peak, which allows for precise dose delivery to the tumor. This results in superior sparing of healthy tissues and critical organs, reduced risk of side effects, and the potential for effective treatment of deep seated or radioresistant tumors. Additionally, the higher linear energy transfer (LET) of heavy ions in hadron therapy leads to more complex DNA damage in cancer cells, which is more difficult to repair. This enhances tumor control, particularly in hypoxic or resistant regions. Despite these achievements, there remains considerable scope for further innovation, particularly in enhancing tumor control and reducing patient side effects.

The complexity of the radiation field and its biological impact at the microscopic scale is a critical challenge in radiotherapy. The biological effectiveness of radiation is not determined only by the absorbed dose, but also by the spatial and stochastic distribution of energy deposition within cells and subcellular structures. This is where microdosimetry becomes essential. Microdosimetry provides the tools and framework to measure and analyze the energy imparted by ionizing radiation in small volumes, comparable to the dimensions of biological cells and their critical targets. By characterizing the distributions of lineal energy and specific energy at these scales, microdosimetry enables a more accurate assessment of the relative biological effectiveness (RBE) of different radiation qualities and treatment modalities. In the context of hadron therapy, which utilizes protons and heavier ions, microdosimetry is particularly important. The unique depth dose profile of charged particles, characterized by the Bragg peak, allows for highly conformal irradiation of tumors. However, the interactions of these particles with tissue and beamline materials

also produce a spectrum of secondary particles, including neutrons, which contribute to the overall radiation field and its biological effects. Understanding and optimizing these mixed fields requires detailed analysis, as the RBE can vary significantly with depth, particle type and tissue characteristics.

This thesis explores an emerging strategy to enhance the therapeutic potential of particle therapy: Neutron Capture Enhanced Particle Therapy (NCEPT). NCEPT [1] [2] seeks to combine the physical precision of charged particle beams with the biochemical selectivity of neutron capture agents, such as ^{10}B, which can be preferentially delivered to tumor cells. During hadron therapy, heavy ions interact with tissue and beamline materials, producing a spectrum of secondary particles, including thermal neutrons. When these thermal neutrons are captured by ^{10}B enriched agents localized within tumor cells, they trigger the neutron capture reaction, resulting in the emission of high LET particles: α particles and ^{7}Li nuclei. These high LET particles deposit their energy over a very short range, causing intense, localized biological damage where the capture agent has accumulated. This dual-action approach offers the potential for significant localized dose amplification within the tumor, while minimizing additional exposure to surrounding healthy tissues. By integrating the physical advantages of hadron therapy with the biochemical targeting of neutron capture agents, NCEPT represents a promising avenue for improving the therapeutic index of particle therapy, especially for tumors that are difficult to treat with conventional modalities.

In this thesis, advanced silicon-on-insulator (SOI) microdosimeters developed by the Centre for Medical Radiation Physics (CMRP, University of Wollongong, Australia) are used to investigate the radiobiological and physical enhancement provided by the presence of thermal neutrons in particle therapy. Monte Carlo simulations with the Geant4 toolkit are used to model particle interactions and energy deposition at the microscopic scale, with a particular focus on the complex radiation fields generated during NCEPT. Through these simulations, this thesis aims to deepen the understanding of how neutron capture agents, such as ^{10}B, selectively delivered to tumor cell, can be exploited to achieve more localized and effective tumor irradiation by harnessing the high LET particles produced in neutron capture reactions. The use of SOI microdosimetry enables a detailed characterization of energy deposition patterns, which is essential for evaluating both the physical and biological impacts of these therapeutic strategies.

The second major focus of this thesis is the study of RBE in proton therapy. While a constant RBE value of 1.1 is typically adopted for treatment planning in clinical practice, this simplification does not fully reflect the true variation of RBE along the proton path, particularly near the Bragg peak where LET increases. In this work, a microdosimetric

analysis is performed to assess as a function of depth in water the changes in RBE, using both established radiobiological models and simulation data. This thesis provides insights that could contribute to more accurate and personalized approaches in proton therapy, aiming to improve tumor control and minimize side effects for patients, by exploring how RBE varies with depth and radiation quality.

The structure of the thesis is as follows:

1. **Proton and Heavy Ion Therapy** : This chapter provides an overview of radiation interactions with matter, focusing on the mechanisms relevant to hadron therapy. It details the physical principles underlying charged particle therapy, including the Bragg peak phenomenon, beam delivery systems, and the production of secondary particles, such as neutrons. This chapter introduces the concept of NCEPT, highlights its potential advantages, and discusses the rationale for integrating neutron capture processes into particle therapy.

2. **Microdosimetry and Radiobiology** : This chapter introduces the fundamental quantities and methodologies of microdosimetry, emphasizing their role in quantifying energy deposition at cellular and subcellular scales. Key radiobiological models, including the linear quadratic model and the microdosimetric kinetic model, are reviewed. The integration of microdosimetric spectra with biological weighting functions is examined, establishing a foundation for linking physical energy deposition to biological effects. In addition, this chapter introduces the Monte Carlo toolkit Geant4 and details its application in simulating radiation transport and interactions for microdosimetric studies.

3. **Detectors and Setup** : This chapter introduces the main types of detectors used in microdosimetry. It begins with an overview of conventional detectors, such as tissue equivalent proportional counters, highlighting their strengths and limitations in replicating the response of biological tissue at the cellular scale. The chapter then focuses on the silicon microdosimeters developed by the CMRP, with particular emphasis on the design, structure and advantages of the Mushroom SOI microdosimeter. Special attention is given to the innovations that make the Mushroom SOI microdosimeter suitable for high resolution microdosimetric measurements and the configurations used in NCEPT.

4. **NCEPT Results and Discussion** : In this chapter the results of Monte Carlo simulations investigating the microdosimetric impact of thermal neutrons in NCEPT are presented and analyzed. The performance of different detector configurations, including standard, boron-doped and $^{10}B_4C$ converter designs, is compared in terms

of neutron detection efficiency and energy deposition. The influence of key parameters, such as beam size, converter thickness, and presence of a tungsten neutron converter, is explored, with an emphasis on optimizing the conditions for enhanced neutron capture effects.

5. **RBE Evaluation along the Bragg Peak** : This chapter is dedicated to the analysis of the spatial variation of RBE along the Bragg peak in proton therapy. Using microdosimetric spectra obtained from Monte Carlo simulations, the chapter investigates how RBE changes with depth in water, considering different detector geometries and physics models. The analysis provides a comprehensive assessment of depth dependent RBE and highlights the importance of accounting for RBE variation in treatment planning for proton therapy.

6. **Conclusions and Future Developments** : The thesis concludes with a summary of the main findings, highlighting the integration of microdosimetric data into treatment planning. Future research directions, including experimental validation and the extension of NCEPT concepts to clinical scenarios, are proposed.

1 | Proton and Heavy Ion Therapy

This chapter provides a brief overview of radiation interactions with matter in the field of hadron therapy and the concept of radiation therapy with charged particles. The focus is on the employment of neutron capture enhanced particle therapy (NCEPT), highlighting its potential advantages over conventional techniques and exploring the enhancement effect induced by the thermal neutrons generated.

1.1. Radiation Interactions

A comprehensive understanding of radiation interactions in matter is crucial for evaluating their biological impact and simulating these processes within a Monte Carlo framework. This thesis focuses primarily on the study of hadrons, particularly protons. Nevertheless, the interaction of these primary particles generates a spectrum of secondary particles, including neutrons, heavy charged particles, fragments, electrons, and photons. The associated interactions must be correctly understood and accounted for. This section presents a detailed analysis of charged hadron interactions, accompanied by an overview of the interaction mechanisms of secondary particles.

1.1.1. Charged Hadron Interactions

Charged hadrons, such as protons, interact with matter through multiple mechanisms as they travel through a material. Their charged nature leads to predominant interactions with atomic electrons and the electric fields surrounding target nuclei. Direct interactions with the nucleus are also possible in what is termed a nuclear interaction. The primary interaction mechanisms for protons can be classified as follows:

1. Electronic Interactions;
2. Elastic Nuclear Interactions;
3. Inelastic Nuclear Interactions.

Electronic Interactions

These interactions can be divided into two main categories: those in which the charged hadron interacts with a single bound electron of the target nucleus, and multiple Coulomb scattering, where the incident hadron approaches the target nucleus and is scattered due to the interaction between their electric fields.

In the first interaction, the charged hadron interacts with a single bound electron of the target atom or molecule, resulting in either electron excitation or atom ionization. This type of interaction constitutes the primary mechanism of energy loss for the charged hadron as it travels through a medium. Electronic interactions with individual electrons can be classified as either inelastic or elastic, depending on different factors. The interaction is considered inelastic if the energy transferred to the electron is sufficient to excite it to a higher energy level within the atom's shell structure or to completely remove it from the atom, resulting in ionization as illustrated in Figure 1.1a. These processes significantly contribute to energy deposition in the medium. Conversely, if the energy transferred is not enough to either ionize the atom or excite the electron to a higher state, the interaction is classified as elastic. In this case, both energy and momentum are conserved, and the electron remains bound to the atom. Unlike inelastic collisions, elastic interactions do not significantly contribute to the hadron's energy loss.

In multiple Coulomb scattering, the incident hadron approaches the target nucleus, and the interaction between their electric fields results in scattering. This electric field interaction can cause the hadron to deviate from its original trajectory with a reduced energy, or it can cause the hadron and the nucleus to be scattered at small angles relative to one another. In this case, only glancing interactions are considered, where the hadron is deflected by a small angle. Since it is a glancing interaction and due to the mass difference between the hadron and the target nucleus, the nucleus typically does not recoil and no secondary particles are produced. Moreover, the small scattering angle implies that the hadron's energy remains unchanged, making multiple Coulomb scattering an insignificant form of energy loss. This interaction is crucial in hadron therapy because it causes the hadron's trajectory to deviate slightly, resulting in beam spreading at depth.

Elastic Nuclear Interactions

Elastic nuclear interactions also occur between the electric fields of the incident hadron and the target nucleus. Unlike multiple Coulomb scattering, which typically results in small angle deflections, elastic nuclear interactions involve more substantial scattering angles. In this case, both the hadron and the nucleus are significantly deflected, leading

to greater energy loss for the hadron.

The total energy and momentum of the system are conserved during the interaction, as the name suggests. The degree of scattering is influenced by the size of the target nucleus, the mass of the incident hadron, and its energy. This form of scattering is more pronounced when lighter nuclei or lighter and more energetic hadrons are involved. Elastic nuclear interactions do not produce high LET particles from the nucleus. However, the scatter can significantly alter the path of lighter hadrons as displayed in Figure 1.1b.

Inelastic Nuclear Interactions

When a hadron overcomes the Coulomb barrier and interacts directly with the target nucleus, inelastic nuclear interactions occur. These collisions transfer energy to the nucleus, resulting in significant changes to both the hadron and the nucleus itself. During this process, the hadron's energy and trajectory may change, while the nucleus is often elevated to an excited state. To return to stability, the nucleus releases this excess energy by ejecting secondary particles that are important to consider. A representation of this is illustrated in Figure 1.1c.

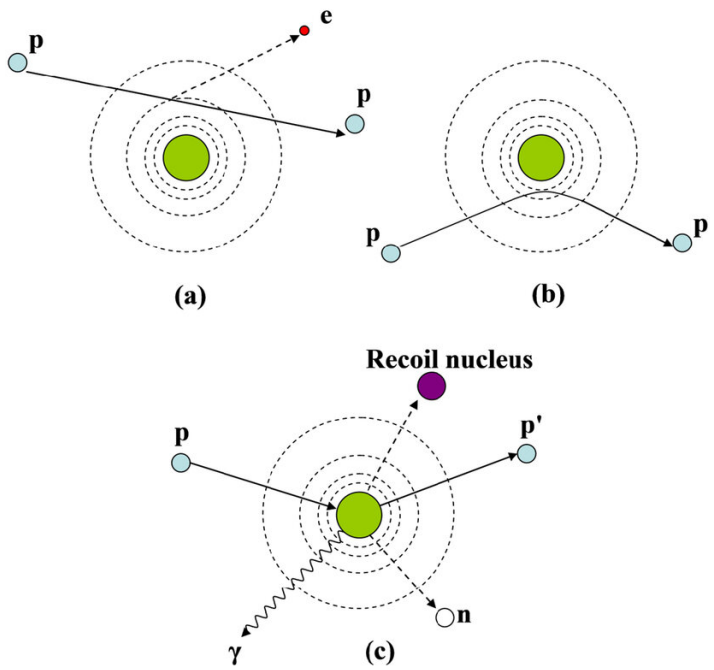

Figure 1.1: Schematic illustration of proton interaction mechanisms: (a) electronic interaction, (b) elastic scattering with nucleus, (c) inelastic nuclear interaction [3].

The resulting products generally possess higher LET compared to the original hadron.

These high LET particles can cause significant biological damage. However, neutrons and gamma photons generated during these interactions are also of concern. Due to their long path lengths, these secondary particles can travel beyond the Bragg peak. In cases where the incident hadron is sufficiently large, fragmentation of the hadron itself can occur. This process produces two or more secondary products through direct interaction with the target nucleus.

Nuclear Spallation Reaction

Nuclear spallation reaction is a high energy inelastic nuclear interaction that occurs when energetic particles, typically protons with energies exceeding 50 MeV, strike a heavy atomic nucleus causing it to emit lighter particles and leaving behind a residual nucleus that is lighter than the original target. The process involves two distinct stages: first, an intranuclear cascade where the incident particle undergoes direct reactions with nucleons inside the target nucleus, creating high energy secondary particles and leaving the nucleus in an excited state; second, a nuclear de-excitation or evaporation phase where the excited nucleus relaxes by emitting low energy neutrons, protons, alpha particles, and other light particles. When a high energy proton bombards a heavy atomic nucleus such as tungsten or lead, approximately 20 to 30 neutrons are expelled from each nucleus, making this process highly efficient for neutron production. Additional information on spallation can be found in [4].

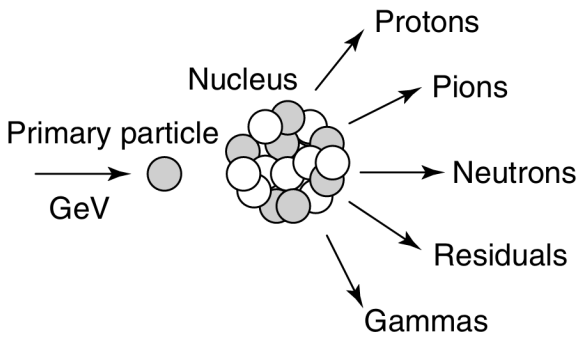

Figure 1.2: Typical secondary particle production in a particle–nucleus interaction [4].

Spallation reactions can be used to produce neutron fluxes with a high energy proton beam on a thick, heavy metal target. The energetic cost of producing spallation neutrons is approximately six times lower than that of neutrons produced via nuclear fission, and the process offers superior control capabilities because the accelerator beam can be turned off to immediately stop neutron production. In this work, tungsten was used to promote spallation due to its properties as a spallation target material [5]. Tungsten is

well suited for spallation applications because of its high atomic number, which maximizes the efficiency of neutron production according to the relationship between atomic mass and neutron yield. The collision of protons with tungsten nuclei throws off a collection of high energy neutrons through the spallation process. The selection of tungsten as the spallation material is based on several advantages that make it superior to other heavy metal alternatives [6]. Tungsten exhibits excellent thermal properties, including a high melting point and high thermal conductivity, which are essential for withstanding the intense energy deposition during spallation reactions [5].

1.1.2. Neutron Interactions

As neutral hadrons, neutrons interact with matter in different ways compared to charged particles. Although neutrons are electrically neutral, they possess a magnetic moment, spin, and a non zero internal charge distribution. These properties allow weak electromagnetic interactions with electrons; however, such interactions are considered negligible. The predominant interactions between neutrons and matter occur through direct interactions with the nucleus of an atom. These can be categorized into three primary mechanisms.

In elastic scattering, the neutron interacts with the target nucleus without altering its internal structure. Energy and momentum are conserved, and the neutron may be either deflected by the nuclear field or absorbed and re-emitted. Part of the neutrons energy is transferred to the nucleus, causing it to recoil. The amount of energy transferred depends on the neutron initial energy, recoil angles and the relative size of the ion. The neutron continues on its path with reduced energy, while the recoil nucleus deposits energy in the medium.

In inelastic scattering, the neutron collides with the nucleus and excites it to a higher energy state. The nucleus can then return to a stable state by emitting secondary radiation such as photons, neutrons, or charged particles:

$$n + {}^{A}_{Z}X \rightarrow n' + {}^{A}_{Z}X^{*} \rightarrow n' + {}^{A}_{Z}X + \gamma \tag{1.1}$$

where ${}^{A}_{Z}X^{*}$ is the excited nucleus. This process results in a loss of energy for the neutron, which is deposited in the medium through the secondary particles emitted. Both inelastic and elastic scattering are the main interactions for high energy neutrons.

At lower neutron energies, especially for thermal energies (0.025 eV), neutron capture becomes more probable. The neutron is absorbed by the nucleus, forming a compound nucleus in an excited state. The nucleus then stabilizes by emitting photons, neutrons or

charged particles:

$$n + {}^{A}_{Z}X \rightarrow {}^{A}_{Z}X^{*} \rightarrow {}^{A}_{Z}X + \gamma \tag{1.2}$$

For example, in the case of thermal neutron capture by ^{10}B:

$$n + {}^{10}\mathrm{B} \rightarrow {}^{11}\mathrm{B}^{*} \rightarrow {}^{7}\mathrm{Li} + \alpha + \gamma \tag{1.3}$$

Also in this case the neutrons energy is transferred indirectly to the surrounding medium via the secondary particles generated.

1.1.3. Electron Interactions

As electrons are the predominant secondary particle species produced as charged hadrons traverse matter, it is essential to understand and consider their interaction properties. Like charged hadrons, electrons can excite and ionize atoms through electromagnetic interactions since they are negatively charged. However, due to their considerably lower mass, electrons are much more deflected when interacting with the Coulomb field of atomic nuclei. This deflection can result in the emission of a photon to conserve the momentum, a process known as Bremsstrahlung. The probability of Bremsstrahlung increases with the atomic number of the medium and the kinetic energy of the electron, making it particularly relevant in high Z materials. In addition, when an electron encounters the positron, a positively charged particle of the same mass, annihilation may occur. This results in the complete conversion of their rest mass into energy, typically producing two photons of 511 keV emitted in opposite directions. This process is the basis for positron emission tomography (PET), a technique used in diagnostic nuclear medicine.

1.1.4. Photon Interactions

Photons are uncharged and as such do not continually lose energy as they traverse matter. Instead, they interact discretely and their energy is deposited in the medium through secondary particles produced by these interactions. There are four distinct interaction pathways for photons, each governed by the energy of the photon and the material properties of the medium [7].

The photoelectric effect occurs when a photon interacts directly with a bound electron. In this case, the photon is completely absorbed and the electron is ejected from the atom. The kinetic energy of the ejected photoelectron is given by:

$$E_k = h\nu - E_b \tag{1.4}$$

where $h\nu$ is the photon energy and E_b is the binding energy of the electron. This interaction is dominant at low photon energies and is more probable in high Z materials.

Compton scattering is similar to the photoelectric effect in that the photon interacts with an electron and causes ionization. However, in this case the photon transfers only part of its energy to the electron and is scattered at an angle with reduced energy. This process dominates at intermediate photon energies. The relationship between the scattered photon energy and the scattering angle θ is given by the Compton equation:

$$E' = \frac{E}{1 + \frac{E}{m_e c^2}(1 - \cos\theta)} \tag{1.5}$$

Pair production is possible when the photon energy is equal to or greater than twice the rest mass of an electron (1.022 MeV). In the presence of a nucleus, the photon may disappear and an electron-positron pair is created. The excess energy is shared as kinetic energy between the two particles. The positron will eventually annihilate with an electron, producing two 511 keV photons. The cross-section for pair production increases with atomic number and photon energy.

In Rayleigh scattering, the photon interacts with the atom as a whole, without transferring energy to it. The photon is scattered at small angles without changing its energy. The deflection is elastic, and no ionization or excitation occurs. This interaction is relevant only at low photon energies and in high-Z materials.

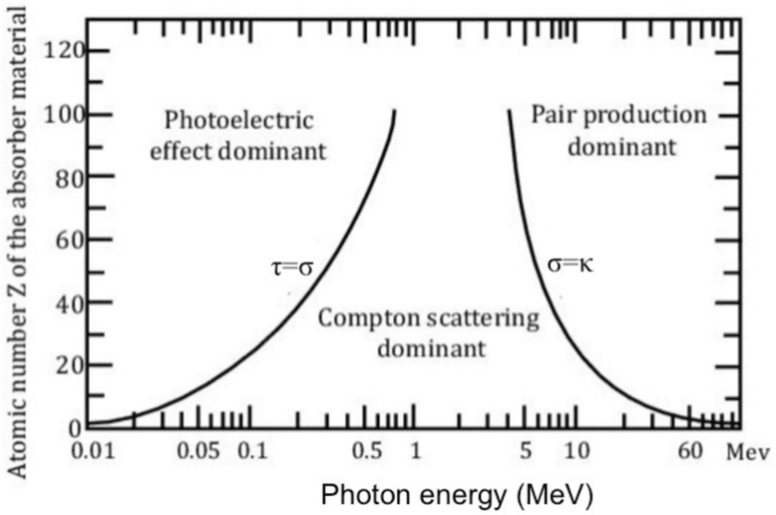

Figure 1.3: Probability of a photon interaction depends on the energy of the photon and the atomic number of the material.

1.2. Hadrontherapy

Radiation therapy is the medical use of ionizing radiation for the treatment of tumours, aiming to deliver radiation to cancer cells to destroy them while minimizing the dose to healthy tissues. In conventional radiation therapy, X-rays are used to damage cells by exploiting the biological effects of radiation, both through direct interaction with molecular bonds of cellular species and via the generation of chemically reactive species, such as free radicals. These free radicals can diffuse and interact destructively with cellular structures.

Hadrontherapy represents a significant advancement in external beam radiation therapy. It offers highly conformal dose distributions that better spare healthy tissues, thanks to the benefits of the Bragg peak. The concept of using heavy charged particles for therapeutic purposes was first proposed in 1946 by Robert R. Wilson at the Lawrence Berkeley Laboratory (LBL) [8]. The strength of hadrontherapy lies in the distinctive physical and radiobiological characteristics of charged hadrons, which enable superior dose conformity. These particles have a well defined range in tissue, depositing little energy at shallow depths and reaching a maximum, the Bragg peak, just before coming to rest.

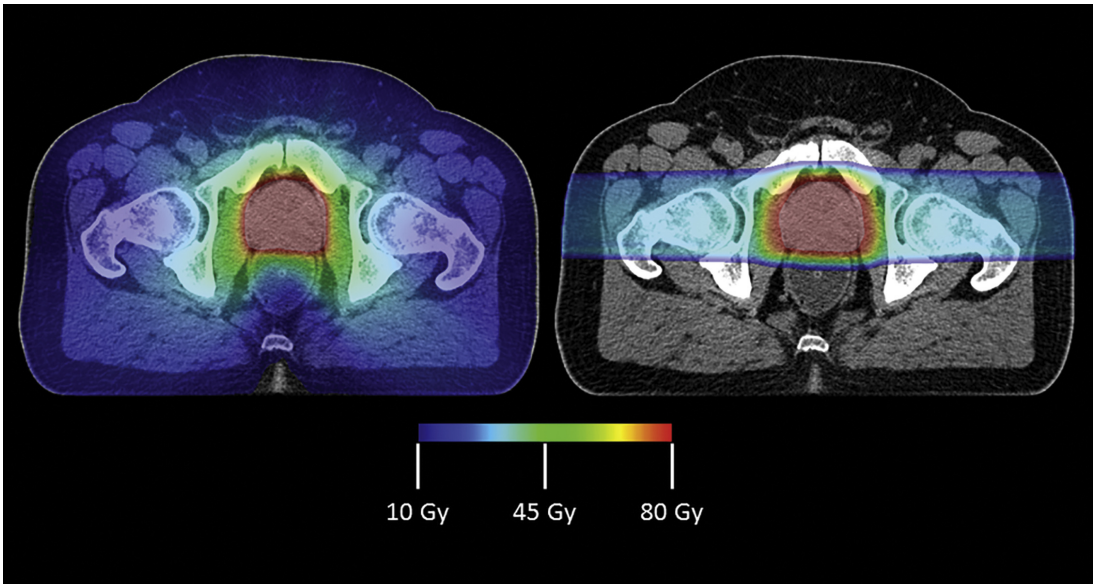

Figure 1.4: Comparison of intensity-modulated radiation therapy (left) vs proton beam therapy (right) for prostate cancer. [9]

By varying the energy of the hadrons, the Bragg peak can be positioned at specific depths within the patient, thereby allowing precise targeting of the tumour volume. Using

multiple converging beams, it is possible to superimpose several Bragg peaks within the tumour, which intensifies the dose where it is most needed. This depth-dose profile contrasts with that of X-rays, which deposit maximum energy near the surface or just below it. A comparison of dose distributions from photon based radiotherapy and carbon ion therapy is presented in Figure 1.4, highlighting the reduced irradiation of normal tissues with carbon ions.

The presence of the Bragg peak is mainly due to electromagnetic interactions that charged hadrons undergo continuously as they traverse matter. These interactions lead to the excitation or ionization of atomic electrons, and at lower energies, near the end of the range of the particle, elastic collisions with target nuclei become significant. This enables effective treatment of deep seated tumours. Another key advantage of protons is that beyond the Bragg peak, no primary radiation dose is delivered apart from a minimal dose from secondary particles and nuclear fragments. This represents a clear advantage over X-rays, allowing for greater sparing of critical organs or tissues located just beyond the tumour. It becomes evident how hadrontherapy enables effective tumour irradiation while reducing damage to healthy tissues, both at the beam entrance and beyond the distal edge of the dose curve, as illustrated in Figure 1.5.

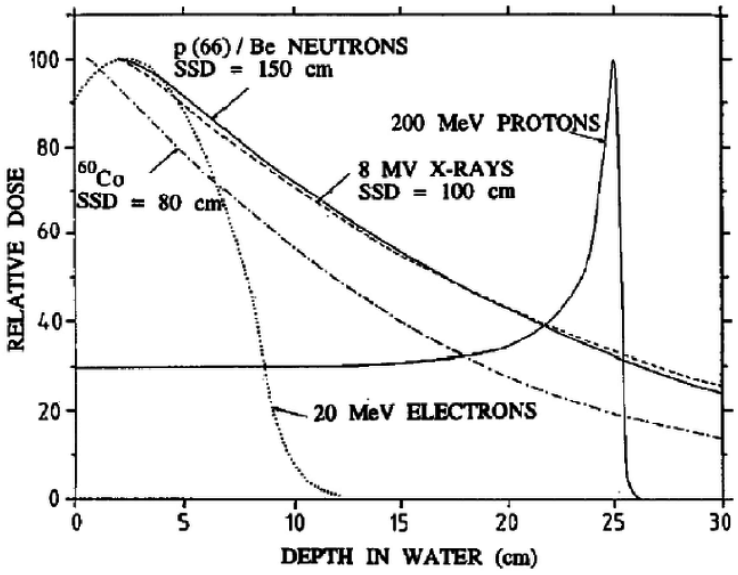

Figure 1.5: Comparison of how different kind of radiations deposit energy in a water phantom.

1.2.1. Beam delivery systems

It is important to note that Figure 1.5 does not represent a realistic clinical treatment plan. In practice, radiotherapy is never performed using a single beam, as this would result in excessive dose to shallow tissues and could lead to complications. Instead, in hadrontherapy, the beam energy is modulated to smooth out the steep energy gradient around the Bragg peak, creating what is known as the spread out Bragg peak (SOBP). This extended dose distribution allows the full tumour volume to be uniformly irradiated. Beam delivery techniques can be categorized into passive and active systems, each with distinct characteristics in terms of dose distribution, complexity, and secondary particle production.

Passive delivery techniques, which have been the most widely used in clinical settings [10], achieve lateral spreading of the beam through a combination of materials designed to produce a flat beam profile with constant flux and range. Typically, a dual scattering foil setup is employed to generate a uniform dose over the desired treatment area. Depth modulation is then achieved using a rotating modulator wheel [11], which superimposes multiple Bragg peaks of different energies to construct the SOBP as shown in Figure 1.6. The beam is collimated and shaped differently according to each patient, while the penetration depth is adjusted using a bolus.

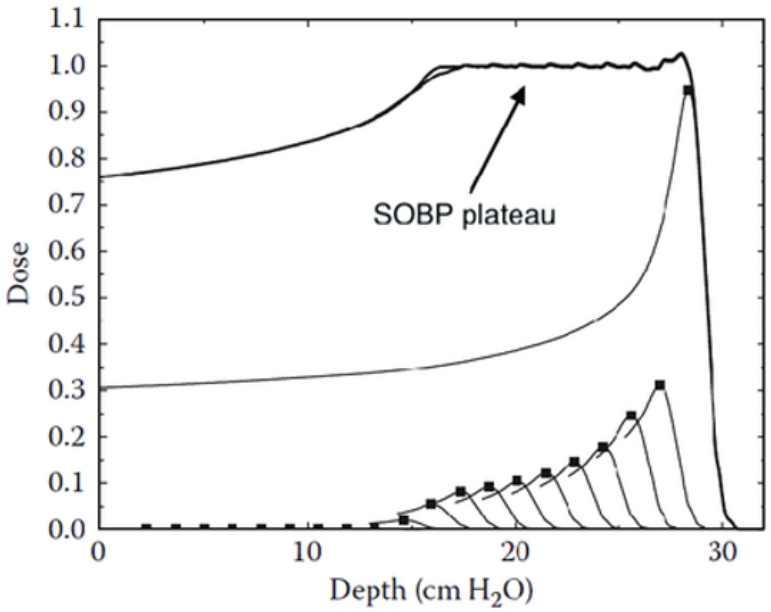

Figure 1.6: Projected proton spread out Bragg peak (SOBP) in water showing individual weighted Bragg curves that make up the SOBP. [12]

In contrast, active delivery techniques utilize a magnetically guided pencil beam that scans across the tumour volume under dynamic control of beam energy and intensity [13]. This method enables precise dose painting and reduces the need for physical beam modifiers, thereby minimizing the production of unwanted secondary particles. Active scanning allows for better conformation of the dose to complex tumour geometries and improved sparing of healthy tissues. However, it comes with increased complexity in both beam delivery and dosimetry. Accurate delivery requires careful management of potential errors that could result in underdosed or overdosed regions, in particular in cases where organ motion may alter tumour position during treatment.

1.2.2. Stopping Power

One of the primary advantages of hadron therapy over conventional treatments is its capacity to reduce radiation exposure to surrounding healthy tissues. This is due to the unique depth-dose profile of charged particles, which deposit the maximum of their energy near the end of their trajectory in tissue, rather than along the entire path. This energy deposition behavior can be described by the stopping power S, which defines the mean energy loss per unit distance traveled through a medium, as illustrated in Equation 1.6.

$$-\frac{dE}{dx} = S_e + S_n + S_r \tag{1.6}$$

The total stopping power is composed of three contributions: electronic (or collision) stopping power S_e, nuclear stopping power S_n , and radiative stopping power S_r [14]. Nuclear stopping power accounts for elastic collisions between the incident ion and target nuclei, while radiative stopping power refers to energy loss through bremsstrahlung radiation. At the therapeutic energies typically used in hadron therapy the dominant contribution to energy loss comes from inelastic Coulomb interactions with atomic electrons [15], described by the electronic stopping power. In this context, the stopping power can be approximately expressed as proportional to the square of the projectile's charge over its velocity:

$$-\frac{dE}{dx} \propto \frac{z^2}{v^2} \tag{1.7}$$

The full and more accurate description of this energy loss is given by the Bethe-Bloch formula [16], which quantifies the mean energy loss per unit path length for charged particles traversing a medium.

At shallow depths within the target, the charged particle loses little energy through electromagnetic interactions, since the stopping power is low. As the particle penetrates

deeper and slows down, its stopping power increases sharply, leading to a peak in energy deposition known as the Bragg peak. This occurs when the energy of the particle approaches the ionization potential of the medium, beyond which it can no longer generate secondary electrons. Consequently, the absorbed dose drops off rapidly beyond this point. However, due to the stochastic nature of energy loss at microscopic scales, the precise energy transferred to the medium varies from one particle to another. This leads to slight differences in penetration depth among particles of the same initial energy, a phenomenon known as energy straggling. Energy straggling becomes more significant at higher incident energies, where the overall range of the particles within the medium increases.

Moreover, particularly for heavy ion beams, nuclear interactions between the incident particles and the target nuclei can lead to the production of nuclear fragments and recoil particles. These secondary products form what is known as the fragmentation tail, which extends beyond the Bragg peak. This poses a challenge in charged particle therapy, as these fragments can deposit dose in healthy tissues both beyond and laterally to the treatment area as well as altering the relative biological effectiveness. The presence of such radiation increases the risk of secondary malignancies following treatment. As a result, careful consideration must be given to this radiation environment, with special attention to minimizing exposure to healthy tissues and organs at risk (OARs) that surround the tumour volume.

1.2.3. Linear energy transfer

The second principal advantage of charged particle therapy, alongside its superior ballistic precision, lies in the spatial pattern of energy deposition by these particles in matter. This is characterized by the linear energy transfer (LET), expressed in $\frac{keV}{\mu m}$, and Equation 1.8 is what is referred to as "restricted" LET [14]. The latter, denoted LET_Δ, represents the average energy deposited per unit path length by a charged particle via electronic interactions, excluding electrons ejected with energy above a threshold Δ.

$$LET_\Delta = (\frac{dE}{dx})_\Delta \tag{1.8}$$

For instance, LET_{250eV} quantifies energy deposition excluding electrons generated with energy $\geq$ 250 eV. This measure provides a more localized representation of energy deposition compared to total stopping power. When no subscript is specified, LET is assumed to be the unrestricted LET (LET_∞), which is equivalent to the stopping power.

Protons and heavier ions are characterized by a higher LET compared to photons. This implies a shorter mean free path between ionization events, resulting in a denser ionization

track structure, as illustrated in Figure Figure 1.7. The increased ionization density leads to the formation of damage clusters within biological tissues, such as DNA double strand breaks (DSBs) and free radicals generated from water radiolysis. These types of damage are more difficult for cellular repair mechanisms to manage, hence enhancing the biological effectiveness of the radiation.

Importantly, the high LET of charged particles can be leveraged to improve treatment efficacy in hypoxic tumors with reduced oxygen levels. Hypoxia arises when tumor growth outpaces the development of new blood vessels, leading to heterogeneous oxygen distribution within the tumor. Since oxygen enhances DNA damage induced by radiation through the fixation of free radicals, hypoxic cells tend to be more resistant to conventional low LET radiation like X-rays. The dense ionization of high LET ions, however, are less dependent on oxygen presence, making them particularly effective in targeting and destroying hypoxic tumor cells.

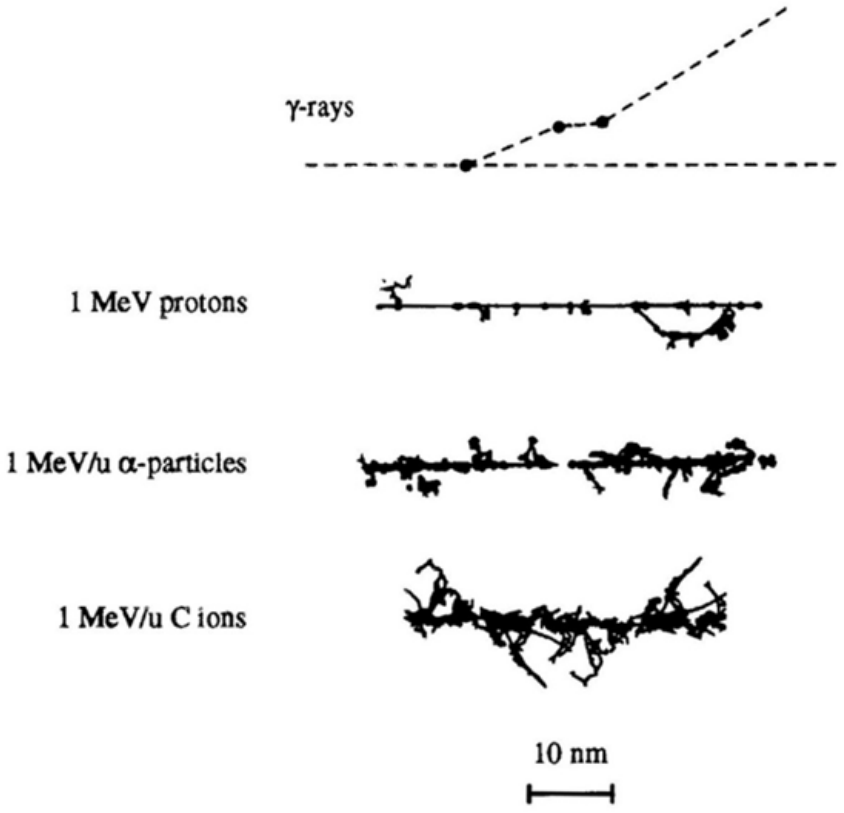

Figure 1.7: Schematic view of different particle tracks against different biological targets.

Hypoxia represents a negative prognostic and predictive factor, as it contributes to the development of radiation resistance, hence reducing the probability to control the tumor

[17]. The biological response of irradiated tissue is influenced by its oxygenation status, because oxygen enhances the fixation of free radicals that damage cellular components such as DNA. Consequently, tissues with higher oxygen content show greater radiosensitivity.

This effect is quantified by the Oxygen Enhancement Ratio (OER), which is defined as the ratio of the radiation doses required to achieve the same biological effect under hypoxic and fully oxygenated conditions:

$$OER = \frac{D}{D_0} \tag{1.9}$$

where D is the absorbed dose required to induce a given biological effect in the tissue and D_0 is the dose needed to produce the same effect in fully oxygenated tissue at standard atmospheric pressure. In vitro studies [18] have shown that for many cell types irradiated with X-rays under anoxic conditions, the oxygen enhancement ratio (OER) is approximately 3, as illustrated in Figure 1.8, which presents OER values corresponding to a 10% survival fraction in human cells. This indicates that a dose three times higher is necessary to achieve the same biological effect in tumor anoxic cells compared to well oxygenated tissues. The dense ionizing tracks of high LET radiation can induce significant biological damage even in hypoxic regions. These particles are less dependent on molecular oxygen for their direct damage. As a result, charged particle therapy is more effective in overcoming the radioresistance associated with hypoxia, effectively improving tumor control in otherwise resistant regions.

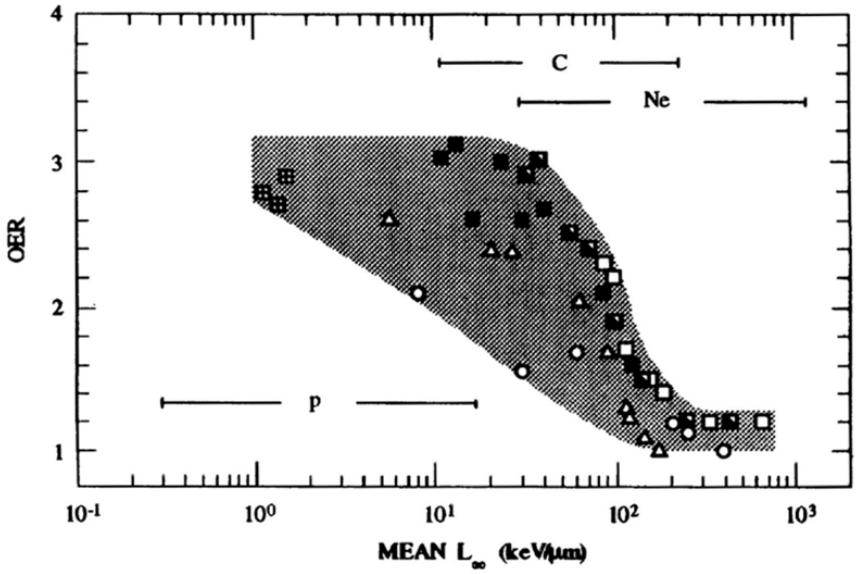

Figure 1.8: OER against LET for 10% surviving fraction of human cell cultures.

1.3. NCEPT

Neutron Capture Enhanced Particle Therapy is a targeted radiotherapy approach designed to improve outcomes for cancers with poor prognosis, proposed as an alternative approach to boron proton therapy by Safavi-Naeini et al [1] in 2018. It enhances conventional charged particle therapy by combining the physical precision of charged particle beams (such as protons, helium, or carbon ions) with the biochemical selectivity of neutron capture agents that preferentially accumulate in tumor cells. This dual-action method provides two key advantages over traditional particle therapy:

1. Localized dose amplification: the therapeutic dose within the target volume is increased due to the additional contribution from neutron capture reactions, without a proportional rise in dose to surrounding healthy tissues.

2. Treatment of micrometastases: since the thermal neutron field produced by particle interactions extends beyond the primary beam path, tumor specific neutron capture agents can deliver a dose even to microscopic or satellite tumor lesions outside the primary irradiation area.

NCEPT utilizes thermal neutrons that are generated in the treatment room during the interaction of high energy particle beams with the tissue and beamline materials. These neutrons are then captured by biologically targeted agents containing stable isotopes such as ^{10}B or ^{157}G, which are selectively absorbed by cancer cells [19]. The most studied reaction in this context is:

$$\begin{aligned} {}^{10}\mathrm{B} + n \;&\rightarrow\; {}^{11}\mathrm{B}^{*} \;\rightarrow\; {}^{7}\mathrm{Li} + {}^{4}\,\mathrm{He} + \gamma, \qquad && Q = 2.314\,\mathrm{MeV}\ (94\%) \\ {}^{10}\mathrm{B} + n \;&\rightarrow\; {}^{11}\mathrm{B}^{*} \;\rightarrow\; {}^{7}\mathrm{Li} + {}^{4}\,\mathrm{He}, && Q = 2.796\,\mathrm{MeV}\ (6\%) \end{aligned} \tag{1.10}$$

This reaction results in the emission of high linear energy transfer alpha particles and lithium nuclei, both damaging to biological tissues over short ranges, as well as gamma photons, most notably with an energy peak at 470 keV. These high LET products are responsible for the enhanced dose localized within tumor regions enriched with ^{10}B [20].

Although initial experimental observations of dose enhancement during proton therapy were attributed to the $^{11}B(p, 3\alpha)$ reaction (as reported by Cirrone et al [21] and Blaha et al [22]), further investigation revealed that neutron capture by ^{10}B, which has a natural isotopic abundance of 19.8% [23], is the dominant contributor to the observed effects [24]. This reinterpretation suggests that similar enhancements should also occur with helium or carbon ion beams in the presence of enriched ^{10}B. The neutron capture cross section

on ^{10}B is roughly three orders of magnitude larger than that of the $^{11}B(p, 3\alpha)$ reaction.

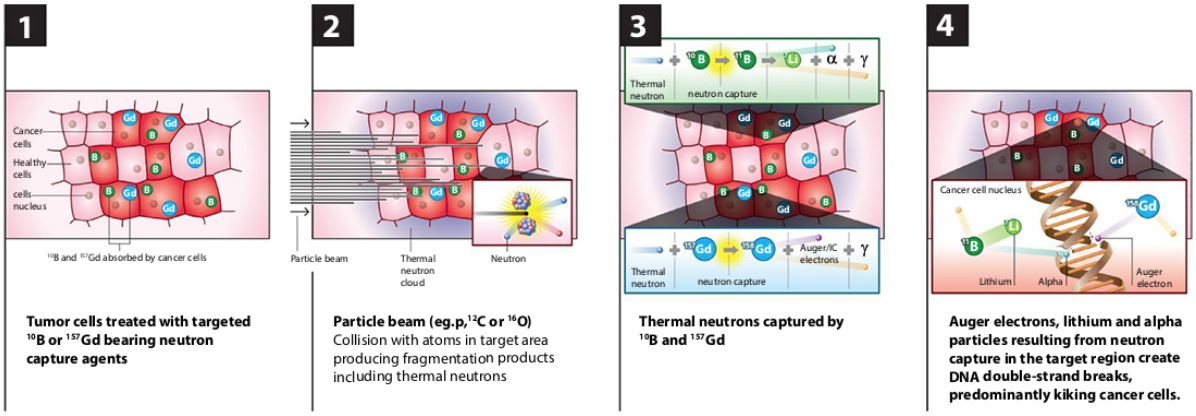

Figure 1.9: As the ion beam passes through tissues located before the tumor, some ions interact with the surrounding materials, producing various nuclear fragments, including neutrons that spread throughout the body and gradually lose energy until they become thermal. Tumor targeting agents deliver ^{10}B specifically to cancer cells, where these thermal neutrons are captured, leading to the emission of high LET particles with short ranges (4-8 μm). These neutrons can be captured wherever the capture agents accumulate, potentially delivering a therapeutic dose even to regions that would not be directly irradiated by the primary beam. [2]

The total dose delivered to the tumor in NCEPT comprises both the ion beam dose and the neutron capture dose. The latter is localized due to the short path length of the emitted high LET particles and the tumor specificity of the capture agent. This dual mechanism of action increases tumor control probability while reducing normal tissue toxicity, making NCEPT a promising approach to improve the therapeutic index of particle therapy.

2 | Microdosimetry and Radiobiology

Hadron therapy offers superior dose conformity and improved sparing of healthy tissues compared to conventional radiotherapy, but it also presents several challenges. One of the main complexities arises from the complex radiation field generated by inelastic hadronic interactions occurring during treatment [15]. Microdosimetry, which quantifies the energy deposited by radiation in microscopic volumes on the order of micrometers, comparable to the size of biological cells [25], is crucial for understanding these interactions. This is especially important because the relative biological effectiveness (RBE) of the radiation varies along the Bragg curve, influenced by the nature of the interactions and the energy of the particles involved. Given that energy deposition by ionizing radiation occurs through stochastic processes, analyzing these energy depositions at the micrometer scale enables a more detailed understanding of their biological effects. At these small dimensions, the randomness in both the number of ionizations or excitations and the energy transferred in each event becomes an important factor [26], making microdosimetry essential for assessing radiation effects on cellular structures.

2.1. Microdosimetric quantities

The energy deposited in matter by ionizing radiation is typically expressed in terms of absorbed dose and linear energy transfer (LET). They are defined respectively as:

$$D = \frac{d\bar{\epsilon}}{dm} \tag{2.1}$$

$$L = \frac{dE}{dx} \tag{2.2}$$

where $d\bar{\epsilon}$ is the mean energy imparted to a mass dm and dE represents the mean energy lost while traversing a distance dx. However, these are macroscopic, non-stochastic quantities and do not directly correlate with the biological effects of radiation, which arise

from the discrete and discontinuous nature of energy deposition in cell-sized volumes. To better investigate the biological impact, it becomes necessary to introduce analogous microdosimetric quantities that can describe energy deposition at microscopic sites where the behavior becomes stochastic.

The central quantity in microdosimetry is the mean lineal energy, denoted by y, which quantifies the stochastic nature of energy depositions along a defined chord length within tissue. It is defined as shown in Equation 2.3, where ϵ represents the energy imparted to a microscopic sensitive volume (SV), and $\langle l \rangle$ is the average chord length.

$$y = \frac{\epsilon}{\langle l \rangle} \tag{2.3}$$

The average chord length of any concave shape with a volume V and surface area S can be approximated using Cauchy's formula as shown in Equation 2.4. In the case of a spherical SV, typical in TEPC measurements, the average chord length is $\frac{2d}{3}$ where d is the diameter of the sphere.

$$\langle l \rangle = \frac{4V}{S} \tag{2.4}$$

Another key quantity is the specific energy, denoted by z, as defined in Equation 2.5, where m is the mass of the sensitive volume. The mean specific energy, $\langle z \rangle$ is equivalent to the non stochastic quantity of dose.

$$z = \frac{\epsilon}{m} \tag{2.5}$$

Lineal energy and specific energy are stochastic quantities, each described by a distribution function, $F(y)$ and $F(z)$, and an associated probability density, $f(y)$ and $f(z)$. These distributions are intrinsic to the radiation quality and do not depend on the absorbed dose or dose rate. In practice, the lineal energy distribution is commonly obtained using a multi-channel analyzer (MCA), which records energy depositions within defined time intervals. To derive the lineal energy spectrum $f(y)$, the recorded energy depositions are divided by the mean chord length $\langle l \rangle$ and the resulting distribution is normalized to unity. From this spectrum, key microdosimetric quantities can be derived, such as the frequency mean lineal energy $\bar{y}_f$ and the dose mean lineal energy $\bar{y}_d$.

$$\bar{y}_f = \int_0^\infty y f(y) dy \tag{2.6}$$

$$\bar{y}_d = \int_0^\infty y d(y) dy \tag{2.7}$$

where $d(y)$ is the dose probability density and it expresses the fraction of absorbed dose per event of lineal energy between y and $y + dy$. By definition this distribution is normalized to unity and typically plotted as $yd(y)$ vs $log(y)$. These two quantities are of interest in determining the quality of the radiation field. The relations between $d(y)$ and $f(y)$ are:

$$d(y) = \frac{y}{\bar{y}_f} f(y) \tag{2.8}$$

$$\bar{y}_d = \frac{1}{\bar{y}_f} \int_0^\infty y^2 f(y) dy \tag{2.9}$$

The major advantage of microdosimetry is that it allows to sort out quantitative information on the quality of mixed radiation fields without prior knowledge on the field composition.

The dose equivalent (H) is defined as a measure of radiation to identify and quantify the effects of ionizing radiation on health at a point in space. The unit of dose equivalent is the Sievert (Sv) with Q specified by the ICRU [26]. The dose equivalent is calculated using the following formula:

$$H = Q_{avg} D_{tissue} \tag{2.10}$$

where D_{tissue} is the dose absorbed in the tissue and Q_{avg} is the average value of the quality factor which can be evaluated through the convolution of $Q(y)$ and $d(y)$:

$$Q_{avg} = \int Q(y) d(y) dy \tag{2.11}$$

The ability of microdosimetry to determine average quality factor and dose equivalent makes it a very useful tool in a wide range of radiation fields.

2.2. Radiobiology

When treating a tumor with radiation, the goal is to eliminate cancer cells while minimizing damage to surrounding healthy tissue. Since it is not feasible to kill every single malignant cell without posing serious risks to normal tissues, treatment plans aim to reduce the tumor cell population below a threshold sufficient to prevent further growth. Understanding the radiation response of specific cell types is essential to determine the appropriate dose required to kill the target tumor.

Radiobiology is the scientific discipline that investigates how ionizing radiation affects biological systems, ranging from DNA and individual cells to entire tissues and organisms, including animal models and humans [27]. A fundamental method in radiobiology is the study of cell survival as a function of radiation dose, often assessed through clonogenic assays. These experiments measure the surviving fraction of cells based on their ability to form colonies after radiation exposure. For cancer cells, the loss of the ability to reproduce, known as reproductive death, is considered the key outcome and it serves as the primary endpoint in clonogenic survival analysis.

This concept is relevant in the context of radiation therapy. Effective treatment does not require the immediate physical destruction of all tumor cells during irradiation, but rather, the critical objective is to eliminate their capacity to proliferate. A cell may retain metabolic activity temporarily after irradiation, but if it has lost its ability to divide and form new cells, it is considered dead. The specific pathway through which the cell dies is less relevant from a therapeutic standpoint. What matters is the irreversible loss of reproductive potential. In larger biological systems like tumors, this loss of clonogenic capacity leads to a stop in tumor growth. Over time the tumor mass can reduce and be reabsorbed by the surrounding tissue.

Determining how a particular cell type responds to radiation is typically done using a cell survival curve. These curves are generated by irradiating cells in vitro, then allowing time for colony formation and finally counting the number of surviving colonies. The surviving fraction (SF) of cells is calculated using the relationship shown in Equation 2.12, which compares the number of colonies formed to the number of cells initially seeded, corrected by the plating efficiency (PE). The plating efficiency, defined in Equation 2.13, represents the ability of cells to form colonies and accounts for factors unrelated to radiation that may affect survival. Cell survival data are usually plotted on a semi-logarithmic scale, with the surviving fraction on the logarithmic axis and absorbed dose on the linear axis, as shown in Figure 2.1. This visual representation allows to compare cellular radiosensitivity across different treatments.

$$SF = \frac{Colonies}{Cells \times \frac{PE}{100}} \tag{2.12}$$

$$PE = \frac{Colonies}{Cells} \times 100 \tag{2.13}$$

The cell survival curve provides valuable information into how cells respond to different types of radiation. For high LET radiation, such as that delivered by heavy ions, the curve typically exhibits a straight linear decline, indicating that the damage, often double strand DNA breaks, is difficult or impossible for the cell to repair. In contrast, cell survival curves for low LET radiation, like X-rays or gamma rays, usually display a pronounced shoulder. This shoulder reflects the capacity of the cell to repair sub-lethal damage at lower doses. As the dose increases, however, the accumulation of damage surpasses the repair capacity, and the curve drops more steeply as sub-lethal lesions combine to form lethal ones. By comparing survival curves of different cell lines exposed to a common reference radiation, the radiosensitivity of each cell type can be assessed.

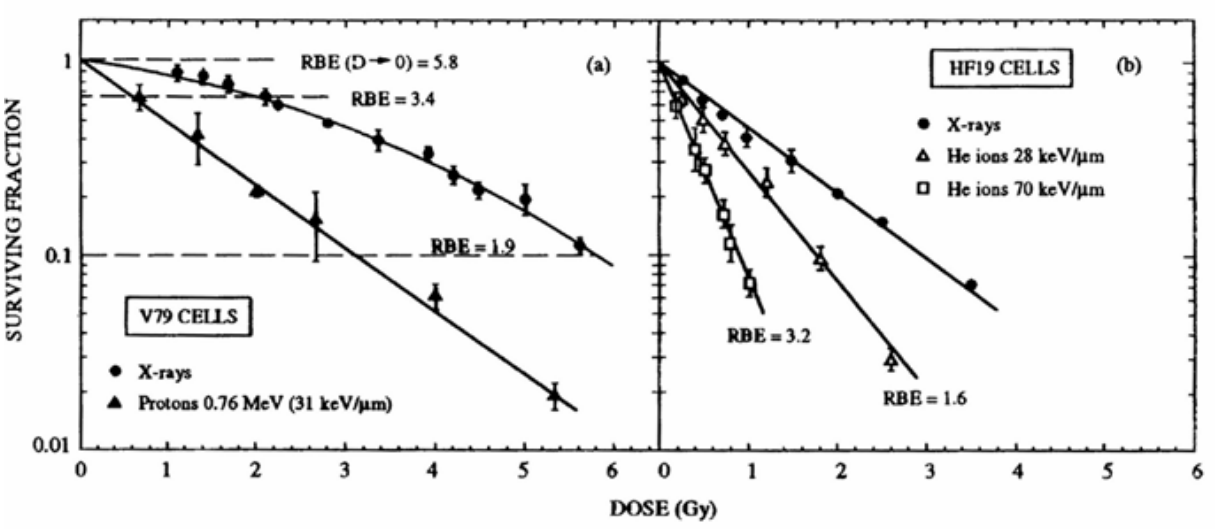

Figure 2.1: Survival curves of cells irradiated with X rays and low energy ions.

As shown in Figure 2.1, cells exposed to the ion beam require a noticeably lower dose to reach the same level of cell death compared to those irradiated with X-rays. This enhanced cell killing capability is described by the relative biological effectiveness (RBE). RBE measures the effectiveness of a given radiation type in producing a specific biological effect, relative to a standard reference radiation, typically photons from ^{60}Co. It is defined as the ratio of the absorbed dose of the reference radiation to that of the test radiation needed to achieve the same biological outcome, as described in Equation 2.14. One

commonly used endpoint for comparing RBE is the dose required to reduce the surviving fraction of irradiated cells to 10

$$RBE = \frac{D_{ref}}{D} \tag{2.14}$$

where D is the absorbed dose required to produce a given effect on the irradiated system and D_{ref} is the absorbed dose from the reference radiation field producing the same biological effect. The RBE is dependent on the radiation quality or LET, delivered radiation dose, dose rate, number of fractions, the chosen endpoint and oxygen concentration.

Because a lower dose is required to achieve the same biological effect, heavy ion therapy treatment plans do not rely on the physical dose, D, but instead on the biological dose, calculated as $D \times RBE$. This approach ensures that the prescribed dose reflects more accurately the biological impact of the radiation. While proton therapy typically applies a constant clinical RBE value of 1.1 [28], heavy ion therapy, using ions heavier than protons, requires a variable RBE since the biological effectiveness changes with depth and ion type. Heavier ions deliver significantly greater biological damage, particularly to radioresistant tumors, due to their higher LET. The relationship between RBE and LET for achieving 10% cell survival across various cellular systems is illustrated in Figure 2.2.

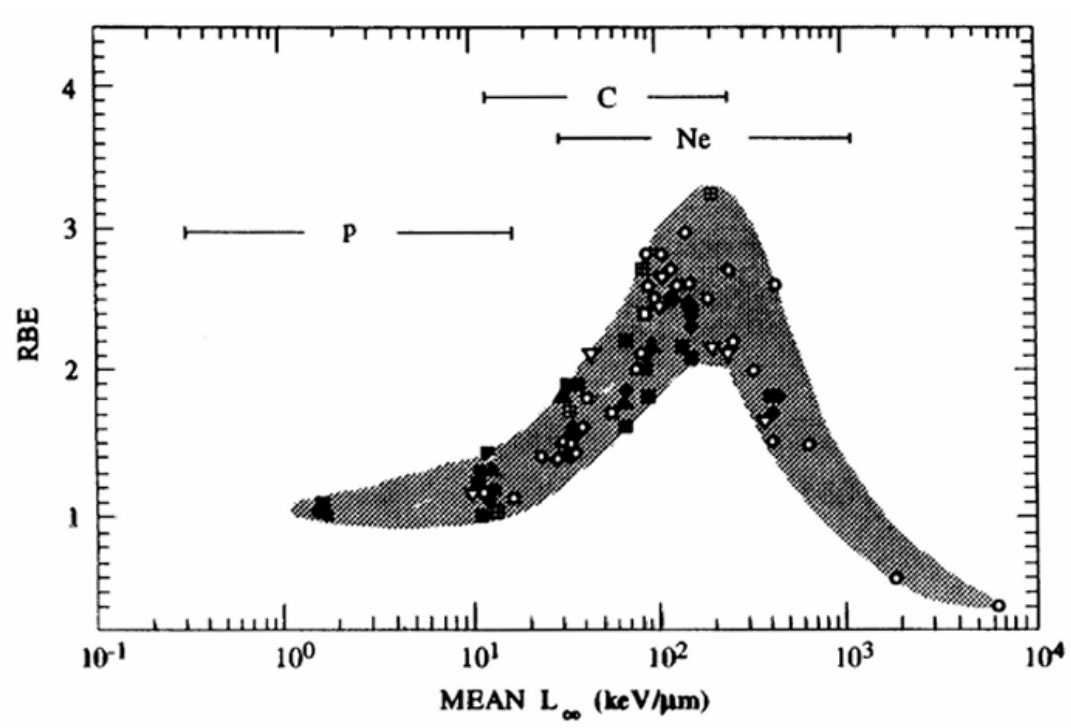

Figure 2.2: RBE against LET for 10% surviving fraction. Symbols refer to nine different cellular systems.

At higher LET values, such as those associated with carbon ions, the relative biological effectiveness can rise to approximately 3. This implies that, for a given biological effect, a carbon ion beam requires only one third the dose needed from the reference radiation. However, as LET continues to increase, such as with even heavier ions like neon, the RBE may actually begin to decline due to a phenomenon known as overkilling. Overkilling occurs when the radiation deposits more energy than necessary to kill a cell. Once critical targets like DNA are already irreparably damaged, additional energy does not lead to a greater biological effect but still contributes to the dose. As a result, the ratio defining RBE decreases. This effect typically begins to manifest at LET values around 100-150 $keV/\mu m$ [29]. The variation in biological damage caused by different radiation types is primarily due to differences in their track structure, resulting in differing ionization densities and thus varying biological impacts.

Since experimentally determining RBE and its dependencies is practically unfeasible, biological models are essential in radiotherapy treatment planning. These models help account for the complex interactions between radiation quality, dose, and biological response. By modeling the time-dose relationships of cellular responses to ionizing radiation, it becomes possible to predict cell survival for different radiation types and doses. This enables the estimation of RBE based on microdosimetric characteristics of the therapeutic beam. For an effective treatment plan, it is crucial to deliver a sufficient dose to the tumor volume to ensure adequate cell kill, while simultaneously minimizing the dose to surrounding healthy tissues to reduce the risk of long term effects such as secondary cancers. Various radiobiological models have been developed to describe the dose response behavior of cells and in the context of hadron therapy the use of more sophisticated models becomes necessary. This is due to the variation of RBE at different depths, which significantly complicates treatment planning compared to conventional photon therapy.

2.2.1. Linear quadratic model

This model begins by evaluating the cellular damage induced by radiation at the DNA level. According to the Theory of Dual Radiation Action (TDRA) [30], lethal damage is produced either from single critical chromosome breaks or from the pairwise interaction of DNA double strand breaks. The likelihood of these pairwise interactions, thus the probability of inducing lethal lesions, is considered to be proportional to the square of the specific energy z, whether the energy is deposited in a single event or across two independent events. To quantify the probability of cell survival following radiation, the Linear Quadratic Model (LQM) is widely adopted. This model relates the cell survival fraction, S, to the delivered dose, D. Here, $S = 1$ implies that all cells survive the given

dose, while values less than 1 indicate a reduction in surviving cells. The LQ model expresses this relationship as:

$$S = \exp(-\alpha D - \beta D^2) \tag{2.15}$$

where α and β are tissue specific radiosensitivity coefficients, measured in units of Gy^{-1} and Gy^{-2}, respectively. The linear quadratic model assumes that radiation induced cell death results from two distinct mechanisms, corresponding to two regions of the cell survival curve.

The first component, α, is linearly proportional to the dose and represents the initial slope of the survival curve. It accounts for damage caused by single radiation events, typically double strand breaks, which may directly result in cell death. In low LET radiation, this component is responsible for the shoulder observed in the initial region of the survival curve, reflecting the capacity of the cell to repair sub-lethal damage.

The second component, β, is proportional to the square of the dose and becomes increasingly significant at higher doses, where repair mechanisms are overwhelmed and damage from two separate ionization events combine to form lethal lesions. This results in the downward bending of the survival curve at higher doses. The β term reflects the probability of lethal damage arising from double hit event; hence DSBs generated by the interaction of two independent tracks.

For high LET radiation, the damage is typically irreparable, and the survival curve is nearly purely exponential, dominated by the linear term α. In such cases, the quadratic component β is negligible, indicating that even low doses can result in significant cell kill. The ratio α/β defines the dose at which the contributions from linear and quadratic components are equal, serving as a useful indicator of the radiosensitivity of a tissue and its response to fractionation. Tissues with a low α/β ratio are more sensitive to changes in dose per fraction, whereas tissues with a high α/β ratio are less sensitive to fractionation.

It should be noted that the linear quadratic model does not perfectly replicate the behavior of the cell survival curve at all dose levels. While it provides a good approximation at low to moderate doses, experimental data at very high doses often show that the survival curve tends to straighten out, becoming more linear rather than continuing to bend downward. This deviation occurs because the LQM predicts a quadratic term dominance at high doses, leading to a sustained curvature that does not always align with experimental observations. However, it is also worth noting that cell survival experiments rarely extend into these very high dose ranges, particularly in clinical or preclinical settings. As a result,

the LQM remains a practical and used tool for modeling clonogenic cell survival. One of its key strengths is its simplicity since it relies on just two parameters, α and β, which have clear biological interpretations and can be fitted directly from experimental data. Despite its limitations at high doses, the model offers a reasonable framework for understanding and comparing radiation effects in radiobiology and treatment planning.

2.2.2. Local effect model

The Local Effect Model (LEM), developed by M. Scholz and Kraft in 1996 [31], was formulated at GSI for calculating RBE values within treatment planning systems. The core principle of LEM is that cell inactivation results from lethal events whose occurrence is determined not by the radiation type itself, but by the microscopic track structure that the radiation produces within cellular targets. For X-ray exposure, the dose is distributed uniformly across the cell population. In contrast, ion beams deposit energy locally, leading to what is termed a local dose distribution. LEM models this by postulating that, after irradiating a group of cells with a given dose D, there is an average number N of lethal events responsible for cell death. Assuming these lethal events follow a Poisson distribution, the model expresses the surviving fraction of cells after irradiation with dose D, denoted as S(D), using the following relationship:

$$S(D) = \exp(-N(D))N(D) = -\ln S(D) \tag{2.16}$$

To further describe cell survival, the LQM is used, where the surviving fraction after a dose D is expressed in Equation 2.15. Substituting the LQM expression for S(D) into the LEM equation yields:

$$N(D) = \alpha D + \beta D^2 \tag{2.17}$$

If we consider the cell nucleus, with volume V, to consist of multiple sensitive sub-nuclear regions, then the density of lethal events within the nucleus, denoted as l(D), can be defined as:

$$l(D) = \frac{N(D)}{V} = \frac{-\ln(S(D))}{V} \tag{2.18}$$

It is postulated that the occurrence of a single lethal event within any sub-nuclear region is enough to result in cell death. For X-ray irradiation, the density of lethal events, l(D), is evenly distributed across the nucleus. In contrast, when only a fraction of the cell volume, ΔV, is exposed to radiation and the dose varies throughout the nucleus as D(x,y,z), determining the number of sub-nuclear regions that receive a lethal dose, N_{lethal},

involves integrating the spatial dose distribution over the entire nuclear volume :

$$N_{lethal} = \iiint \frac{\alpha D(x,y,z) + \beta D(x,y,z)^2}{V} \, dx \, dy \, dz \tag{2.19}$$

The fraction of cells that remain viable are those in which no lethal events have taken place. This can be expressed as:

$$S = \exp(-N) \tag{2.20}$$

The LEM estimates the RBE by utilizing the experimentally determined α and β parameters from X-ray irradiation studies. A fundamental assumption in LEM is that both the radiosensitivity of the cell and the size of the nucleus remain constant throughout the cell cycle. However, this introduces potential uncertainties, as both nuclear size and cellular radiosensitivity are known to increase during certain cell cycle phases. Additionally, LEM does not account for the effects of dose rate, which can further impact its accuracy. LEM enables the prediction of the biological impact of heavy ion irradiation by extrapolating from X-ray survival curves. This relies on the premise that, at a given absorbed dose, heavy charged particles and X-rays will generate the same number of lethal events within the cell. This assumption is valid at the nanometer scale, where the dose is deposited primarily via the track structure of the radiation. In such small volumes, whether the energy is delivered by X-ray secondary electrons or by the electrons from ion tracks, the biological effect is expected to be similar.

However, as the volume under consideration increases, the interaction mechanisms for X-rays and ions diverge, leading to differences in biological effectiveness. In larger volumes, the spatial distribution and density of energy deposition differ between radiation types, which can result in varying biological effects. LEM is a theoretical framework, grounded in simulations of ion track structures and their secondary particles across a range of energies. The parameters of the model are functions of the radial distance from the ion track, reflecting the localized nature of energy deposition. While LEM provides valuable results, its predictions of RBE must be validated through experiments. Overall, while LEM offers a theoretical tool for understanding the biological effects of different radiation types, its assumptions and limitations highlight the need for experimental validation and the integration of alternative models like MKM.

2.2.3. Microdosimetric kinetic model

The microdosimetric kinetic model (MKM), originally proposed by Hawkins in 1994 [32], builds upon the theory of dual radiation action by incorporating kinetic aspects of DNA damage repair. Its primary function is to derive the linear component of the linear quadratic model, the coefficient α, using tissue-specific parameters along with the dose mean lineal energy, $\bar{y}_d$, which is obtained through experimental microdosimetric measurements. The MKM considers the stochastic nature of energy deposition at microscopic scales, integrating both the physical interactions of radiation with matter and the biological processes of damage accumulation and repair. To extend its applicability to high LET radiation, Kase et al. [29] introduced modifications that take into account the phenomenon of overkilling. This enhanced version, commonly known as the modified MKM, allows for more accurate predictions of RBE across a broader range of LET values, especially relevant in therapies using heavier ions.

The MKM assumes that each cell nucleus contains multiple sub-nuclear spherical regions known as domains, whose dimensions are specific to the cell type. When a particle track passes through a cell, the stochastic nature of energy deposition leads to a distribution of deposited energies across these domains. Despite this randomness, the model presumes that the survival probability S of a domain after receiving a certain dose D follows the same functional form as in the LQM, which is typically used for low LET radiation. This assumption allows the MKM to link microdosimetric energy distributions directly to biological outcomes.

$$S = \exp[-AD - BD^2] \tag{2.21}$$

where A and B are cell specific like α and β in equation Equation 2.15 for LQM. The average number of lethal lesions, L, in the domain for the specific energy, z, is given by a linear quadratic relationship:

$$L = Az + Bz^2 \tag{2.22}$$

The number of hits occurring in each domain is assumed to follow a Poisson distribution. The average number of lethal lesions in a nucleus, L_n, and the surviving fraction, S, can be described as follows:

$$\begin{aligned} L_n &= N\bar{L} = N(A\bar{z} + B\bar{z}^2) \\ &= (\alpha_0 + \beta_0 z_{1D})D + \beta D^2 \\ &= -\ln S \end{aligned} \tag{2.23}$$

where N is the number of domains in a nucleus, D is the absorbed dose and z_{1D} is the

specific energy in a single event in domain. The value of z_{1D} can be calculated by:

$$z_{1D} = \frac{l}{m} y_d = \frac{y_d}{\rho \pi r_d^2} \tag{2.24}$$

where ρ, r_d, l and m are the density, radium, mean chord length and mass of the domain, respectively. To take into account overkilling effects, also called saturation effects, the saturation parameter, y_0, is introduced :

$$y_0 = \frac{\rho \pi r_d R_n^2}{\sqrt{\beta (r_d^2 + R_n^2)}} \tag{2.25}$$

where R_n is the radius of the nucleus instead of the domain. The saturation corrected dose mean lineal energy, y^* is similar to y_d but accounts for overkilling effects at high lineal energies, where Kase et al. [29] found values for y_0 equal to 150 $keV/\mu m$ provided the best fit to survival data:

$$y^* = y_0^2 \frac{\int (1 - \exp(-y^2/y_0^2)) f(y) dy}{\int y f(y) dy} \tag{2.26}$$

This correction is then applied to the modified MKM parameter α:

$$\alpha = \alpha_0 + \frac{\beta}{\rho \pi r_d^2} y^* \tag{2.27}$$

where α_0 is the initial slope of the survival fraction curve in the limit of zero LET and β is a constant independent of LET. The RBE_{10} can thus be obtained as:

$$RBE_{10} = \frac{2\beta D_{10,ref}}{\sqrt{\alpha^2 - 4\beta \ln(0.1)} - \alpha} \tag{2.28}$$

where $D_{10,ref}$ is the dose required for 10% survival for 200 keV X-rays and has a value of 5 Gy. In the case of low lineal energy regions, the value of α could be regarded as a simple linear function of z_{1D} as follows:

$$\alpha \approx \alpha_0 + \beta z_{1D} = \alpha_0 + \beta \frac{y_d}{\rho \pi r_d^2} \tag{2.29}$$

2.2.4. Biological weighting function

The biological weighting function (BWF) model offers a microdosimetric based framework for estimating the RBE of different radiation types. It was originally designed to facilitate

comparisons among radiotherapy beams used in clinical settings. Over time, it has been widely adopted for use with microdosimetric spectra, whether obtained experimentally or through Monte Carlo simulations. This approach operates on the principle that the biological effect of radiation can be quantified by integrating the dose weighted lineal energy spectrum, d(y), with a biological response function, r(y), known as the BWF (Equation 2.30). The shape and form of this weighting function are chosen based on the specific biological endpoint of interest, allowing the model to translate microdosimetric information into predictions of biological impact.

$$RBE = \int_0^\infty d(y)r(y)dy \tag{2.30}$$

One of the most commonly adopted BWFs was derived by Loncol et al.[33] in 1994 using an unfolding method applied to combined datasets from spherical tissue equivalent proportional counters (TEPCs) and biological experiments involving exposures to photons, neutrons, and protons. The biological effect chosen for calibration was the tolerance of the mouse intestine, evaluated through in vivo crypt regeneration assays following an 8 Gy dose. The resulting BWF, shown in Figure 2.3, is expressed as a function of lineal energy y, and was defined only up to a maximum y value of 1000 $keV/\mu m$.

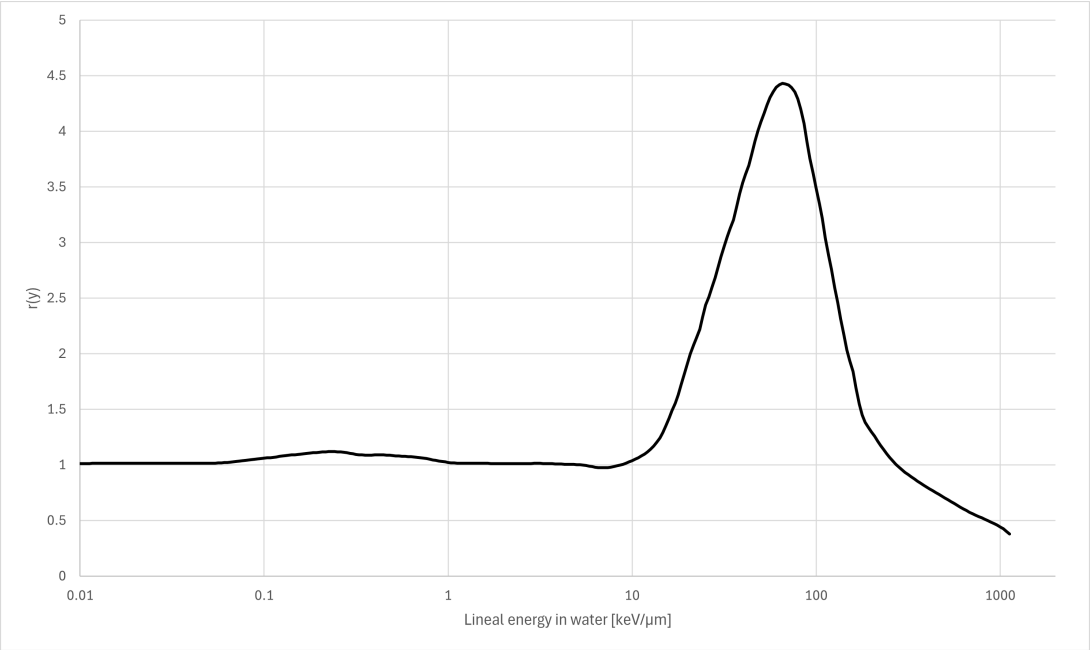

Figure 2.3: Loncol's biological weighting function. Figure adapted from [33]

It is important to note that the BWF was derived from measurements performed in

TEPCs filled with a tissue equivalent propane-based gas mixture. Ideally, for consistency, the lineal energy spectra used in RBE calculations should be evaluated in this medium. However, because the mass stopping power ratio between this gas mixture and liquid water remains approximately 1 across the relevant energy and particle types (according to SRIM 2013, Ziegler et al.[34]), the BWF proposed by Loncol et al.[33] can be directly applied to lineal energy spectra simulated in liquid water without introducing discrepancies.

A key distinction between the MKM and the approach proposed by Loncol lies in their treatment of the microscopic dose distribution. While the MKM primarily relies on average quantities such as the dose mean lineal energy $\bar{y}_d$ or the saturation-corrected lineal energy y^* , Loncol's method incorporates a weighting function that evaluates the full distribution d(y) of lineal energy. This enables the model to account for the entire spectrum of microscopic energy deposition events rather than just their mean values. As a result, even when two radiation fields exhibit identical $\bar{y}_d$ or y^*, differences in their underlying d(y) distributions can be captured, making Loncol's method more sensitive to variations in radiation quality than the MKM.

Parisi et al.[35] developed an improved biological weighting function (IBWF) to establish a robust correlation between microdosimetric lineal energy probability density distributions and the RBE for in vitro clonogenic cell survival at 10% surviving fraction in V79 Chinese hamster lung fibroblasts. This model enables fast and reliable RBE assessment across a wide range of ion species and energies. Further details on the IBWF and its application can be found in [35].

2.3. Introduction to Monte Carlo - GEANT4

The Monte Carlo method is a powerful numerical approach widely used in particle and nuclear physics for simulating stochastic interactions of particles with matter. It is suited for systems influenced by stochastic processes and has been adopted in fields such as radiation transport, nuclear physics, astrophysics, and medical physics. Monte Carlo simulations are based on the fundamental principle of simulating individual particle histories using known physical probabilities and cross sections. Each particle's trajectory and interactions are determined through a sequence of random sampling from probability distributions that describe physical processes such as scattering, absorption, and secondary particle generation. In radiation research, Monte Carlo simulations are important because they allow for accurate modeling of particle interactions within specified materials and geometries, based on defined input parameters such as particle energy and phantom composition. Monte Carlo simulations track individual particles through matter, accounting for every possible interaction. A typical Monte Carlo code involves the definition of the simulation geometry, primary particle source, their energies, and the physics processes to consider. The simulation proceeds by generating random numbers to determine the outcomes of particle interactions. For each primary particle, a complete history is simulated, including the generation and transport of any secondary particles. Secondary particles can either be ignored, hence it is assumed that they deposit all their energy locally, or tracked after the primary particle completes its transport. The user defines sensitive volumes within the geometry, where interaction data are recorded. These information allow for detailed analysis of the radiation field and its biological relevance.

Several Monte Carlo codes exist, from general purpose frameworks to application specific ones. The simulations discussed in this thesis were carried out using Geant4 (GEometry ANd Tracking), a widely adopted open-source C++ toolkit initially developed at CERN for high energy physics [36][37][38]. First released in 1998, Geant4 has since expanded to serve medical physics and radiation protection through the implementation of low energy physics extensions. A Geant4-DNA package allows one to describe particle interactions down to ∼eV scale. The object-oriented platform is designed for simulating the passage of particles through matter. Geant4 allows for the full customization of simulations through a modular architecture. Unlike some Monte Carlo systems that provide a pre defined user interface, Geant4 requires users to build a C++ application and the minimum requirements is the inclusion of three fundamental classes:

- DetectorConstruction : defines the geometry and materials of the setup;
- PrimaryGeneratorAction : specifies the source particles;

- PhysicsList : includes particles, physical processes, and production thresholds.

Geant4 is used in a wide energy range, from eV to TeV, and supports simulations of electromagnetic, hadronic and radioactive decay processes. The strength of Geant4 lies in its comprehensive suite of physics models. For electromagnetic interactions, the toolkit includes processes such as ionization, multiple scattering, Bremsstrahlung, pair production, Compton scattering, photoelectric and Rayleigh effects. They are modelled in an energy range between $\sim$ 100 eV to $\sim$TeV scale. In electromagnetic physics processes, a production threshold must be defined for secondary particle generation. This threshold is specified in terms of the range that secondary particles would travel within a given material. If a secondary particle's range exceeds the defined cut, it is generated and tracked in the simulation. Otherwise, its energy is assumed to be deposited locally at the point of origin. Hadronic interactions are handled through a range of models, verified against experimental databases [37] like NIST [39]. Hadronic interactions are modeled using a combination of physics models that cover a wide energy spectrum, ranging from thermal neutron energies up to the TeV scale.

One of Geant4's strengths lies in its geometry construction capabilities. Users can build complex setups using a library of primitive shapes and custom material definitions. Solids can additionally be created using CAD systems. Users can define homogeneous and heterogeneous materials either from pre-defined elements and compounds or by specifying custom elemental and isotopic compositions. It is also possible to model a material based on its temperature, pressure and state (solid, liquid or gaseous). This allows for the accurate modeling of biological tissues, detector materials, and experimental phantoms. For what concerns the primary source, the General Particle Source (GPS) is a feature within Geant4 that enables the simulation of complex radiation fields using straightforward, predefined user interface commands. Visualization tools integrated in Geant4 support verification of the simulation setup and facilitate debugging.

Historically, the main limitation of Monte Carlo methods has been long computational times. However, Geant4 includes various optimization features to address this. In this work, simulations were executed on high performance computing facilities including the University of Wollongong cluster and the National Computational Infrastructure (NCI) Gadi supercomputer. These resources significantly reduced computation times, enabling the execution of complex simulations needed for microdosimetric analysis. Moreover the production cut of secondary particles was defined to achieve fast simulation execution speed without sacrificing the accuracy of the results. With continuing advances in computing power, Monte Carlo methods are becoming increasingly viable for clinical applications, including direct integration into treatment planning systems for radiation therapy.

3 | Detectors and Setup

Detectors are essential tools in microdosimetry for measuring energy deposition at microscopic scales, helping to understand radiation effects on biological targets. Common detectors include tissue-equivalent proportional counters (TEPCs), silicon solid-state detectors, and diamond detectors, each offering distinct advantages in terms of sensitivity and resolution. This chapter reviews these typical microdosimetry detectors and then presents the simulation configurations used in this work. Using Geant4, virtual detector models were created to replicate real detector responses, enabling analysis of radiation interactions. This combination of experimental detector principles and simulation setups provides a comprehensive framework for studying microdosimetric measurements.

3.1. Tissue equivalent proportional counters

The tissue equivalent proportional counter (TEPC) is regarded as the gold standard in microdosimetric measurements due to its ability to replicate the energy deposition in biological cells. TEPCs are designed with a spherical sensitive volume filled with a low pressure tissue equivalent gas, typically maintained at a few tens of mmHg. This configuration enables the detector to emulate the microscopic volume of a human cell, making it suitable for studying radiation effects at the cellular scale. As illustrated in Figure 3.1, a metal wire, serving as the anode, runs across the diameter of the spherical cavity, while a bias voltage is applied between the wire and the surrounding conductive wall. This arrangement creates an electric field that collects the ionization charges produced within the gas by traversing radiation. One of the primary advantages of TEPCs is their capability to measure the lineal energy spectrum. Their spherical geometry ensures uniform response regardless of the angle of particle incidence and the tissue equivalent composition of both the gas and the chamber wall ensures that the measured interactions are representative of energy depositions in biological tissue.

Despite these strengths, TEPCs also present a number of limitations that affect their applications. They operate at high voltages. Furthermore, due to their relatively large dimensions they suffer from poor spatial resolution. A continuous supply of the gas

mixture is required to maintain consistent performance. Another critical limitation is that TEPCs model only a single, isolated cell [40]. Wall effects represent a source of uncertainty. These occur when primary or secondary particles interact with the wall material before reaching the gas filled sensitive volume, leading to scattering or partial energy loss. Such interactions can distort the energy deposition and introduce errors in the measurement of microdosimetric quantities [26]. For these reasons, while TEPCs remain a benchmark in microdosimetry, alternative detector technologies such as solid state microdosimeters have been developed to overcome some of these limitations.

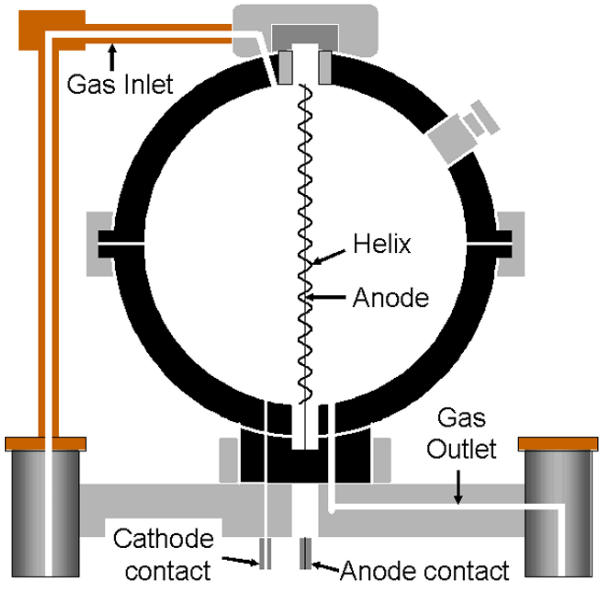

Figure 3.1: Rossi proportional counter [41]

The relatively large size of a TEPC hides its ability to measure energy depositions equivalent to those in micron sized tissue volumes. The energy deposited in the gas filled sensitive volume, E_g, is interpreted as being equivalent to the energy deposited in an equivalent tissue volume, E_t , at the cellular scale. This is made possible by operating the detector with a low pressure tissue equivalent gas, which has a specific mass stopping power $(S/\rho)_g$. The following relationship allows the measured quantities in the gas to be scaled to biologically dimensions using this expression:

$$\Delta E_g = \Delta E_t \tag{3.1}$$

$$\left(\frac{S}{\rho}\right)_g \rho_g d_g = \left(\frac{S}{\rho}\right)_t \rho_t d_t \tag{3.2}$$

Wall effects occur due to the density differences between the gas-filled cavity of a TEPC

and its surrounding wall. Rossi [42] and Kellerer [43] described four primary wall effects.

The delta-ray effect arises when a heavy ion passes through the wall, producing secondary electrons. In a TEPC, both the primary ion and its delta rays can enter the cavity together and deposit energy in the same event. In contrast, in actual tissue, the primary ion and its delta rays are more likely to deposit their energy in separate volumes due to the uniform density. This leads to an artificial increase in the $\bar{y}_f$ and the $\bar{y}_d$, since the energy contributed by delta rays is typically much less than that of the primary ion. The re-entry effect involves electrons that, after escaping the cavity, re-enter it following a curved trajectory. This is more likely in the low-density gas of a TEPC, where electrons can travel longer distances and bend back into the cavity. In real tissue, the higher density makes the distance much greater than the size of a biological target, so such re-entry is improbable. The re-entry effect is most significant for electrons with energies up to about 1 MeV. The V effect is associated with inelastic nuclear interactions occurring in the wall material. When such an interaction takes place near the cavity, it can produce several charged nuclear fragments, such as protons or α particles, which may all enter the same TEPC cavity and deposit their energy together. In actual tissue, these fragments would typically traverse and deposit energy in separate volumes because their tracks diverge and the sensitive sites are much smaller. The scattering effect occurs when neutral particles like neutrons or photons interact with the wall and generate multiple charged particles. These particles can simultaneously pass through the TEPC cavity and deposit energy as a single event. In real tissue, the sensitive volumes are small enough that the tracks of these secondary charged particles would usually cross separate volumes, not the same one.

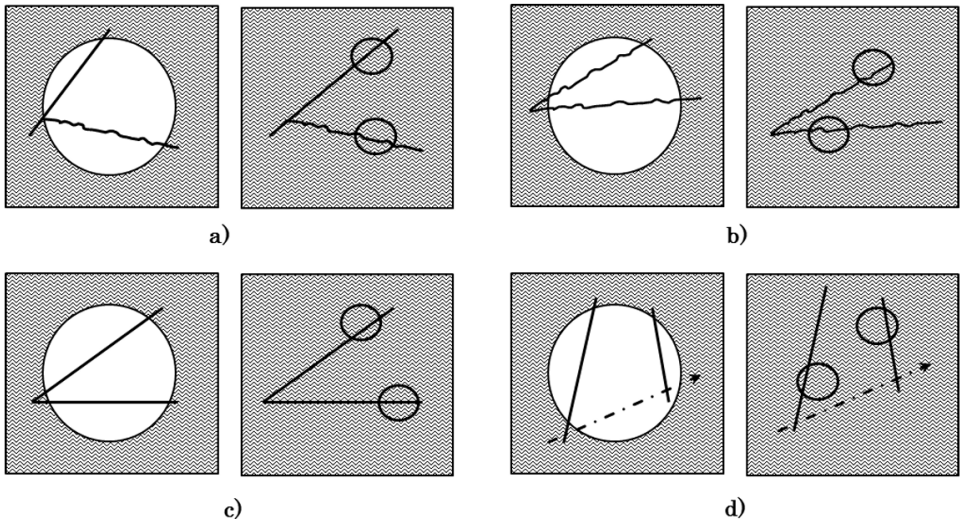

Figure 3.2: Illustrations of wall effects in a low pressure proportional counter: a) Delta-ray effect, b) Re-entry effect, c) V effect, d) Scattering effect

3.2. Silicon Microdosimetry

As an alternative to TEPCs, the Centre for Medical Radiation Physics (CMRP) at the University of Wollongong has developed a solid state microdosimeter that overcomes key limitations of traditional gas detectors [44]. Silicon was first employed in microdosimetry in 1980, when Dicello et al. conducted measurements using a silicon diode [45]. These silicon microdosimeters use arrays of micron sized sensitive volumes (SVs) fabricated on silicon on insulator (SOI) substrates, where an insulating SiO_2 layer beneath the active region blocks charge collection from deeper depths. Unlike TEPCs, they are compact, portable, operate at low voltages ($\sim$ 10 V) and do not require continuous gas flow. Their SVs, typically 2-10 μm thick, enable high spatial resolution and permit the replication of an array of biological cells, making them ideal for high dose rate environments without pile up issues.

A significant advantage of silicon microdosimeters lies in the ionization energy: silicon has a mean ionization energy of approximately 3.6 eV, which is about ten times lower than that of gas ($\sim$ 30 eV). This means that for the same amount of deposited energy, silicon generates roughly ten times more electron-hole pairs, leading to lower statistical fluctuations, superior energy resolution and a higher signal to noise ratio, especially for low LET radiation where electronic noise becomes limiting. For accurate microdosimetric measurements, certain design and operational requirements must be met: the SV must be well defined to calculate the mean chord length precisely; charge collection must avoid contributions from outside the depletion region to maintain measurement fidelity; last, a tissue equivalence correction factor is required to translate silicon based measurements to tissue relevant quantities. A dedicated data acquisition system supports these devices, incorporating a charge sensitive preamplifier, shaping amplifier, and multichannel analyzer for real time microdosimetric spectrum processing. Additionally, chip segmentation reduces capacitance and electronic noise while maintaining sufficient event statistics.

The main challenge with using silicon is that its measured signal does not directly reflect a biological tissue equivalent response. To address this, several studies have explored methods to convert silicon detector outputs into tissue equivalent values. A common approach involves determining the size of the tissue volume that corresponds to the silicon sensitive volume. Once this equivalent tissue volume is established, the lineal energy can be recalculated using the mean chord length of the tissue, as shown in Equation 3.3. Alternatively, this is often done by applying a scaling factor k to the chord length or,

more commonly, to the energy deposition ϵ, as expressed in Equation 3.4.

$$y = \frac{\epsilon}{\langle l_{Tissue} \rangle} \tag{3.3}$$

$$y = \frac{k\epsilon}{\langle l_{Silicon} \rangle} \tag{3.4}$$

Bradley and Rosenfeld [46], using ICRU muscle as the reference in a boron neutron capture therapy field, determined a scaling factor k equal to 0.63. Guatelli et al. [47], using water as the reference for therapeutic proton fields, reported a scale factor of 0.56. Bolst et al. [48] examined striated muscle and found scale factors of 0.58 for protons and 0.57 for ^{12}C, while with water as the reference, they found a factor of 0.54. In the present work, a scale factor of 0.58 was adopted using muscle as the reference tissue.

Another important challenge in using silicon microdosimeters, particularly in hadron therapy, is the application of Cauchy's equation to determine the mean chord length for calculating lineal energy. This equation assumes isotropic radiation fields and spherical sensitive volumes, whereas silicon devices are typically fabricated with cylindrical geometries and hadron therapy beams are highly directional and conformal. These discrepancies can lead to inaccuracies if the standard approach is used. To better reflect the actual geometry and irradiation conditions, in this work the height of the cylindrical sensitive volumes was adopted as the effective mean chord length.

3.3. Mushrooms SOI

The development of silicon microdosimeters at CMRP has progressed through four generations, each aiming to improve charge collection and sensitive volume definition. The first generation used a silicon-on-insulator (SOI) diode array, featuring 4800 parallel connected diodes (10×10 μm^2 each) in three thicknesses (2, 5, and 10 μm) [40]. However, these devices suffered from lateral charge diffusion and electric field distortion, leading to poorly defined sensitive volumes.

The second generation of devices tried to make the sensitive area more uniform and better defined. They were based on an array of physically isolated cylindrical 2D planar structure. The redesign introduced p^+ guard rings, which simplified manufacturing and increased SV yield to nearly 100%, although some lateral diffusion persisted.

Third generation devices kept the planar guard ring design but increased the SV diameter and expanded the active area by about 16 times. They used high resistivity n-type silicon

and added p^+ electrode cores, enabling the rejection of laterally diffused events through coincidence detection, further improving charge collection and SV yield.

However, planar technology has some drawbacks, such as non uniformity of the charge collection in the SV and diffuse charge collection outside the SV. For these reasons, the current, fourth generation focuses on fully etched "Bridge" and "Mushroom" structures. These designs offer superior charge collection uniformity, better SV definition, enhanced radiation hardness, and improved timing compared to earlier planar detectors. In this thesis, the focus will be on the Mushroom design.

3.3.1. Detector Design

The detector used in this study is the Mushroom silicon-on-insulator detector introduced by CMRP. The concept of SOI microdosimeters with 3D cylindrical SVs is to mimick the dimensions of cells in an array. SVs were segmented into sub-arrays to reduce the capacitance and avoid pile up in high dose rate applications.

It features an independent read-out system for even and odd rows of sensitive volumes, preventing events in adjacent SVs from being interpreted as a single event when charged particles travel along oblique paths. This dual-channel readout also enhances the RBE determination for different high energy ions with the same LET but distinct delta electron track structures. The detector's charge collection efficiency and response have been thoroughly investigated and documented in previous works [44][49].

The Mushroom microdosimeter, shown in Figure 3.3, features freestanding, 3D cylindrical SVs shaped like *mushrooms* and fabricated on a high resistivity *p*-SOI wafer. The structure used in this work represents the generation of devices designed by CMRP referred to as the "trenched planar" design. This configuration consists of 3D cylindrical SVs with an inner planar n^+ core, produced by ion implantation to ensure precise and uniform doping. Each SV is surrounded by a full p^+ doped trench, etched into the silicon active layer and subsequently filled with polysilicon. The outer wall of this trench is also p^+ doped, a feature designed to prevent charge collection from regions outside the SV, ensuring that only charge generated within the SV contributes to the detected signal; hence, background noise is minimized and accuracy is enhanced. Furthermore, the p-stop layer was connected to the outer p^+ trench to avoid charge build-up in the oxide layer between the SVs after being irradiated with heavy ions.

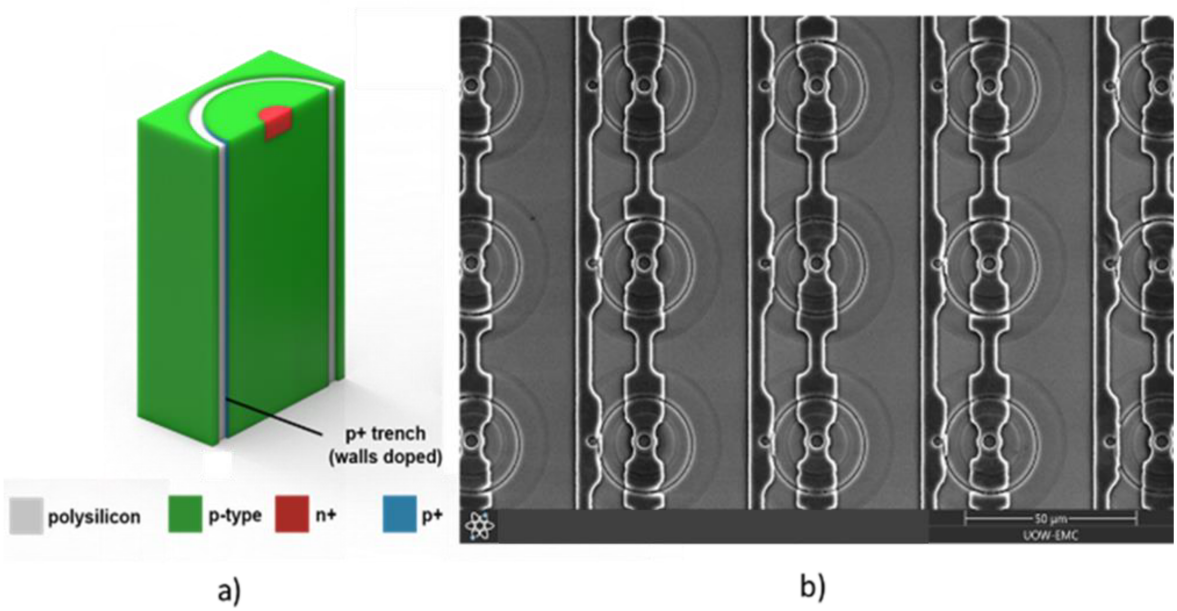

Figure 3.3: (a) Illustration of the trenched 3D Mushroom microdosimeter, featuring a p^+ doped trench filled with polysilicon and a planar n^+ core; (b) SEM image showing an array of planar core sensitive volumes in the trenched 3D Mushroom microdosimeter [50]

In order to connect SVs in an array, the trench was filled with polysilicon to support the aluminum contact in the inner n^+ electrode. Outer aluminum tracks, each 1.2 µm thick, are connected to the p^+ outer electrodes of the 3D SVs, establishing an electrical connection between the SVs, forming an interconnected array to facilitate efficient charge readout. The active layer of the microdosimeter is fabricated on high resistivity p-type silicon, which is bonded to a low resistivity supporting wafer. A 0.75 µm silicon oxide layer is positioned between these layers.

The cylindrical geometry of the sensitive volumes closely resembles the size and shape of human cells. This design reduces the angular dependence on radiation incidence, leading to improved alignment between experimental microdosimetric measurements and radiobiological models. By replicating the geometrical characteristics of human cells, the device provides a more realistic simulation of cellular energy deposition.

Several models of the Mushroom microdosimeter have been developed, differing in the number of SVs and featuring thicknesses of 2, 5, or 10 µm, with diameters of 18, 20, or 30 µm. These dimensions are important factors to consider when selecting a suitable SOI microdosimeter for experimental measurements.

The number of SVs is primarily determined by the radiation dose rate. A higher number of SVs increases the overall sensitive area, which enhances statistical accuracy and reduces

acquisition times, particularly important under low dose rate conditions. The larger detection area allows more events to be recorded in a shorter period, improving data reliability and reducing measurement time.

However, increasing the number of SVs also results in trade-offs. A greater number of SVs leads to higher leakage current and increased device capacitance, both of which contribute to high electronic noise. This additional noise can degrade signal quality, reducing the microdosimeter's ability to resolve low energy events. Therefore, the selection of the number of SVs involves balancing the need for faster data acquisition and improved statistics against the potential for increased noise and reduced sensitivity to small energy depositions.

Thinner sensitive volumes reduce the likelihood of particles stopping within the volume, ensuring that the energy deposited is associated with a track characterized by the correct mean chord length. This leads to microdosimetric spectra that more accurately reflect the physical reality of energy deposition. In addition, thinner SVs provide improved spatial resolution, particularly at the distal edge of the Bragg Peak, where the dose gradient is steep. In this region, even a small shift of a few micrometers can significantly affect the dose-mean lineal energy, y_D. A thinner SV averages the deposited energy over a smaller distance, capturing more precisely rapid changes in the dose profile and enhancing resolution in regions with high variations. In contrast, thicker SVs offer different advantages, including the ability to register a higher number of events, leading to an improved signal-to-noise ratio. Increased SV thickness also allows for the detection of a broader range of energy depositions, expanding the dynamic range of the microdosimeter. This wider range helps prevent compression of the energy spectrum, a phenomenon that can occur in thinner detectors, affecting the resolution at lower energies. However, in radiation fields with high energy deposition, thicker SVs may result in saturation of the MCA, leading to data loss. This requires careful selection of the microdosimeter thickness to balance the spatial resolution, dynamic range and signal quality, according to the specific requirements of the radiation field and experimental setup.

In the present work, the Monte Carlo simulations have been carried out with a Mushroom device with 1600 SVs (40x40 matrix) of thickness 10 µm and diameter 20 µm, 50 µm pitch. The design of the SV array is shown in Figure 3.4.

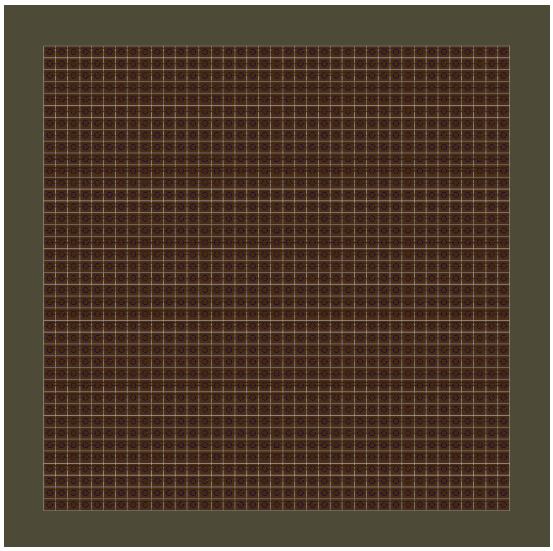

Figure 3.4: Array of the SOI device with 40 x 40 sensitive volumes.

3.3.2. Detector design for NCEPT

In this work, the contribution from thermal neutrons during proton irradiation is addressed by modifying the microdosimeter design to enable detection of the $^{10}B(n,\alpha)^{7}Li$ reaction. Three configurations were considered in the simulations. The first configuration consisted of a standard Mushroom SOI microdosimeter, which served as a reference for evaluating the effects of neutron interactions. In the second configuration, the sensitive volume of the detector was uniformly doped with 1% ^{10}B, allowing neutron capture reactions to occur directly within the SV. In this scenario, the majority of the energy from the reaction products is deposited inside the SV, as the generated α and ^{7}Li particles do not traverse any intervening material before detection. This approach minimizes energy loss and maximizes the detection efficiency for neutron induced events.

To further enhance sensitivity to thermal neutrons, a boron carbide (B_4C) converter layer highly enriched in ^{10}B was implemented in the third configuration. B_4C thin films are widely used in neutron detection due to the high neutron absorption cross section of ^{10}B, as well as the favorable physical and chemical properties of boron carbide, including good adhesion, chemical stability and high density. In this study, the B_4C converter was deposited directly onto the aluminum tracks of the detector, with no air gap, in order to minimize the energy loss of the reaction products before they reach the sensitive volume. The converter layer was enriched to >96% ^{10}B [51], significantly increasing the probability of neutron capture and maximizing the number of (n,α) reactions. The thickness of the B_4C layer was varied in simulations to optimize the trade-off between maximizing neutron conversion efficiency and ensuring the escape of energetic α and ^{7}Li particles into the

sensitive region, as excessive thickness can lead to energy degradation before the particles reach the detection region. The performance of such thin films is strongly influenced by their thickness, density, and impurity content. Uniformity of the converter layer and minimization of contaminants are critical for consistent and efficient neutron detection, as demonstrated in large area detector prototypes utilizing B_4C coatings [51]. The specific configuration used for the converter based approach is illustrated in Figure 3.5, and the results of these simulations, including the impact of converter thickness, will be discussed in detail in the following sections.

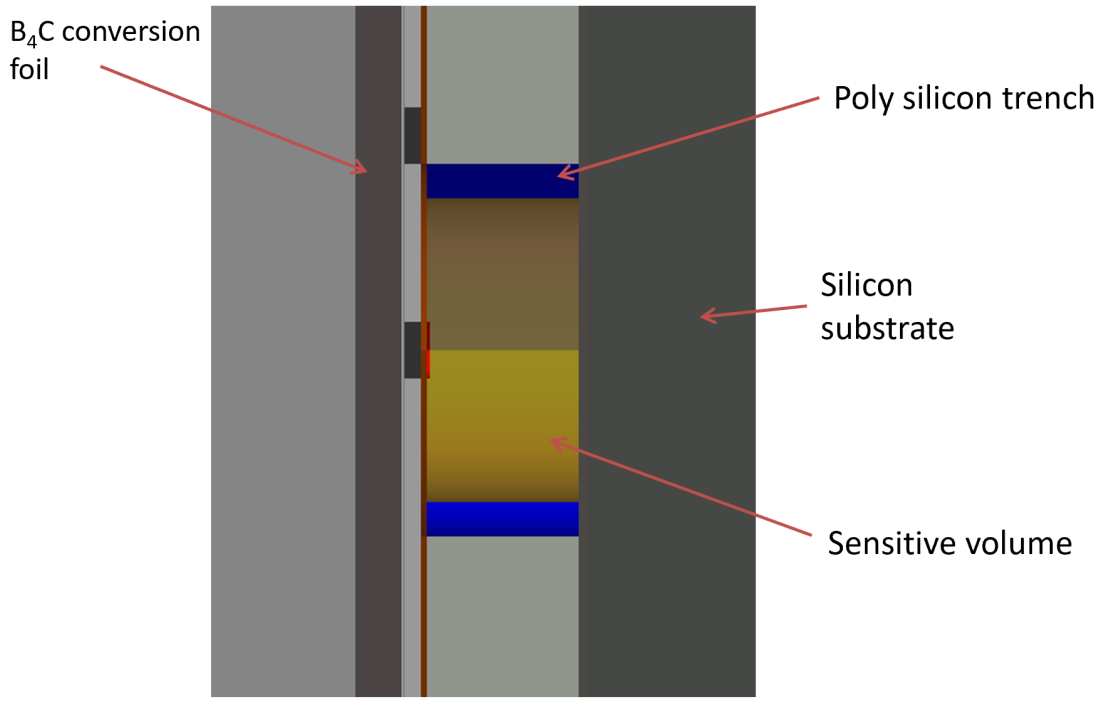

Figure 3.5: Schematic cross section of the microdosimeter structure featuring the B_4C conversion foil, polysilicon trench, silicon substrate and sensitive volume.

The thickness of the B_4C converter layer influences the balance between neutron capture efficiency and energy degradation of reaction products. Thicker converters enhance neutron absorption due to increased ^{10}B density but attenuate α and ^{7}Li particles, leading to higher rates of "stoppers" in the SVs. Conversely, thinner layers reduce energy loss, allowing more particles to escape as "crossers" with minimal attenuation, though at the cost of reduced neutron interaction probability. Simulations made by Vohradsky et al. [52] demonstrated that a 3 µm B_4C layer achieves the maximum neutron detection efficiency for thermal neutrons, while optimizing thickness to match particle ranges ensures maximal signal yield.

3.3.3. MicroPlus Design

The microdosimetry probe, shown in Figure 3.6, consists of a silicon microdosimeter connected to low noise front-end readout electronics, all encased within a PMMA waterproof sheath covered with Aluminium foil. This protective casing helps reducing radio frequency noise and enables reliable measurements in both water and PMMA of lineal energy down to 0.4 keV/µm. The system functions by measuring the charge collected in the silicon-on-insulator microdosimeter due to ionizing radiation interactions within its sensitive volumes.

The microdosimeter itself is mounted within a dual in line package (DIL), which securely connects to one end of the probe. To minimize radiation induced damage to the electronics, the probe circuit board, which is designed for low noise spectroscopy-based readout, is positioned 10 cm away from the detector outside the primary radiation field [53]. This spatial separation helps avoiding radiation damage and worsening of the readout electronics performance during prolonged exposure to radiation.

Furthermore, the probe incorporates a flexible design feature that allows selective connection of specific arrays, alternating even and odd rows of sensitive volumes, via configurable jumpers. This functionality is particularly effective in reducing the pile-up effect that can occur in high dose rate radiation fields, where multiple events may overlap within a single readout window. By enabling independent readout of alternating SV rows, the system improves event discrimination.

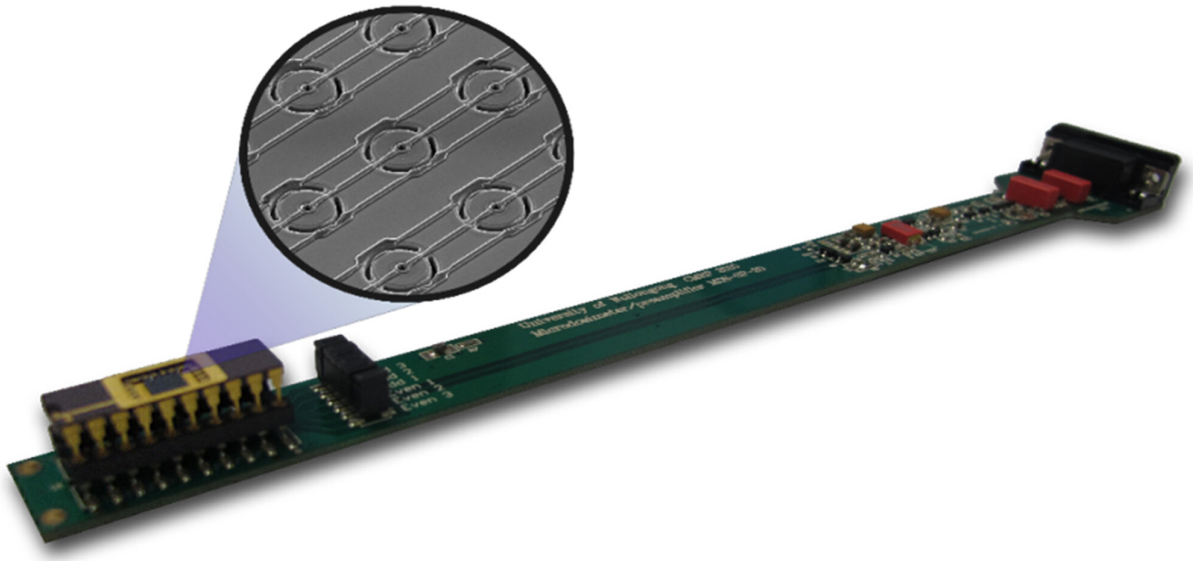

Figure 3.6: The MicroPlus probe with the Mushroom microdosimeter chip [53]

4 | NCEPT Results and discussion

This chapter presents and discusses the simulation results for the different microdosimeter configurations studied in the context of neutron capture enhanced particle therapy (NCEPT). The performance of the standard Mushroom SOI, the uniformly ^{10}B-doped sensitive volume and the B_4C converter designs are compared, focusing on neutron detection efficiency, energy deposition and the influence of key geometric parameters. The analysis highlights how each configuration affects the microdosimetric response.

4.1. Simulations setup

Simulations investigating the physical processes relevant to NCEPT therapy were performed using the Geant4 toolkit (version 11.03). The setup, including the Mushroom microdosimeter, was reconstructed in the simulation environment with attention paid to the modeling of overlayers and structural details, as described in [54][50]. This precise geometrical representation ensures that the microdosimeter's response in the simulated radiation field matches its behavior in experimental conditions.

To accurately capture the range of particle interactions expected in the therapy scenario, several physics lists were employed. Electromagnetic interactions were modeled using the G4EmLivermorePhysics List, which provides high precision modeling of low energy electromagnetic processes. For the simulation of hadronic interactions, both the Binary Intranuclear Cascade (BIC) and the Bertini Cascade models were utilized. The BIC model describes interactions between an incident projectile and individual nucleons within the target nucleus, treating their overlap as Gaussian wave functions. Meanwhile, the Bertini Cascade model simulates the intranuclear cascade process by representing the nucleus as a series of concentric density shells. For the treatment of elastic scattering of hadrons, the G4HadronElasticPhysicsHP package was used, with the High Precision (HP) model adopted for neutron interactions up to 20 MeV. This approach ensures accurate simulation of neutron transport and interactions, which are critical for secondary particle production.

To optimize computational efficiency while maintaining physical accuracy, the micro-

dosimeter was placed within a water region inside the water phantom. The Geant4 classes G4Region and G4ProductionCuts were employed to define distinct regions within the simulation geometry, each with thresholds for the production of secondary particles. This strategy limited the generation of secondary electrons primarily to the vicinity of the detector, thereby reducing unnecessary computational overhead in regions far from the sensitive volume. The production cut was set to 20 mm in the water phantom, 2 mm in the water window in front of the SOI chip and in the DIL package housing, 50μm in the printed circuit board (PCB) of the MicroPlus probe, 5 μm in the silicon and aluminum contacts surrounding the sensitive volumes and as low as 0.250 μm in the sensitive silicon volumes themselves. These range cuts correspond to energy thresholds for secondary electrons appropriate to each material and region, ensuring both computational efficiency and accurate modeling of energy deposition in the detector.

Region	Material	Range cut (μm)	Energy cut e^- (keV)
World	Air	20000	34.5
Phantom	Water	20000	4200
Water window	Water	2000	571
DIL	PMMA	2000	637
PCB	Al	50	87
SOI chip	Si	5	13
Sensitive volumes	Si	0.250	0.1

Table 4.1: Threshold cuts for secondaries production in the main regions of the simulation.

Throughout the simulation, the identity of all particles depositing energy within the detector was recorded. This allowed for a detailed analysis of the radiation field composition and the specific contribution of each particle type. Furthermore, if a secondary particle was produced within the sensitive volume, its energy deposition was attributed to the parent particle that entered the sensitive region from outside, ensuring a physically meaningful association between incident radiation and microdosimetric spectra.

4.1.1. Geometry

The simulations were performed using the Geant4 Monte Carlo toolkit to investigate the contribution of thermal neutrons in proton therapy and their enhancement effects on microdosimetric spectra. The simulation geometry, illustrated in Figure 4.2, consists of a water phantom irradiated by a monoenergetic 200 MeV proton beam traveling in the positive z direction. An SOI MicroPlus probe was positioned at the center of the phantom to maximize detection efficiency for thermal neutrons. The central placement of the detector was strategically chosen based on the thermal neutron flux distribution

within the phantom. As demonstrated in Figure 4.3, the thermal neutron yield exhibits a maximum around the phantom center due to the symmetrical geometry, with both HP and BERT physics models showing consistent behavior in this region. This positioning ensures optimal conditions for observing thermal neutron induced enhancements in the microdosimetric measurements.

The thermal neutrons in this configuration originate primarily from inelastic nuclear reactions between the incident proton beam and water nuclei, resulting in a relatively modest neutron production rate [55]. The primary nuclear reactions responsible for neutron production occur when the 200 MeV protons interact with both ^{16}O and hydrogen nuclei in the water phantom. The most significant contribution comes from proton induced nuclear reactions with ^{16}O, where multiple neutrons can be emitted depending on the available kinetic energy [56]. Additionally, proton interactions with hydrogen nuclei contribute through elastic and inelastic scattering processes, though to a lower extent.

The initially produced neutrons emerge with energies ranging from several MeV down to the keV range, as shown in Figure 4.1, requiring moderation to reach thermal energies ($< 0.025\ eV$). Water serves as an excellent moderating medium due to its high hydrogen content, which slows down fast neutrons through multiple elastic collisions with hydrogen nuclei. This thermalization process occurs over distances comparable to the phantom dimensions, with the neutron energy spectrum gradually shifting toward lower energies as neutrons diffuse through the water medium.

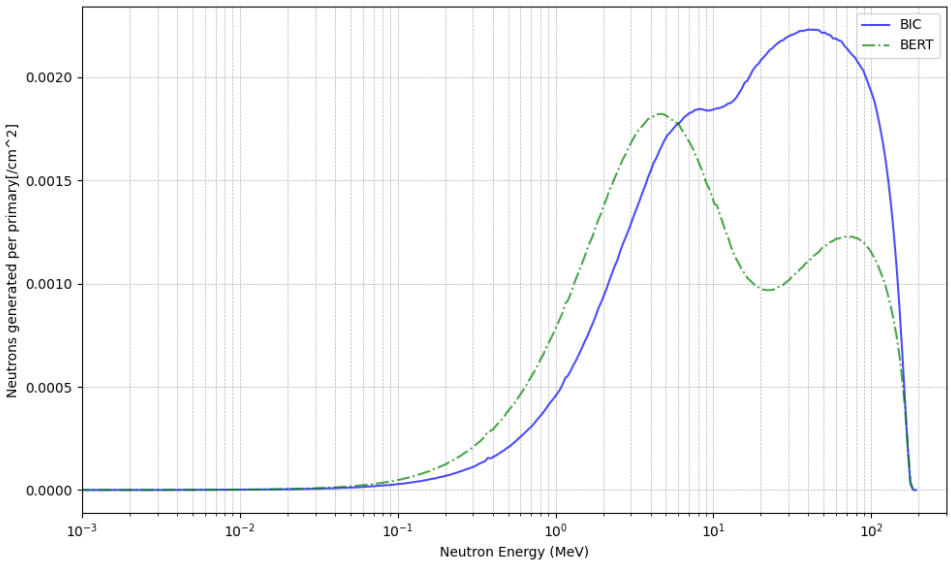

Figure 4.1: Energy spectrum of neutrons generated per primary proton in water, comparing BIC and BERT physics models as a function of neutron energy.

The neutron production rate is inherently modest because the cross sections for neutron producing reactions with 200 MeV protons, while measurable, are relatively small. However, the chosen geometry maximizes the probability of detecting these secondary neutrons and their potential contributions to the overall radiation field characteristics. The central positioning of the SOI MicroPlus probe exploits the build-up region where thermalized neutrons accumulate due to the combination of local production and diffusion. This placement ensures optimal sensitivity for measuring the thermal neutron component, which is crucial for understanding the complete radiation field composition in proton therapy environments and its biological implications through secondary nuclear reactions [57][58].

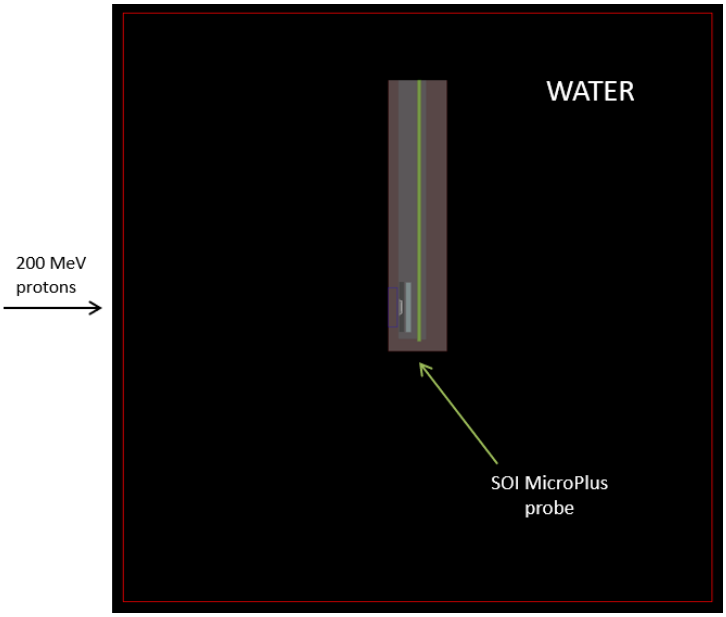

Figure 4.2: Schematic illustration of the simulation setup used to analyze the contribution of thermal neutrons in NCEPT.

The comparison between two different hadronic physics models is presented in both Figure 4.1 and Figure 4.3. This work employed the Bertini High Precision (BERT) model and the Binary Cascade High Precision (BIC) model to evaluate their impact on neutron production and thermalization characteristics. The analysis reveals differences in neutron production between the two models. The BERT model demonstrates an higher thermal neutron fluence, approximately double that of the BIC model, as evidenced in the depth distribution shown in Figure 4.3. This enhanced thermal neutron production is advantageous, as it increases the probability of $^{10}\mathrm{B}(n,\alpha)^{7}\mathrm{Li}$ reactions. Conversely, the neutron energy spectrum comparison in Figure 4.1 shows that the BIC model produces a higher yield of fast neutrons, particularly in the energy range above 1 MeV. While these fast

neutrons contribute to the overall neutron field, they require additional moderation to reach thermal energies suitable for boron capture reactions.

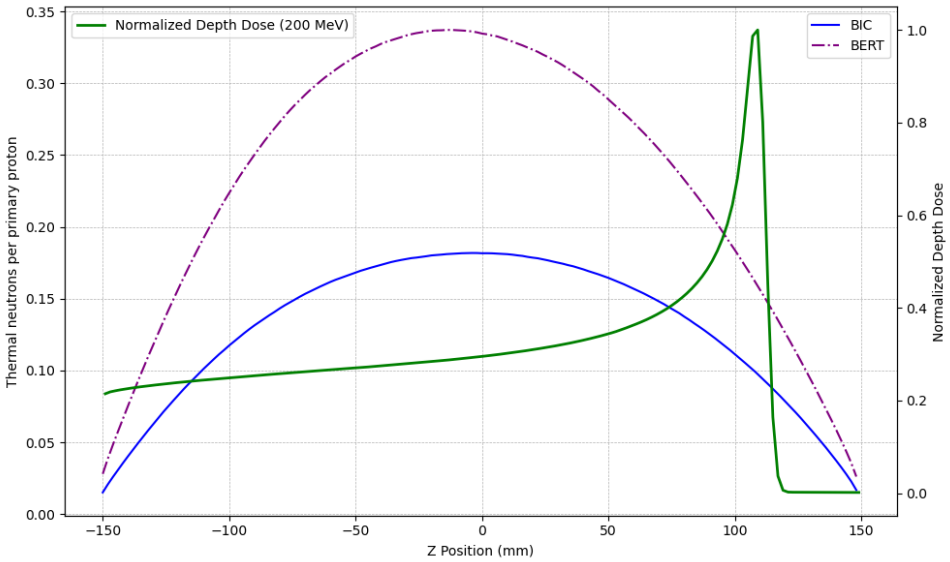

Figure 4.3: Thermal neutron yield per primary proton as a function of depth (BIC and BERT models), with normalized depth dose shown for reference.

However, the neutron yield remained insufficient to observe a meaningful contribution. To ensure a detectable signal, a larger neutron contribution in the proton beam was required by placing a 5 mm thick tungsten slab before the detector setup. An illustration of this configuration is visible in Figure 4.4, which shows the simulation setup with 200 MeV protons passing through the tungsten layer into the water medium where the SOI MicroPlus probe is positioned. The selection of tungsten is motivated by its high atomic number and density, which enhance the probability of spallation reactions and secondary neutron production when irradiated by energetic protons. Literature on tungsten spallation using 250 MeV protons indicates that the BERT HP physics module in GEANT4 tends to overestimate neutron production compared to experimental measurements [59].

The addition of the tungsten slab led to an increase in neutron yield, confirming its effectiveness as a neutron converter. Furthermore, the presence of tungsten alters the spatial distribution of thermal neutrons, shifting the maximum fluence closer to the beam entrance, as observed at approximately -90 mm in Figure 4.5. This shift is attributed to the moderation and production of neutrons within the dense tungsten layer, which results in a more pronounced thermal neutron peak near the entrance region. The probe position was thus selected at this maximum to optimize the detection of thermal neutrons and to enhance the contribution of these particles to the measured signal.

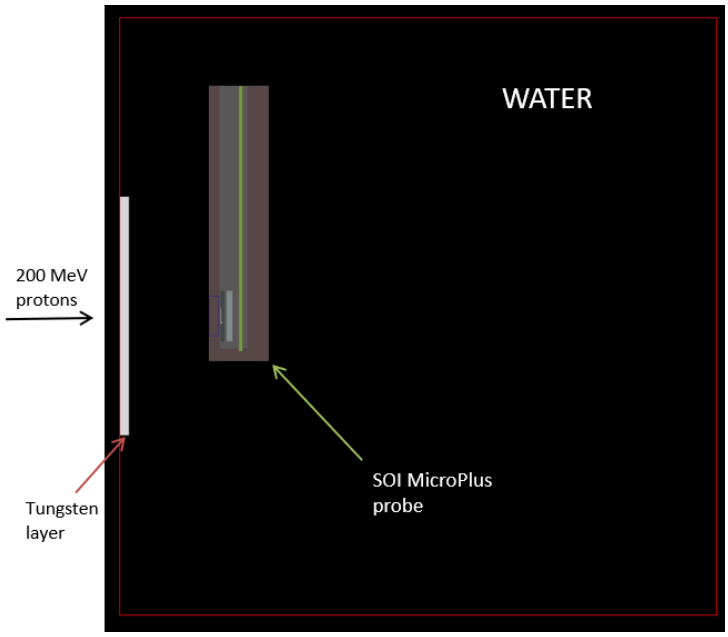

Figure 4.4: Schematic illustration of the simulation setup used to analyze the contribution of thermal neutrons with an additional tungsten slab.

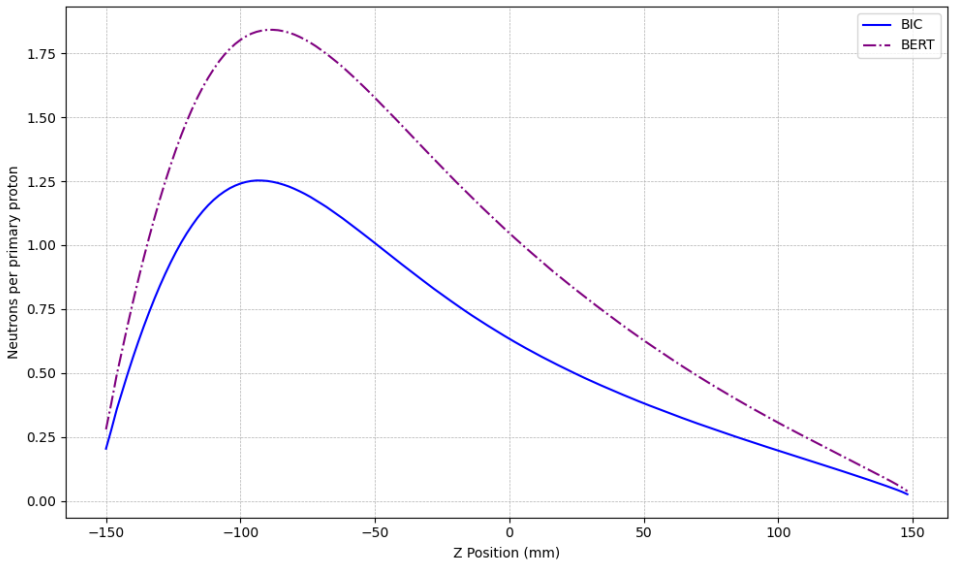

Figure 4.5: Thermal neutron yield per primary proton as a function of depth (BIC and BERT models) with an additional tungsten slab.

Examining Figure 4.5, the BERT model (dashed line) predicts a higher peak in thermal neutron yield compared to the BIC model (solid line). Both models show their maxima near -90 mm, but BERT estimates greater neutron production across the range. This aligns with literature noting BERT's tendency to overestimate neutron yields, a differ-

ence that underscores the importance of experimental validation when using Monte Carlo simulations for neutron production studies in tungsten targets.

4.1.2. Beams

The neutron energy spectra at the B_4C layer for varying beam sizes and configurations are presented in Figure 4.6. In both configurations, the beam maintains a rectangular cross section, with dimensions of 5×5 mm^2, 5×5 cm^2 and 10×10 cm^2, while the converter area (2.3×2.3 μm^2) remains negligible in comparison. The results indicate a strong dependence of the neutron spectrum on the beam size.

As the beam area increases, the number of neutrons per incident proton fluence reaching the converter rises across the entire energy range, with the greatest enhancement observed in the thermal energy region. This trend is attributed to the increased moderation path available for neutrons produced further from the converter, allowing a higher fraction to thermalize before reaching the sensitive volume. The effect is particularly evident as the thermal neutron peak becomes more prominent with the increase of the beam size.

The addition of a tungsten slab (Figure 4.6b) further amplifies the neutron yield at the converter. The total neutron fluence, especially in the thermal region, is nearly doubled relative to the configuration without tungsten. This enhancement is consistent across all beam sizes, indicating that the presence of high Z material upstream of the detector increases neutron production.

These findings demonstrate that the beam size is a critical parameter for optimizing the thermal neutron flux in the B_4C. Larger beams facilitate greater neutron moderation due to the increased distance from the production site to the region of interest, while materials such as tungsten can further enhance the overall neutron yield. The reduction in the relative contribution of protons to the microdosimetric spectra with increasing beam size is a consequence of the converter's small area relative to the beam, resulting in a lower probability of direct proton interactions within the sensitive volume. This effect is an important consideration for the interpretation of microdosimetric data and will be addressed in detail in subsequent sections.

Overall, the data confirm that increasing the beam area is an effective strategy for enhancing the thermal neutron component at the region of interest, thereby improving the conditions for $^{10}\mathrm{B}(n,\alpha)^{7}\mathrm{Li}$ reactions.

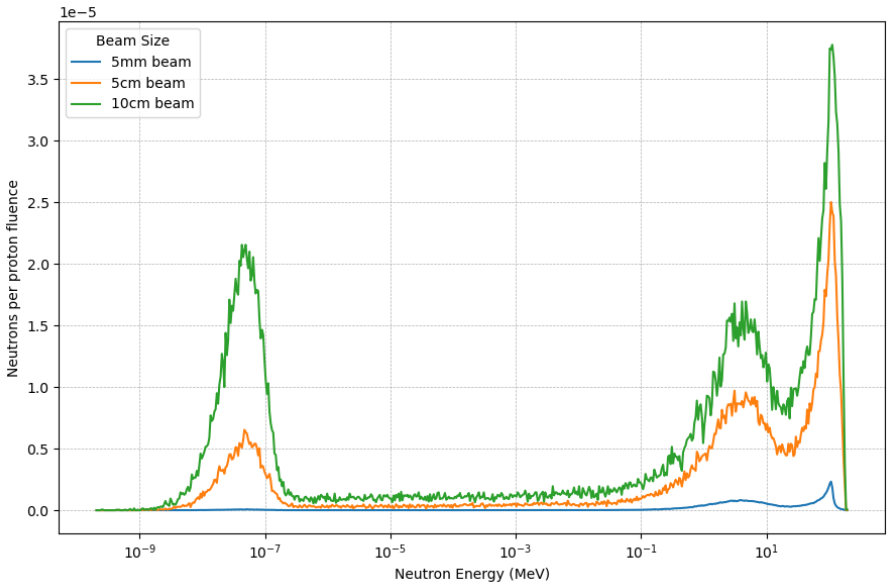

(a) Spectrum without tungsten slab

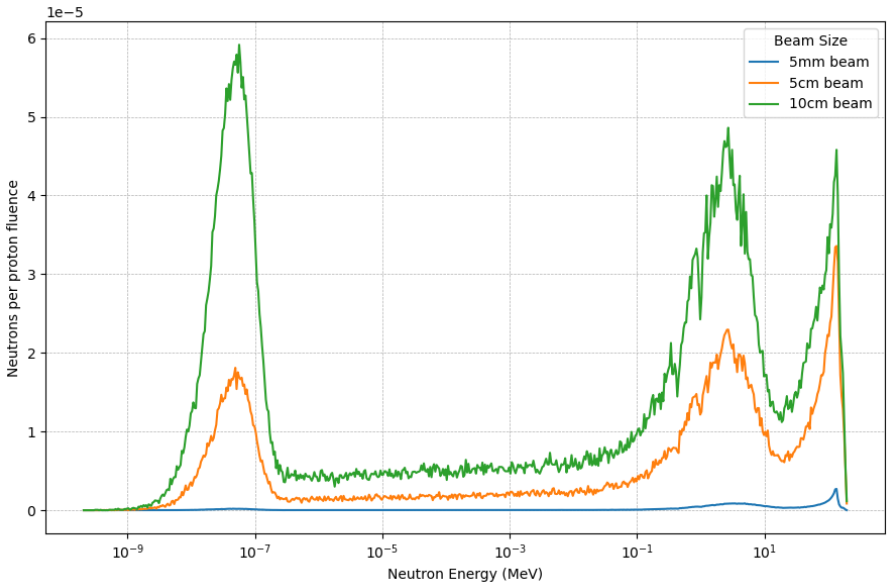

(b) Spectrum with the addition of a tungsten slab upstream of the converter.

Figure 4.6: Comparison of neutron energy spectra at the B_4C using the BERT model for varying beam sizes.

As previously discussed, the Bertini model produces a higher number of thermal neutrons compared to the Binary cascade model. Figure 4.7 presents the neutron energy spectra comparison between these two physics models for a 10×10 cm^2 beam, representing the optimal beam configuration for NCEPT applications. The results demonstrate that the Bertini model significantly enhances the thermal neutron flux in both configurations, while

the Binary cascade model generates a higher proportion of fast neutrons reaching the converter. The enhanced thermal neutron yield from the Bertini model directly benefits $^{10}\mathrm{B}(n,\alpha)^{7}\mathrm{Li}$ reaction optimization, making it the preferred choice for this application. However, the Binary cascade results provide valuable insight and will be included in the analysis to ensure robust conclusions.

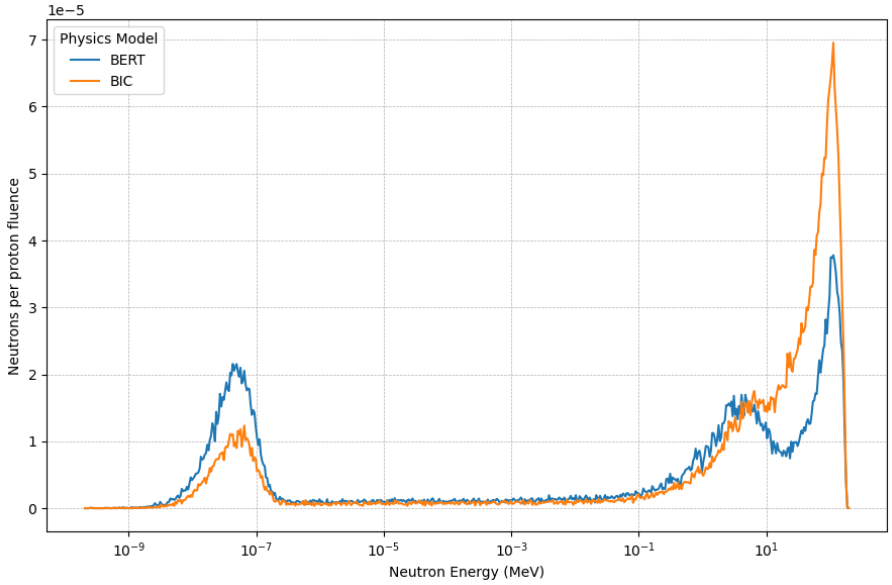

(a) Spectrum without tungsten slab.

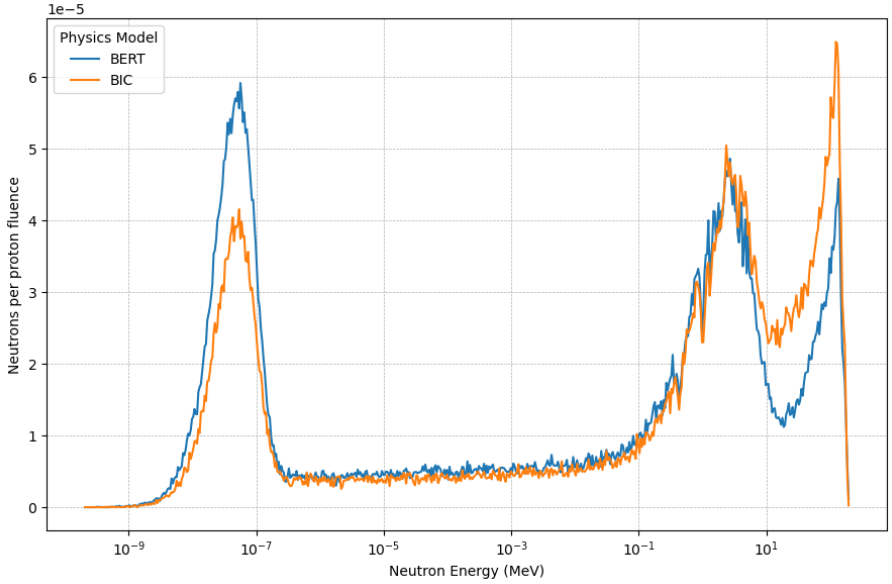

(b) Spectrum with the addition of a tungsten slab upstream of the converter.

Figure 4.7: Comparison of neutron energy spectra at the B_4C between the BERT and BIC physics models for a 10x10 cm^2 proton beam.

4.2. Microdosimetric analysis

4.2.1. Beams

The analysis of the microdosimetric spectra for different beam sizes highlights distinct patterns in the yd(y) vs log(y) distributions, particularly regarding the contributions from the $^{10}\mathrm{B}(n,\alpha)^{7}\mathrm{Li}$ reactions. As previously observed in the neutron spectra, increasing the beam size leads to a higher contribution in the microdosimetric spectra. This effect is evident in Figure 4.8, with the first row that presents the spectra for the SOI configuration with ^{10}B uniformly distributed in the sensitive volume. The second row illustrates the configuration with the B_4C converter, while the third row provides the standard SOI configuration as a reference.

The yd(y) vs log(y) plot offers a comprehensive view of the microdosimetric spectra. This approach effectively highlights the relative contributions from different radiation components. In these spectra, yd(y) accentuates the significance of high LET events, making it possible to clearly identify the signatures of specific nuclear reactions. Across all configurations, a prominent peak appears around 0.45 $keV/\mu m$, corresponding to protons. However, this feature is not the primary focus of the current analysis. More relevant is the region between 50 and 90 $keV/\mu m$, where a distinct contribution from α particles and ^{7}Li nuclei, generated by the capture reaction, is observed. The enhancement is more pronounced with larger beam sizes, as evidenced by higher peaks for the 10×10 cm^2 beam. In contrast, the standard SOI configuration, shows no such enhancement, as expected.

In the second column of Figure 4.8, the spectra reveal an even greater contribution in the presence of tungsten, which increases the number of thermal neutrons available for the capture reaction. This observation aligns with predictions and confirms that the α and ^{7}Li yield is maximized with the largest beam size. Given these findings, it is clear that the 10×10 cm^2 beam configuration provides the highest contribution from thermal neutron induced reactions, as evidenced by the pronounced peak in the high lineal energy region. Consequently, the remainder of the analysis will focus exclusively on the 10×10 cm^2 beam, as it offers the optimal conditions for investigating thermal neutron effects.

Additionally, increasing the beam size leads to a decrease in the proton peak intensity, as fewer protons reach the sensitive volume. This peak also shifts to slightly higher lineal energies, a result of the more complex trajectories protons must follow to reach the sensitive volume in the presence of a larger beam. The increased path length results in lower proton energies upon arrival, thereby increasing the energy deposited per unit length and causing the observed shift in the yd(y) spectra.

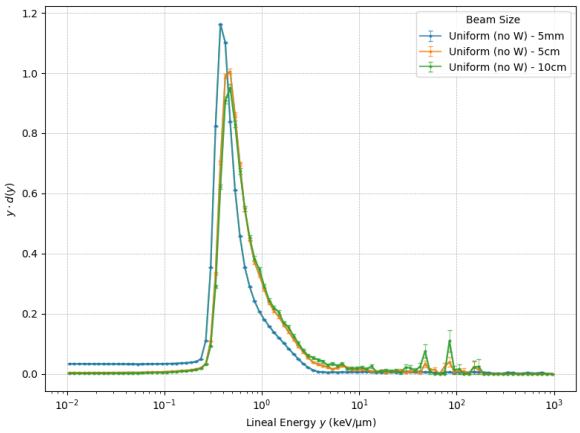

(a) Uniform boron configuration

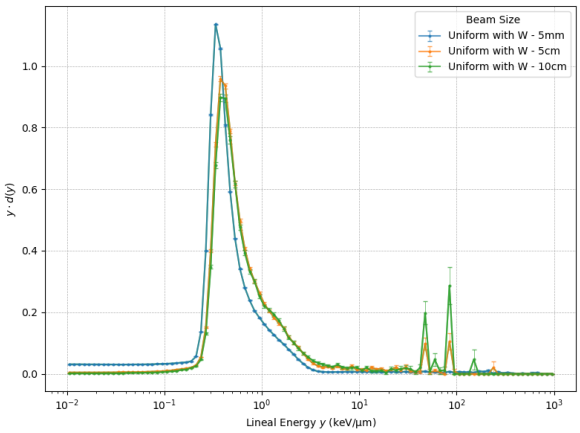

(b) Uniform boron configuration with tungsten

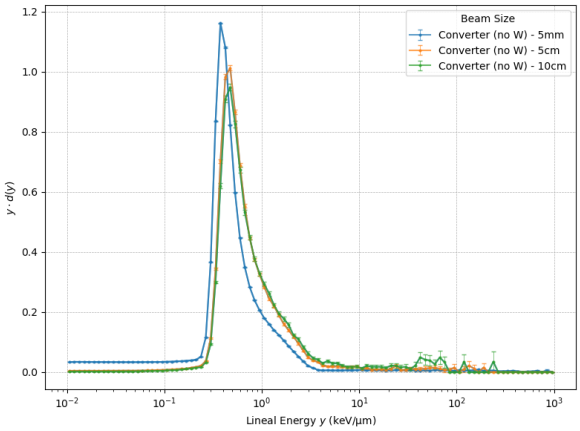

(c) $^{10}B_4C$ converter configuration

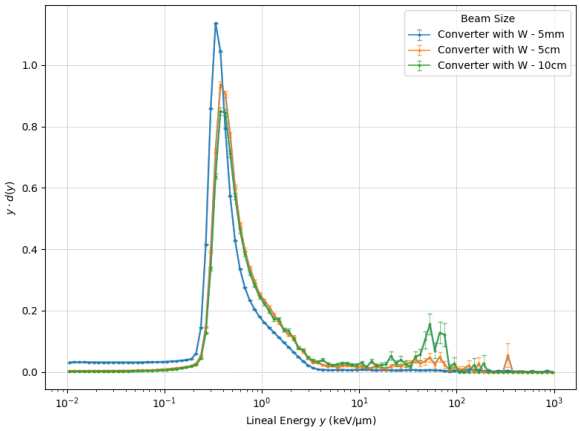

(d) $^{10}B_4C$ converter configuration with tungsten

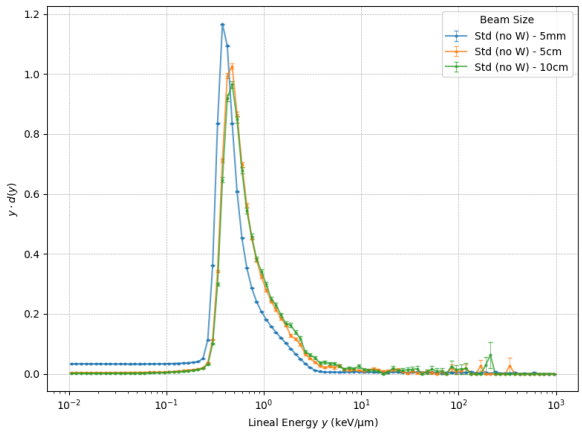

(e) Standard SOI configuration

Figure 4.8: Microdosimetric yd(y) vs log(y) spectra for different SOI detector configurations and beam sizes, simulated using the Bertini physics model.

4.2.2. Tunsgten contribution

From this point onward, all analyses are performed using the 10×10 cm^2 beam, as this configuration maximizes the contribution from thermal neutrons and thus the most relevant conditions for studying neutron capture effects. The main objective of this section is to highlight the advantage of introducing the tungsten slab, specifically by examining its effect on the microdosimetric yd(y) spectra. As previously described in section 3.2, all microdosimetric spectra have been converted to energy deposition in muscle using the single factor conversion method proposed by Bolst et al.[48] to ensure clinical relevance. Inspection of Figure 4.9 clearly shows that, in the lineal energy range between 50 and 80 $keV/\mu m$, the presence of tungsten leads to a notable enhancement in the spectra. This is attributed to the increased number of thermal neutrons available for the $^{10}\mathrm{B}(n,\alpha)^{7}\mathrm{Li}$ reaction, confirming the expected effect of the tungsten.

To quantify this enhancement, the dose weighted mean lineal energy, $\bar{y}_d$, was evaluated for both configurations. The results over the full spectrum (0.01–1000 $keV/\mu m$) are reported in Table 4.2, where it is evident that the addition of tungsten significantly increases $\bar{y}_d$ in both the $^{10}B_4C$ converter and the uniform ^{10}B configurations. However, values above 100 $keV/\mu m$, primarily due to heavy ion recoils, tend to increase both $\bar{y}_d$ and its associated uncertainty, despite not being directly related to neutron capture events.

For a more precise evaluation of the effect of thermal neutron capture, $\bar{y}_d$ was also calculated for the restricted spectrum between 0.1 and 100 $keV/\mu m$, thereby excluding both low-energy events that are negligible and high-energy recoils that are not relevant to the capture process. The results, reported in Table 4.3, confirm that the presence of tungsten leads to a substantial increase in $\bar{y}_d$ for both boron configurations.

	$^{10}B_4C$ converter	Uniform ^{10}B
No tungsten	3.8476 ± 0.7119	4.1110 ± 0.7539
Tungsten	6.9003 ± 0.6806	6.4510 ± 0.8733

Table 4.2: Comparison of $\bar{y}_d$ values, with and without tungsten slab, calculated over the full microdosimetric spectrum (0.01-1000 $keV/\mu m$).

	$^{10}B_4C$ converter	Uniform ^{10}B
No tungsten	2.911 ± 0.263	3.0808 ± 0.4164
Tungsten	6.080 ± 0.457	5.6509 ± 0.6655

Table 4.3: Comparison of $\bar{y}_d$ values, with and without tungsten slab, calculated over the 0.1-100 $keV/\mu m$ range.

This increase in $\bar{y}_d$ is particularly significant, as it directly impacts the calculations of the relative biological effectiveness via the microdosimetric kinetic model, which relies on accurate characterization of the high LET component of the radiation field.

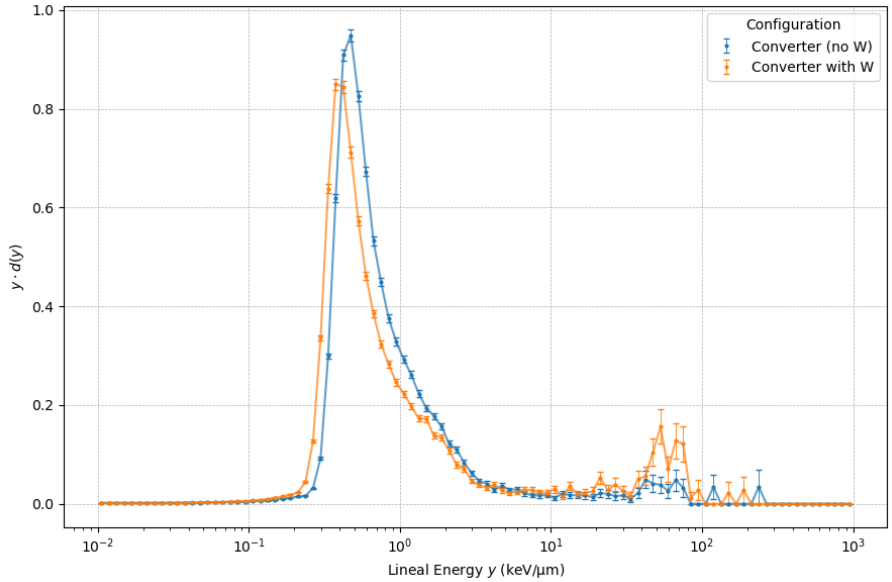

(a) $^{10}B_4C$ converter configuration

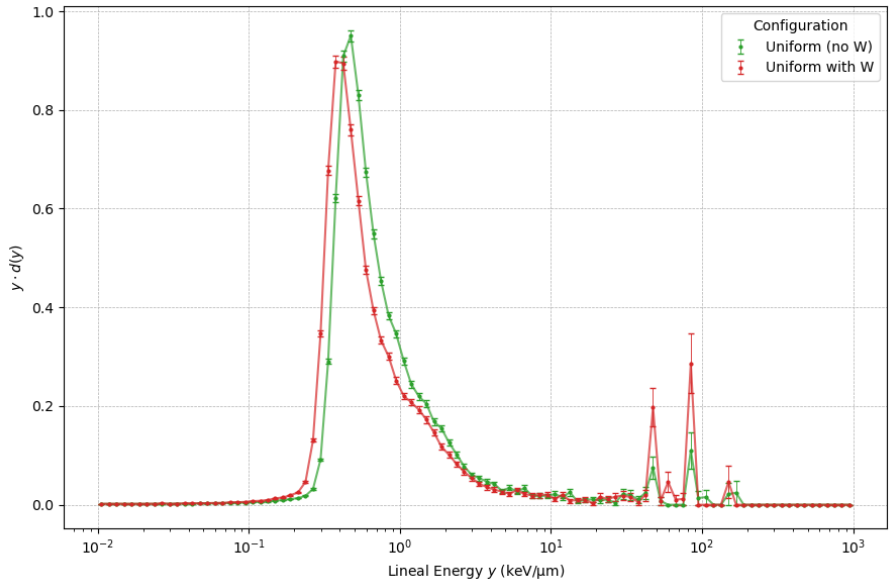

(b) Uniform boron configuration

Figure 4.9: Comparison of yd(y) vs log(y) spectra for different SOI detector configurations with and without tungsten, simulated using the Bertini physics model.

The introduction of tungsten not only enhances thermal neutron flux but also alters the proton energy. As shown in Figure 4.5 (tungsten setup) versus Figure 4.3 (water setup),

the position of maximum neutron fluence shifts due to the presence of tungsten. This spatial shift changes the placement of the SOI microdosimeter in a region where protons exhibit a different energy, resulting in a proton peak shift to lower lineal energies (0.35 $keV/\mu m$ with tungsten vs 0.45 $keV/\mu m$ without). Despite this spectral displacement, the y_d values remain higher in configurations with tungsten (Tables 4.2 and 4.3), confirming that thermal neutron capture products dominate the microdosimetric response.

The invariance of α and ^7Li peak positions in Figure 4.9b demonstrates that these high LET particles deposit energy independently of proton beam characteristics. Their lineal energy remains constant because it is determined by the fixed Q values of the $^{10}\mathrm{B}(n,\alpha)^7\mathrm{Li}$ reaction (α: 1.47 MeV, ^7Li: 0.84 MeV). Only the peak amplitude varies, reflecting the increased number of thermal neutrons produced thanks to tungsten spallation. This decoupling between proton energy and capture reaction validates the use of α and ^7Li peaks as direct indicators of thermal neutron performance in NCEPT microdosimetry.

These observations demonstrate that tungsten's primary benefit lies in amplifying thermal neutron capture events rather than modifying proton interactions. The y_d enhancement stems from increased number of reactions.

4.2.3. Configurations

The detailed analysis now examines the microdosimetric characteristics of different detector configurations and their biological implications. The comparison between the three configurations in the standard water environment without tungsten is presented in Figure 4.10. The full spectrum analysis in Figure 4.10a reveals minimal differences between configurations due to the limited thermal neutron flux available for boron neutron capture reactions. However, the focused spectral analysis in Figure 4.10b reveals differences in the relevant 30-100 $keV/\mu m$ range. The standard SOI configuration exhibits negligible contribution in this region, with values approaching zero within uncertainties, confirming the absence of boron capture signatures. In contrast, the uniform boron configuration displays distinct peaks at 85 $keV/\mu m$ and 50 $keV/\mu m$, corresponding to α particles and ^7Li nuclei from the $^{10}\mathrm{B}(n,\alpha)^7\mathrm{Li}$ reaction, respectively.

Regarding the $^{10}B_4C$ converter configuration, a notable degradation in the spectral quality of the α and ^7Li contributions is observed, manifesting as broadened peaks compared to the uniform boron distribution. This spectral broadening arises from the energy loss experienced by the reaction products as they traverse the converter material before reaching the sensitive volume. The finite thickness of the $^{10}B_4C$ layer causes the initially monoenergetic α particles and ^7Li nuclei to undergo different energy degradation depending on

their emission depth and angle within the converter film. Consequently, the sharp peaks characteristic of the uniform configuration become smeared across a broader energy range, reducing the spectral resolution for microdosimetric analysis.

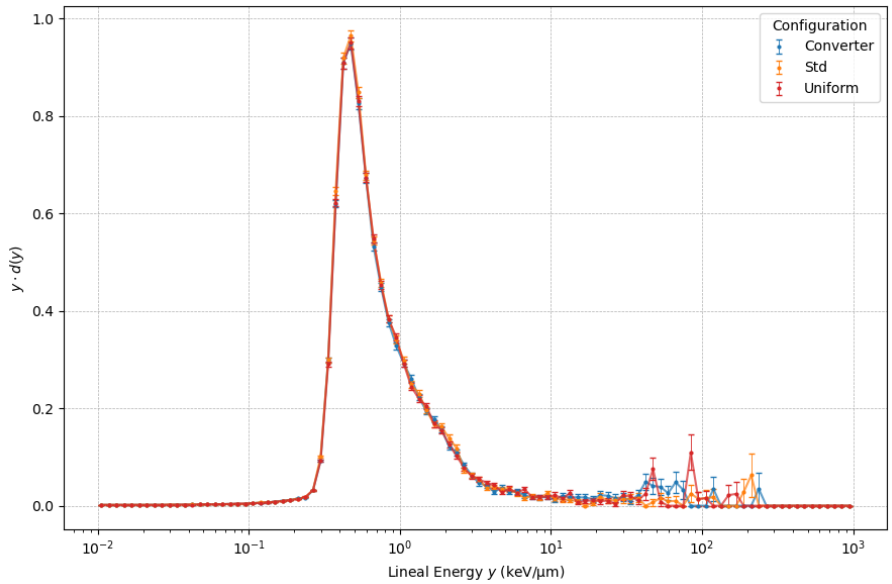

(a) Full microdosimetric spectra

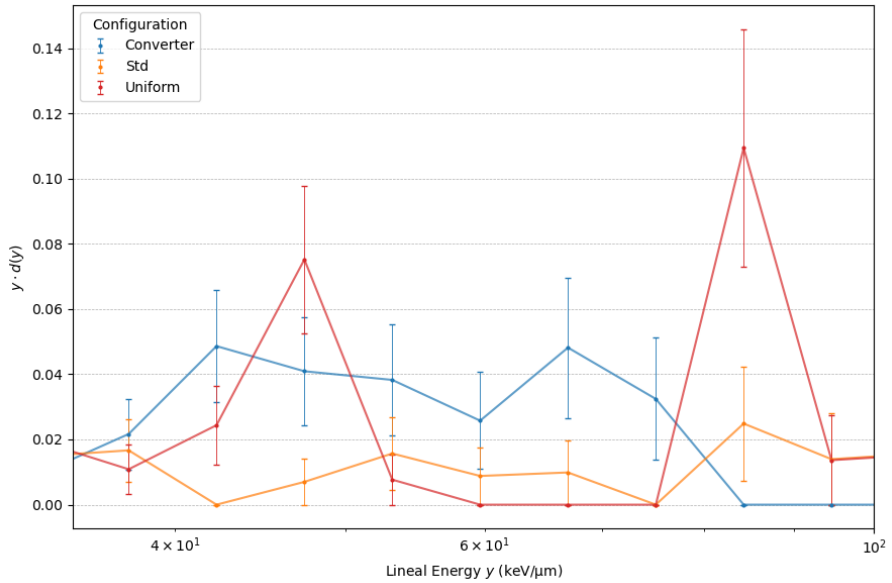

(b) Focused view of the microdosimetric spectra

Figure 4.10: Comparison of the microdosimetric spectra for three SOI configurations without tungsten, simulated using the Bertini physics model for a 10×10 cm^2 proton beam.

A comparison of the $\bar{y}_d$ values in the reduced range of 0.1–100 $keV/\mu m$ (see Table 4.4)

demonstrates an enhancement in energy deposition due to the $^{10}\mathrm{B}(n,\alpha)^{7}\mathrm{Li}$ reactions, even in the absence of a tungsten slab. Both the $^{10}B_4C$ converter and the uniform ^{10}B configurations exhibit higher $\bar{y}_d$ values, exceeding the standard SOI by more than 50%. This increase in $\bar{y}_d$ reflects a greater production of high LET particles, which are well known for their capacity to induce complex DNA damage and enhance the RBE of radiation therapy [60]. A closer examination of $\bar{y}_d$ values for the two configurations reveals that, despite differences in their yd(y) spectral distributions (Figure 4.10), their overall $\bar{y}_d$ values are statistically indistinguishable within the provided uncertainties. The overlap in error bars indicates that the apparent difference is not statistically significant.

Configuration	$\bar{y}_d$ $(keV/\mu m)$
$^{10}B_4C$ converter	2.911 ± 0.263
Uniform ^{10}B	3.0808 ± 0.4164
Standard SOI	1.93 ± 0.2698

Table 4.4: $\bar{y}_d$ values for each configuration, calculated over the 0.1–100 $keV\mu m$ range, without a tungsten slab.

The subsequent analysis focuses on configurations where upstream tungsten placement enhances thermal neutron generation. The standard SOI detector is excluded from this comparison, as its lack of ^{10}B renders it insensitive to thermal neutron flux variations; its spectral response remains unchanged regardless of tungsten presence. The analysis can concentrate on configurations where tungsten's capabilities can impact the microdosimetric spectra. By inspecting only configurations containing ^{10}B, the analysis directly correlates the thermal neutron flux amplification with more α and ^{7}Li generated. When comparing the two configurations in the presence of a tungsten slab, the yd(y) spectra exhibit distinct features (Figure 4.11). The uniform ^{10}B configuration produces sharp peaks in the spectrum, as the reaction products generated within the sensitive volume deposit their energy immediately and are efficiently detected. In contrast, the $^{10}B_4C$ converter, placed before the sensitive volume, causes the reaction products to lose some energy before reaching the detection region, resulting in a broader spectrum. The $\bar{y}_d$ values for the two configurations with tungsten are shown in Table 4.5.

Configuration	$\bar{y}_d$ $(keV/\mu m)$
$^{10}B_4C$ converter	6.080 ± 0.457
Uniform ^{10}B	5.6509 ± 0.6655

Table 4.5: $\bar{y}_d$ values for each configuration, calculated over the 0.1–100 $keV/\mu m$ range, with a tungsten slab.

Although the converter configuration shows a slightly higher value, the difference is within

the uncertainties, indicating that both configurations have comparable results in terms of enhancement induced by the $^{10}\mathrm{B}(n,\alpha)^{7}\mathrm{Li}$ reactions.

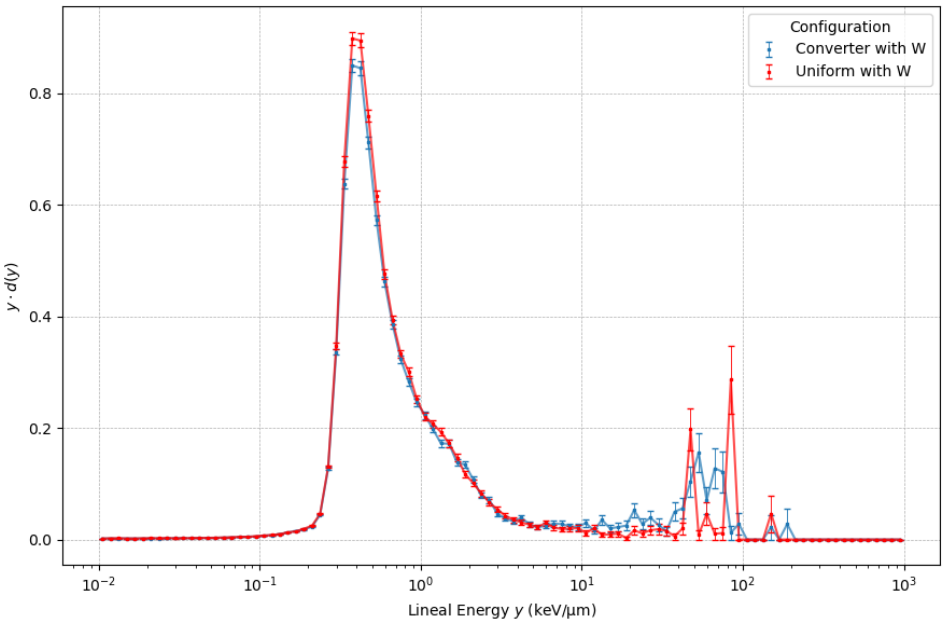

Figure 4.11: Comparison of yd(y) vs log(y) spectra for two SOI configurations with tungsten slab, simulated using the Bertini physics model for a 10×10 cm^2 proton beam.

The microdosimetric yd(y) spectra with individual particle contributions across the full energy range are presented in Figure 4.12. The distinct peak at 0.35 $keV/\mu m$ originates exclusively from primary protons traversing the sensitive volume and depositing energy. In the uniform boron configuration (Figure 4.12a), two well separated sharp peaks are clearly distinguishable in the relevant 30-100 $keV/\mu m$ range. The higher lineal energy peak corresponds to α particles produced by the $^{10}\mathrm{B}(n,\alpha)^{7}\mathrm{Li}$ reaction, while the lower energy peak is attributed to ^{7}Li nuclei. These sharp spectral features reflect the immediate energy deposition of reaction products generated within the sensitive volume itself. Conversely, the $^{10}B_4C$ converter configuration (Figure 4.12b) exhibits a broadened peak attributed primarily to α particles. This broadening occurs because the α particles must traverse matter before reaching the sensitive volume, resulting in a range of energies upon detection due to varying energy losses along their paths. The ^{7}Li peak is substantially suppressed and nearly disappears in this configuration. This attenuation is explained by the higher atomic number of lithium compared to helium, which results in greater energy loss per unit path length through the material, making it less probable for ^{7}Li nuclei to reach the sensitive volume with sufficient energy for detection.

An important observation is that all spectral events above 100 $keV/\mu m$ are associated

with heavy ion recoils from neutron elastic scattering processes. These high LET events, while present, are not relevant to the NCEPT analysis. This finding validates the decision to restrict the evaluation of $\bar{y}_d$ values to the 0.1-100 $keV/\mu m$ range, thereby excluding contributions from recoil hadrons and focusing specifically on the therapeutically relevant boron capture products.

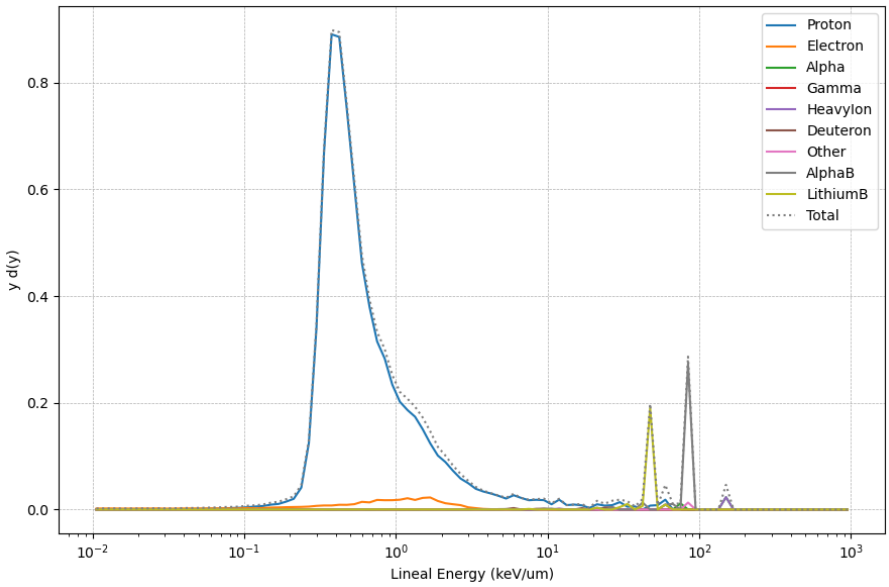

(a) Uniform boron configuration

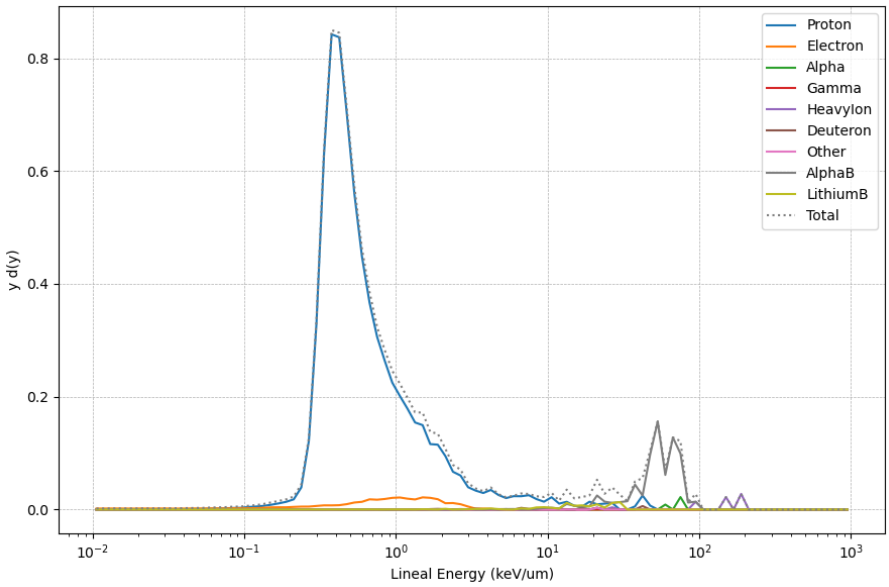

(b) $^{10}B_4C$ converter configuration

Figure 4.12: yd(y) vs log(y) spectra with tungsten highlighting contributions from different particle types, simulated using the Bertini physics model for a 10×10 cm^2 proton beam.

4.2.4. Physics models

In this section, a comparative analysis between the Bertini and Binary Cascade physics models is presented, focusing on their influence on microdosimetric spectra and the resulting $\bar{y}_d$ values across various detector configurations. All previous results were obtained using the Bertini physics list, but for a more comprehensive understanding, both models are now evaluated side by side. It is important to note that, in the absence of experimental data, a direct benchmarking of the two models to determine which better reflects reality is not possible. Nevertheless, it has been previously established (subsection 4.1.1) that the Bertini model tends to overestimate the production of thermal neutrons, which in turn enhances the contribution from the $^{10}\mathrm{B}(n,\alpha)^{7}\mathrm{Li}$ reactions. A detailed comparison of the microdosimetric spectra for the uniform and $^{10}B_4C$ converter configurations, as illustrated in Figure 4.13 and Figure 4.14, reveals that the differences between the two physics models are less pronounced than those observed in the neutron energy spectra at the converter. This suggests that, while the underlying neutron spectra differ, the overall microdosimetric response remains consistent between the two models.

To quantitatively assess these differences, Table 4.6 presents the $\bar{y}_d$ values obtained for each configuration using both physics models, calculated over the 0.1–100 $keV/\mu m$ range. In general, the values are very similar across the two models. The most notable distinction appears in the cases containing tungsten, where the $\bar{y}_d$ values are smaller for the Binary Cascade model. However, these differences remain within the statistical uncertainties, making it difficult to draw definitive conclusions about the superiority of either model.

Configuration	Bertini Cascade	Binary Cascade
Standard SOI	1.93 ± 0.2698	2.002 ± 0.2662
$^{10}B_4C$ without W	2.911 ± 0.263	2.759 ± 0.261
Uniform ^{10}B without W	3.0808 ± 0.4164	3.2956 ± 0.4477
$^{10}B_4C$ with W	6.080 ± 0.457	5.192 ± 0.413
Uniform ^{10}B with W	5.6509 ± 0.6655	4.6849 ± 0.5945

Table 4.6: $\bar{y}_d$ values for each configuration, calculated over the 0.1–100 $keV/\mu m$ range

Examining the microdosimetric spectra further, Figure 4.13b shows that the two peaks associated with α particles and ^{7}Li ions exhibit different intensities between the models, whereas in Figure 4.14b the distinction is less clear. Additionally, across all spectra, a higher number of heavy ion recoils is observed when using the BIC model. This phenomenon could be attributed to random statistical fluctuations, as such recoil events are rare but can significantly influence the $\bar{y}_d$ values. For this reason, the analysis was restricted to the reduced range of 0.1–100 $keV/\mu m$, ensuring that the results are not affected

by these sporadic events.

In summary, while the Bertini and Binary Cascade models yield similar $\bar{y}_d$ values across most configurations, subtle differences, particularly in the tungsten cases and in the intensities of peaks in the microdosimetric spectra, highlight the need for further investigation, ideally supported by experimental data, to fully understand the implications of model choice in microdosimetric simulations.

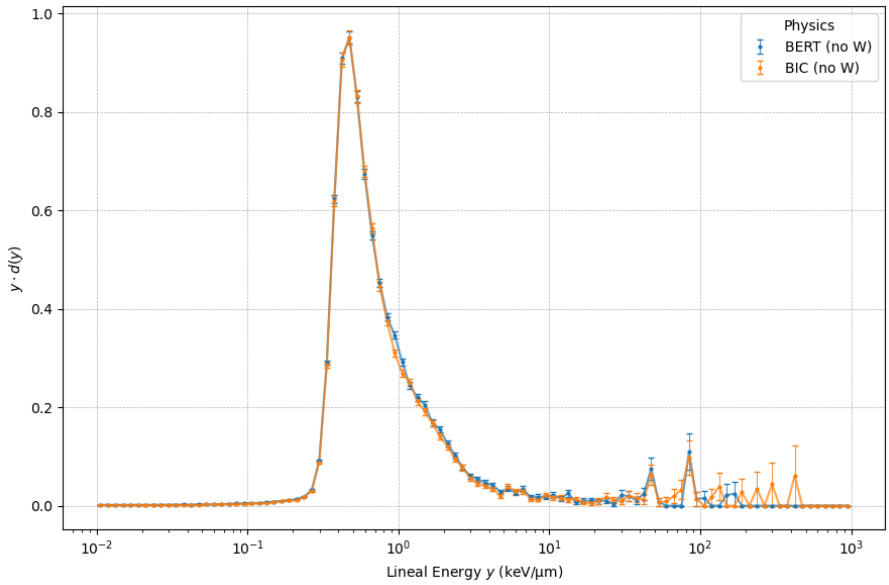

(a) Without tungsten

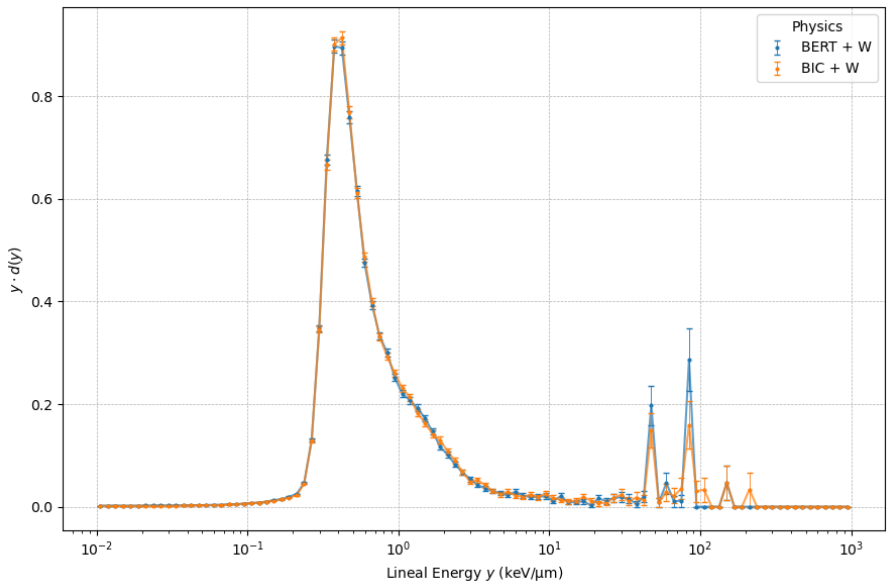

(b) With tungsten

Figure 4.13: Comparison of yd(y) spectra for the uniform configuration, emphasizing the differences between the BIC and BERT physics models for a 10×10 cm^2 proton beam.

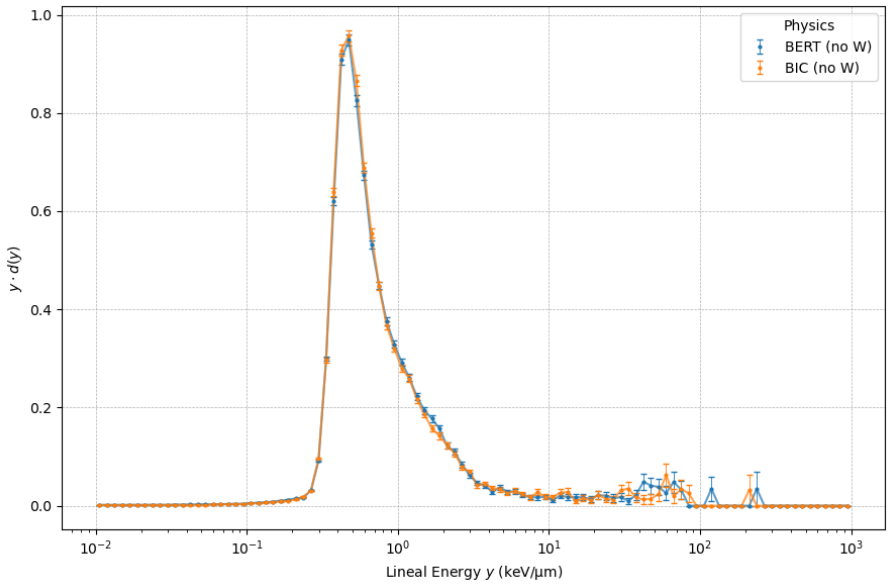

(a) Without tungsten

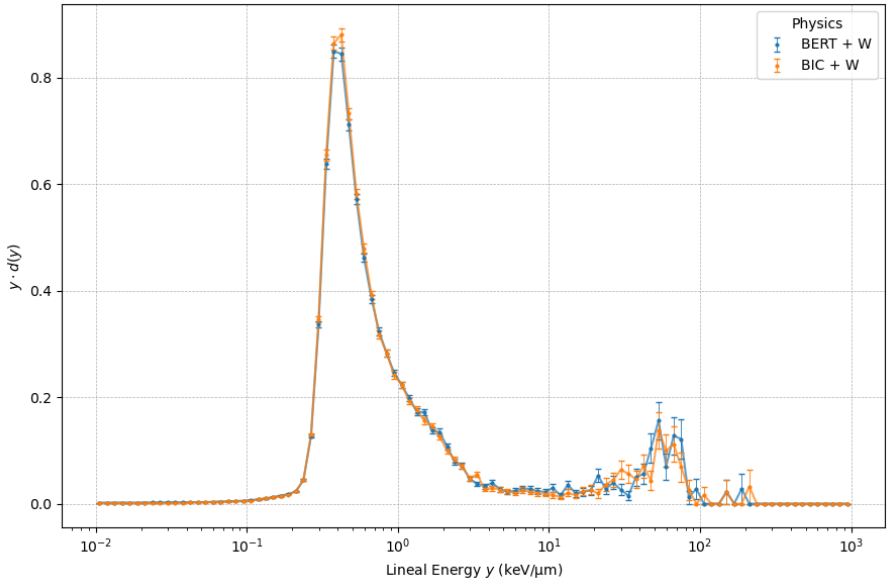

(b) With tungsten

Figure 4.14: Comparison of microdosimetric spectra for the $^{10}B_4C$ configuration, emphasizing the differences between the BIC and BERT physics models for a 10×10 cm^2 proton beam.

4.3. Converter thickness

This section examines the impact of varying $^{10}B_4C$ converter thickness (0.5, 1, and 3 μm) neutron detection performance and detection efficiency, building on earlier simulations that used a 1 μm baseline. Thinner converters are theorized to reduce energy loss of boron neutron capture products, potentially increasing sensitive volume crossings by minimizing self absorption within the converter material [52]. However, this comes with a trade-off: reduced converter thickness decreases the total number of $^{10}\mathrm{B}(n,\alpha)^7\mathrm{Li}$ reactions, while thicker converters increase reaction yield but enhance energy dissipation through ionization losses [52]. To this end, simulations were performed with converter thicknesses of 0.5 μm and 3 μm in addition to the baseline, allowing for a direct comparison of their effects.

The physical ranges of the reaction products are central to this analysis. In silicon, the 1.47 MeV alpha particles and 0.84 MeV ^7Li ions produced by the $^{10}\mathrm{B}(n,\alpha)^7\mathrm{Li}$ reaction have ranges of approximately 5.26 μm and 2.46 μm, respectively [34]. In $^{10}B_4C$ itself, the 1.47 MeV α range reduces to approximately 3.43 μm. Given that the SV height is 10 μm, most reaction products are stopped within the SV [52], but the fraction of products that reach the SV is sensitive to the converter thickness.

Reducing the converter thickness inevitably decreases the total number of neutron capture reactions, resulting in fewer generated α and ^7Li particles. However, a thinner layer allows a higher proportion of these particles to escape the converter with greater kinetic energy, increasing their probability of reaching the SV. Conversely, increasing the converter thickness boosts the total reaction yield, but most generated particles are absorbed within the converter itself and those that do emerge have lost more energy due to ionization losses in the thicker material. This trade-off underscores the need for careful optimization of the converter thickness to balance neutron capture efficiency against particle escape probability.

Microdosimetric spectra, as shown in Figure 4.15, reveal that variations in converter thickness do not produce significant differences from a purely microdosimetric perspective: the spectra for 0.5, 1, and 3 μm converters overlap within statistical uncertainties, both with and without tungsten present. This indicates that, at least within the explored thickness range and SV geometry, the energy deposition patterns in the SV are not strongly dependent on converter thickness.

However, the underlying particle statistics, such as the number of α and $^7\mathrm{Li}$ ions generated, those escaping the converter and those ultimately detected in the SV, can differ with

thickness. Thicker converters generate more reaction products, but self-absorption within the film limits the number that escape and are detected, leading to a nonlinear relationship between thickness and detection efficiency. Thinner converters, while producing fewer reaction products overall, allow a higher fraction to escape and retain more kinetic energy, which can be advantageous to help those particles in reaching the SVs.

The detailed tables provide a quantitative foundation for understanding how varying the thickness of the $^{10}B_4C$ converter film impacts particle generation, escape, detection and energy deposition, both with and without a tungsten slab. As the converter thickness increases from 0.5 to 3 μm, there is a pronounced rise in the number of both α particles and ^7Li nuclei generated, as evidenced by the jump from 1,270 to 12,754 α particles and from 1,266 to 11,478 ^7Li nuclei in the BERT model without tungsten (Table 4.7). However, this increase in generation does not translate proportionally into the number of particles escaping the converter or being detected in the SVs. The number of escaping and detected particles grows much more slowly, and for ^7Li, detection actually peaks at 1 μm and then declines with further increases in thickness. This phenomenon is a consequence of self-absorption within the converter: as the film thickens, a greater fraction of the reaction products are stopped before they can exit the film or reach the SVs, with ^7Li, being heavier and having a shorter range, particularly affected.

Hadronic model	Thickness [μm]	α gen	^{7}Li gen	α out	^{7}Li out	α det	^{7}Li det
BERT	0.5	1270	1266	392	371	35	26
	1	3207	3182	731	568	76	30
	3	12754	11478	1226	508	89	23
BIC	0.5	761	795	257	211	28	9
	1	1715	1764	446	296	43	15
	3	7482	6653	702	339	58	11

Table 4.7: Both models without tungsten slab

Hadronic model	Thickness [μm]	α gen	^7Li gen	α out	^{7}Li out	α det	^7Li det
BERT	0.5	3783	3864	1232	1072	118	79
	1	9043	9094	2058	1596	190	83
	3	37538	33752	3587	1656	273	75
BIC	0.5	2797	2804	920	760	87	41
	1	6804	6806	1551	1172	147	63
	3	27537	24672	2670	1169	206	45

Table 4.8: Both models with tungsten slab

When a tungsten slab is introduced, absolute numbers for generation, escape and detection all increase, as illustrated in Table 4.8. This reflects the enhanced neutron generation

and capture. Yet, the qualitative trends remain unchanged. Detected α particles continue to increase with thickness, but the detected ^{7}Li nuclei still peak at 1 μm and then decrease, confirming that self-absorption and limited particle range are the dominant factors regardless of the neutron environment.

The microdosimetric response, as measured by the $\bar{y}_d$, does not increase monotonically with converter thickness. Without tungsten, the highest $\bar{y}_d$ values are observed at 1 μm for both BERT and BIC models, with a slight decline at 3 μm. The presence of tungsten does not significantly alter this pattern and all $\bar{y}_d$ values across thicknesses remain within overlapping uncertainties. This stability indicates that the increased number of detected particles at greater thicknesses is offset by a decrease in their average energy, resulting in a nearly constant microdosimetric impact.

	0.5 μm	1 μm	3 μm
BERT	2.578 ± 0.261	2.911 ± 0.263	2.872 ± 0.244
BIC	2.623 ± 0.268	2.759 ± 0.261	2.480 ± 0.228

Table 4.9: $\bar{y}_d$ values no tungsten

	0.5 μm	1 μm	3 μm
BERT	5.590 ± 0.462	6.080 ± 0.457	5.639 ± 0.415
BIC	5.111 ± 0.460	5.192 ± 0.413	5.413 ± 0.438

Table 4.10: $\bar{y}_d$ values with tungsten

The energy deposition data further clarify this effect. For both α particles and ^{7}Li nuclei, the average energy deposited in the SVs decreases or remains nearly constant as the converter thickens. For example, the average energy deposited by α particles in the BERT model without tungsten drops from 831.7 keV at 0.5 μm to 494.1 keV at 3 μm, as shown in Table 4.11. For ^{7}Li, the deposited energy fluctuates within a narrow range, reflecting the fact that only those ^{7}Li nuclei generated very close to the film boundary can escape and deposit energy, while those born shallower in the film are stopped before reaching the SVs. This underscores the limited range of both reaction products in solids and the importance of geometric optimization.

Taken together, these results demonstrate that while increasing the $^{10}B_4C$ film thickness boosts the raw number of neutron capture events, the benefits for detection efficiency and microdosimetric response are limited by the self-absorption of reaction products and the reduced energy of those that do escape. The optimal configuration, especially for maximizing $\bar{y}_d$ and ^{7}Li detection, appears to be around 1 μm. Thicker films do not provide additional microdosimetric benefit and may even reduce performance for certain metrics,

as additional reaction products are increasingly absorbed before contributing to the detector signal. This balance is crucial for optimizing neutron detector design, particularly in applications such as NCEPT, where both detection efficiency and biological relevance of the dose are critical. The data reinforce that the interplay between particle range, film thickness, and detector geometry fundamentally governs the microdosimetric outcome, and that beyond a certain point, increasing converter thickness yields diminishing or even negative returns for detection.

Hadronic model	Thickness [μm]	Energy dep by α [keV]	Energy dep by ^7Li [keV]
BERT	0.5	831.7	204.8
	1	614.3	214.7
	3	494.1	201.4
HP	0.5	762.8	285.2
	1	719.2	198.7
	3	516.7	305.1

Table 4.11: Avarage energy deposited by α and ^7Li particles without tungsten slab.

Hadronic model	Thickness [μm]	Energy dep by α [keV]	Energy dep by ^7Li [keV]
BERT	0.5	829.5	272.4
	1	673.5	195.7
	3	509.6	234.1
HP	0.5	830.2	266.4
	1	694.0	196.1
	3	546.2	243.4

Table 4.12: Avarage energy deposited by α and ^7Li particles with tungsten slab.

Both hadronic models show consistent trends where particle generation and detection increase with converter thickness, with BERT consistently producing higher particle counts than BIC across all configurations. The $\bar{y}_d$ values reveal the superior of BERT signal amplification, though both models show optimal performance at 1 μm thickness. BERT exhibits a higher particle yield and signal generation, particularly in the presence of tungsten, as a result of its greater thermal neutron flux and the resulting increase in neutron capture reactions. In contrast, BIC provides slightly more consistent energy deposition for ^7Li, despite producing fewer reaction events overall.

In summary, while microdosimetric spectra appear largely insensitive to converter thickness within the studied range, the number and energy of detected reaction products are influenced by this parameter. Optimizing the $^{10}B_4C$ converter thickness is essential for achieving the desired balance between neutron capture probability and the efficient transport of reaction products to the SV, with the optimal value depending on the specific

detector geometry and application requirements.

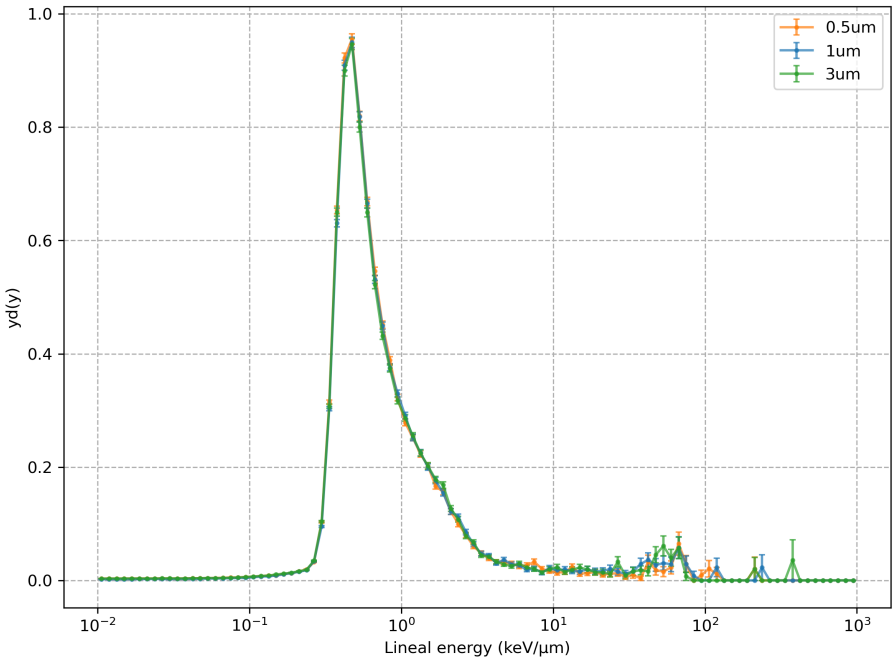

(a) Without tungsten

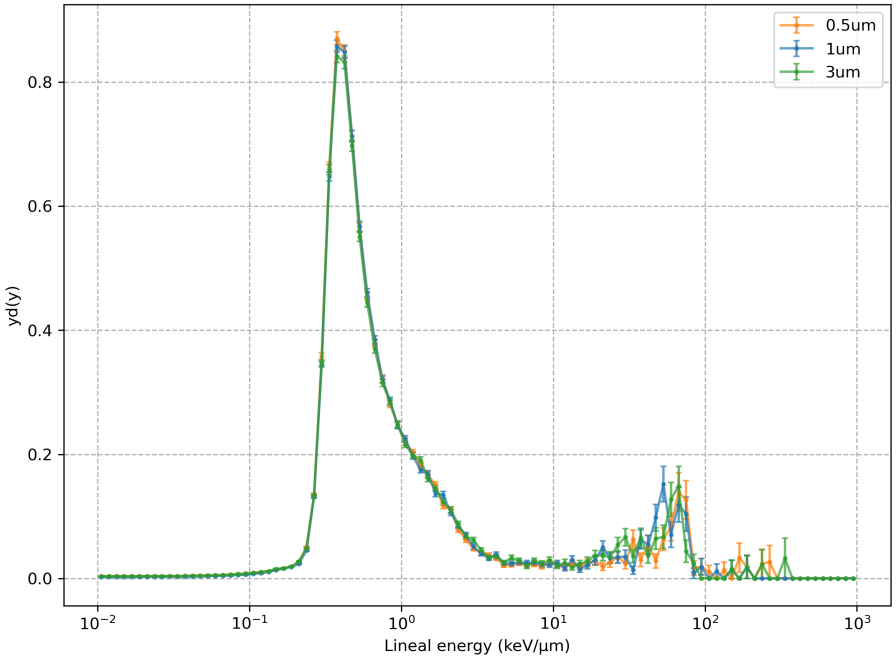

(b) With tungsten

Figure 4.15: Comparison of yd(y) spectra, emphasizing the differences between different films thickness using BERT physics model for a 10×10 cm^2 proton beam.

4.4. Discussion

This chapter examined the optimization of SOI microdosimeter configurations for neutron capture enhanced particle therapy, with the primary objective of detecting and quantifying the biological enhancement provided by ^{10}B neutron capture reactions. These reactions, $^{10}\mathrm{B}(n,\alpha)^{7}\mathrm{Li}$, produce high LET particles (α and ^{7}Li ions) that increase the biological effect of the proton beam. The optimization process focused on five key parameters:

- Detector positioning: placement within the water phantom to maximize thermal neutron fluence at the sensitive volume;
- Proton beam dimensions: field size adjustments to enhance neutron moderation and thermal neutron yield at the region of interest;
- Neutron amplification: incorporation of high Z materials (tungsten spallation target) to boost neutron production;
- Configurations analysis: the enhancement was analyzed by comparing three SOI microdosimeter configurations, standard (boron-free), uniform ^{10}B doping and a $^{10}B_4C$ layer, to assess neutron capture events and microdosimetric response.
- Converter optimization: thickness tuning of the $^{10}B_4C$ layer to balance neutron capture efficiency and reaction product detection.

The collective influence of these parameters on microdosimetric spectra and biological effectiveness was analyzed through Geant4 simulations, with particular emphasis on the dose-mean lineal energy ($\bar{y}_d$) as a critical indicator of the quality of radiation fields.

The choice of detector position is foundational to maximize the amount of thermal neutrons and, consequently, the biological impact of neutron capture reactions. Placing the microdosimeter at the center of the water phantom exploits the region of highest thermal neutron fluence, as the neutron flux distribution peaks there due to the symmetrical geometry and moderation properties of water. This strategic placement ensures that the detector is exposed to the maximum possible number of thermal neutrons generated by proton interactions with oxygen and hydrogen nuclei, which is essential for observing and quantifying the enhancement in microdosimetric spectra attributed to neutron capture events. The simulation results confirm that the central location is optimal for measuring the effects of secondary neutron production and moderation. By introducing a high Z material, such as tungtsen, upstream of the detector, the number of thermal neutrons increase and the position of maximum neutron fluence varies. The tungsten slab acts as an efficient neutron generator via spallation, significantly boosting the overall neutron

yield and shifting the maximum thermal neutron fluence closer to the beam entrance. The presence of tungsten nearly doubles the thermal neutron flux at the detector, as confirmed by both the Bertini and Binary Cascade physics models, though the Bertini model tends to overestimate neutron production.

The dimensions of the incident proton beam play a crucial role in shaping the neutron energy spectrum and the microdosimetric response. Larger beam areas, such as a 10×10 cm^2 field, substantially increase the number of thermal neutrons reaching the detector. This is attributed to the longer moderation paths available for neutrons produced farther from the sensitive volume, allowing a greater fraction to thermalize before interacting with the SOI microdosimeter. The data show that as the beam area increases, there is a marked enhancement in the thermal neutron component at the region of interest, which directly translates to a higher yield of the $^{10}\mathrm{B}(n,\alpha)^{7}\mathrm{Li}$ reaction products. Microdosimetric spectra confirm that larger beam cross sections intensify high lineal energy signatures associated with alpha (85 $keV/\mu m$) and lithium (50 $keV/\mu m$) particles, while concurrently reducing the proton peak intensity and shifting it to higher lineal energies (from 0.35 $keV/\mu m$ to 0.45 $keV/\mu m$). This shift arises because protons traversing the sensitive volume in a larger beam field typically follow longer and more complex trajectories, resulting in lower energy upon arrival and consequently higher energy deposition per unit length. The increased path length, attributable to the beam's large area relative to the sensitive region of the SOI microdosimeter, enhances energy loss through scattering, thereby elevating the lineal energy of proton interactions. The reduction in proton peak intensity stems from the decreased number of protons reaching the sensitive volume.

The inclusion of ^{10}B is central to the NCEPT concept, as the neutron capture reaction $^{10}\mathrm{B}(n,\alpha)^{7}\mathrm{Li}$ produces high LET particles that are highly effective at inducing complex, localized biological damage. The microdosimetric spectra reveal that even in the absence of tungsten, both uniform boron doping in the sensitive volume and the use of a $^{10}B_4C$ converter layer result in a significant increase in the $\bar{y}_d$ compared to standard SOI detector, with enhancements exceeding 50%. This increase in $\bar{y}_d$ directly correlates with a higher relative biological effectiveness, as the high LET component is known to cause more severe DNA damage and cell kill. The presence of tungsten further elevates $\bar{y}_d$ values, underscoring the effect of neutron enhancement and boron capture. The microdosimetric spectra consistently exhibit distinct peaks for α particles and ^{7}Li nuclei, corresponding to the fixed Q values of the $^{10}\mathrm{B}(n,\alpha)^{7}\mathrm{Li}$ reaction. These peak positions remain invariant across all proton beam energies and neutron production mechanisms (with or without tungsten spallation), confirming that the energy deposition of these reaction products is exclusively governed by nuclear properties rather than beam parameters. Consequently,

the amplitude of these peaks serves as a direct quantitative measure of the reaction yield.

The analysis of the $^{10}B_4C$ converter thickness highlights a trade-off between maximizing neutron capture events and ensuring the efficient escape and detection of reaction products. Thicker converters increase the total number of $^{10}\mathrm{B}(n,\alpha)^{7}\mathrm{Li}$ reactions but also enhance the self-absorption of particles within the converter material, thereby reducing the number and average energy of particles that reach the sensitive volumes. Conversely, thinner converters allow a higher fraction of reaction products to escape with greater kinetic energy but reduce the absolute number of neutron capture events. The simulation results indicate that a converter thickness of 1 μm provides an optimal balance, maximizing $\bar{y}_d$ and the detection efficiency for both α and ^{7}Li ions. This finding is consistent with prior studies in Boron neutron capture therapy (BNCT) microdosimetry made by Vohradsky et al.[52], which have demonstrated that thinner boron carbide films enhance the number of sensitive volume crossers.

The choice of physics model for simulating NCEPT microdosimetry, with a focus on neutron generation and moderation, introduces some quantitative differences in the predicted neutron yields and microdosimetric spectra, but the overall trends and conclusions remain robust across models. The Bertini cascade model consistently predicts higher thermal neutron fluence compared to the Binary cascade model, leading to greater microdosimetric enhancement, particularly in configurations with tungsten. This is evident in both the thermal neutron fluence and the amplification of the reaction products. However, while the Bertini model tends to overestimate neutron moderation, the differences in microdosimetric outcomes between the two models are generally within statistical uncertainties for the configurations studied. This consistency, despite quantitative differences, reinforces the reliability of the findings and highlights the importance of experimental benchmarking to further validate the absolute predictions of each physics model.

In summary, the results of this chapter demonstrate that the optimization of microdosimeter configuration for NCEPT requires a holistic approach that considers detector placement, beam size, neutron enhancement strategies and converter design. The positioning of the detector, use of a large area proton beam, addition of a tungsten neutron converter and careful selection of $^{10}B_4C$ film thickness collectively maximize the yield of high LET neutron capture products and the associated biological effect. These findings not only inform the design of future microdosimetric detectors for NCEPT but also provide a framework for translating simulation insights into experimental. The interplay between neutron moderation, capture efficiency and particle transport must be balanced to achieve the desired therapeutic outcomes.

5 | RBE evaluation along the Bragg Peak

Proton beam therapy has become an increasingly important modality in cancer treatment, delivering a concentrated radiation dose to tumors while minimizing exposure to surrounding healthy tissue. A fundamental concept in proton therapy is the RBE, which quantifies the biological impact of protons compared to conventional photon radiation. Clinically, a constant RBE value of 1.1 is applied in treatment planning [28], simplifying the conversion from physical to biological dose. However, this approach overlooks the fact that RBE is not uniform along the proton path. Experimental and preclinical studies have demonstrated that RBE increases significantly near the distal edge of the Bragg peak, where the LET rises sharply [28]. This variation is particularly relevant for tissues located just beyond the tumor, where a higher RBE may lead to an underestimation of biological dose and an increased risk of toxicity.

Additionally, the biological effects are further complicated by the contribution of heavy ion recoils, which are secondary particles produced by nuclear interactions. These recoils can generate localized regions of very high lineal energy, resulting in complex DNA damage and elevating the RBE in these regions [61]. Understanding these events is essential for optimizing treatment plans and ensuring both the safety and efficacy of proton therapy.

This chapter provides a comprehensive analysis of RBE variation along the Bragg peak, with particular attention to the the impact of LET and the role of heavy ion recoils at high lineal energies.

5.1. Setup

In this study, simulations were performed using a monoenergetic proton beam with an energy of 100 MeV, directed into a water phantom to investigate microdosimetric energy deposition along the Bragg peak. The sensitive sites were modeled as small water spheres placed at various depths along the beam axis, with radii of 10, 5, and 1 μm, to enable

the analysis of the energy deposition characteristics at the micron scale and to capture the evolution of deposited energy as the protons slow down and approach the Bragg peak region. The proton beam itself was shaped cylindrically, with a radius chosen to match the maximum range of delta electrons produced by a 100 MeV proton in water, ensuring lateral equilibrium and minimizing edge effects in the sensitive volumes. The maximum kinetic energy that a proton can transfer to a delta electron is given by the formula:

$$E_k^{max} = \frac{4m_e}{m_p} E_p \tag{5.1}$$

where $m_e = 0.511 MeV/c^2$ is the electron mass, $m_p = 938.3 MeV/c^2$ is the proton mass and E_p is the kinetic energy of the proton. For a proton energy of $E_p = 100 MeV$, the calculation yields

$$E_k^{max} = \frac{4 \times 0.511}{938.3} \times 100 \approx 0.218 MeV = 218 keV \tag{5.2}$$

Equation 5.1 is derived from non relativistic conservation of momentum and energy for a head-on collision. To determine the range of a 218 keV electron in water, the NIST ESTAR [62] database provides stopping power and range data for electrons in various materials. According to ESTAR, the continuous slowing down approximation (CSDA) range for electrons with energies near 218 keV in liquid water is approximately 500 μm.

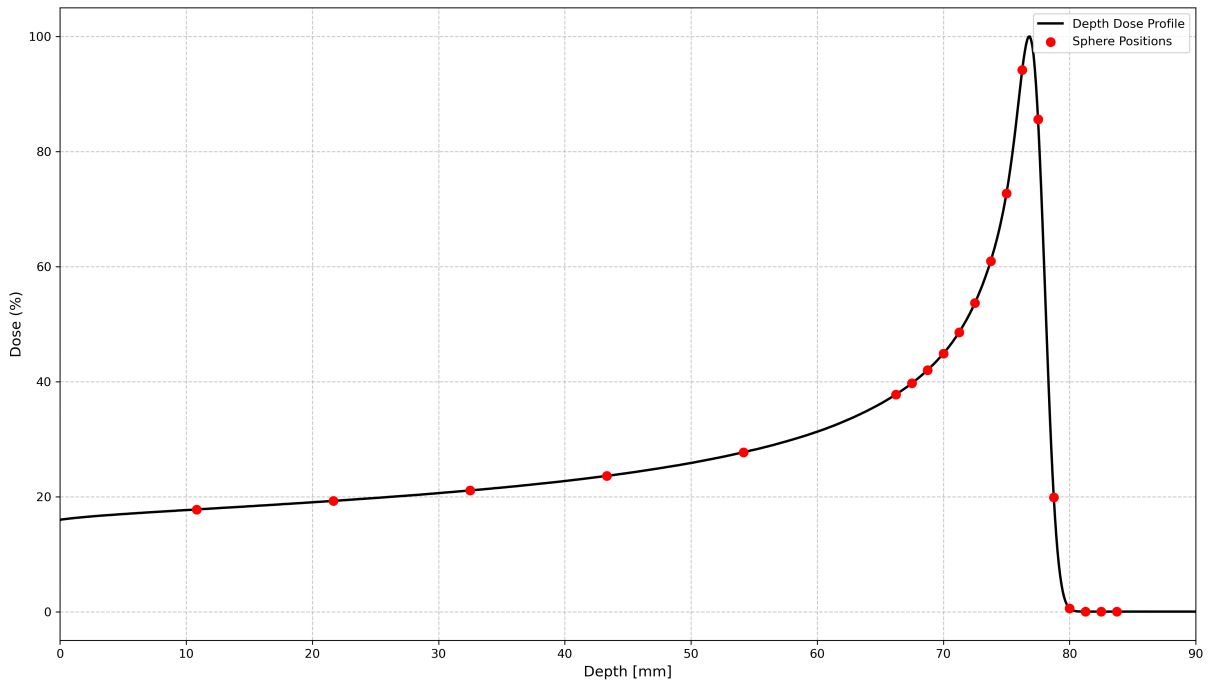

Figure 5.1: Sphere positions superimposed on the depth dose profile.

A total of 20 spheres were placed along the path of the proton beam. The placement strategy prioritizes high resolution sampling in the Bragg peak region, where proton energy deposition exhibits steep gradients. Five spheres are distributed across the 65 mm span from -100 mm to -35 mm, while the remaining fifteen spheres are concentrated within the critical 20 mm interval from -35 mm to -15 mm. This second segment uses a fine spacing to resolve the sharp dose gradients characteristic of the Bragg peak, ensuring accurate capture of rapid dose variations in this significant region. Figure 5.1 illustrates the spatial distribution of the sampling spheres along the beam axis with respect to the Bragg curve. By allocating 75% of the spheres to the Bragg peak zone, the spatial resolution is maximized where energy deposition changes most rapidly.

To enhance resolution at the distal edge of the Bragg peak, a high density sphere configuration was implemented. Eleven spheres were distributed across the 70–80 mm region with 1 mm spacing, providing baseline coverage of the proximal Bragg region. Within the critical 79–80 mm zone, four additional spheres were positioned at 0.2 mm intervals to achieve sub-millimeter resolution for characterizing the steep dose gradient. Figure 5.2 illustrates this optimized sampling configuration.

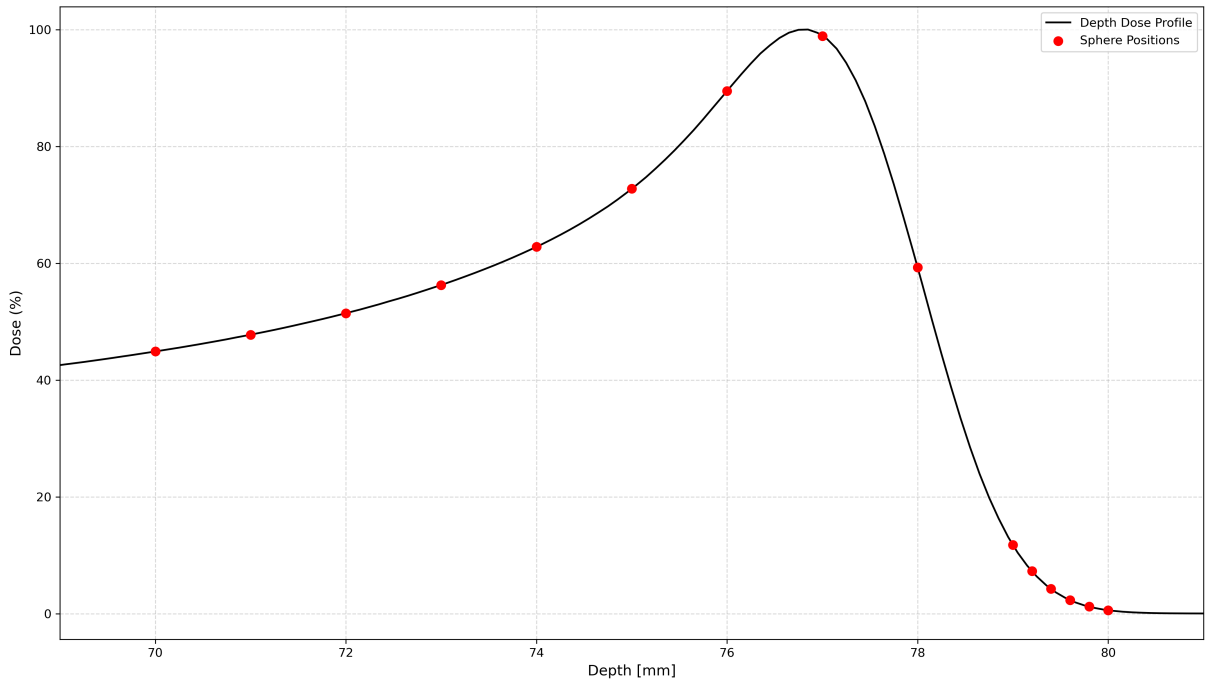

Figure 5.2: Sphere positions with high density configuration in the distal region superimposed on the depth dose profile.

To accurately model electromagnetic interactions, two advanced low energy physics models available in Geant4, Livermore and Penelope, were employed. These models differ

in their treatment of low energy photon and electron transport, which can significantly influence the generation and propagation of secondary electrons, especially at energies below 1 keV. The Penelope model is known to produce a greater number of low energy secondary electrons, particularly in the 250 eV to 1 keV range, compared to Livermore, but both models yield comparable results for macroscopic dose distributions [63]. The simulation geometry around each sensitive sphere was divided into concentric regions, with progressively reduced range cuts in regions closer to the scoring volumes. This approach allowed the capture of all relevant low energy interactions near the sensitive sites while optimizing computational efficiency in less critical outer regions, as recommended for complex geometries in Geant4 [64].

This simulation framework, combining micrometer scale scoring, beam shaping and adaptive region based range cuts, provides a robust basis for analyzing the microdosimetric properties of proton beams and for comparing the impact of different electromagnetic physics models on the resulting energy deposition patterns.

5.2. Microdosimetric results

The analysis reveals the microdosimetric behavior along the proton beam path. The $\bar{y}_d$ for each sphere size demonstrate the expected correlation with linear energy transfer, showing characteristic increases beyond the Bragg peak region as illustrated in Figure 5.3. However, spheres 4 and 8 exhibit anomalously elevated $\bar{y}_d$ values that exceed theoretical predictions for their respective positions along the beam path. These unexpectedly high $\bar{y}_d$ values result from heavy ion recoil events that deposit substantial energy within the detector volumes. During proton interactions with target nuclei, nuclear reactions produce recoiling fragments with short ranges but high energy deposition rates. The microdosimetric spectra (Figure 5.4) for spheres 4 and 8 clearly demonstrate how these high lineal energy events dominate the dose weighted distributions. These rare nuclear interaction events create localized energy depositions that can exceed 500 $keV/\,um$, significantly influencing the calculated $\bar{y}_d$ values.

The large error bars associated with spheres 4 and 8 reflect the statistical uncertainty arising from rare, high energy deposition events. When microdosimetric measurements are dominated by single high-LET events, the statistical uncertainty becomes larger due to the limited sampling of these infrequent occurrences. The stochastic nature of nuclear reactions means that such events occur randomly and infrequently, contributing to the observed statistical variations in the measurements.

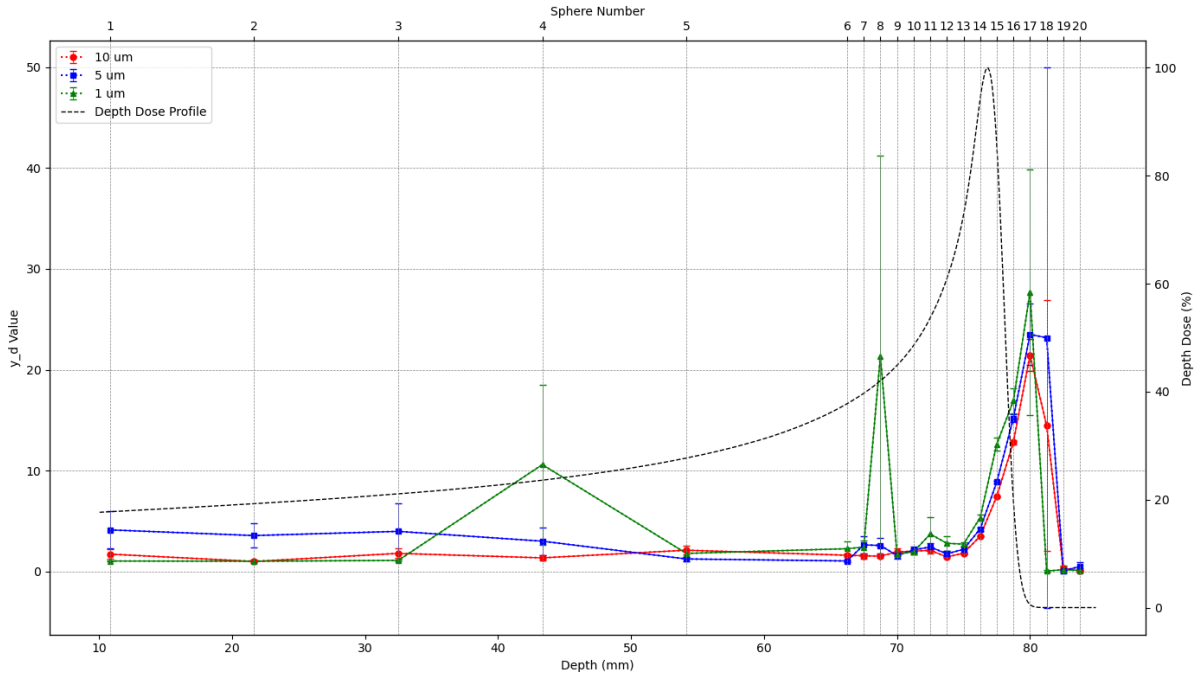

Figure 5.3: $\bar{y}_d$ values for spheres of varying sizes positioned along a 100 MeV proton beam path, with corresponding depth dose profile using Livermore.

The pronounced effect observed in the smallest spheres (1 μm radius) can be attributed to the inverse relationship between sphere size and mean chord length. The lineal energy is defined as $y = \epsilon/\langle l \rangle$, where ϵ is the energy imparted and $\langle l \rangle$ is the mean chord length. For spherical geometries, the mean chord length is given by $\langle l \rangle = 2d/3$ for isotropic radiation, where d is the sphere diameter. The smaller mean chord length in 1 μm spheres results in higher lineal energy values for equivalent energy depositions compared to larger spheres, which exhibit lower $\bar{y}_d$ values due to volume averaging effects that dilute the contribution of localized high energy events across larger detector volumes.

Examination of Figure 5.3 reveals important characteristics. In the entrance region, the $\bar{y}_d$ values demonstrate consistency across all sphere geometries, with the exception of the 5 μm radius spheres at shallow depths. The values observed for these spheres can be attributed to the same stochastic high lineal energy events discussed previously, as evidenced by the correspondingly larger error bars that reflect the statistical uncertainty associated with rare, high energy deposition events. The most significant sphere size dependency emerges in the distal portion of the Bragg peak region, where a clear inverse relationship between sphere diameter and $\bar{y}_d$ values becomes apparent. This variation reflects differences in particle interaction geometry as protons approach their range limit. In this terminal region, the probability of proton stopping events within the detector

volume increases due to the reduction in particle energy.

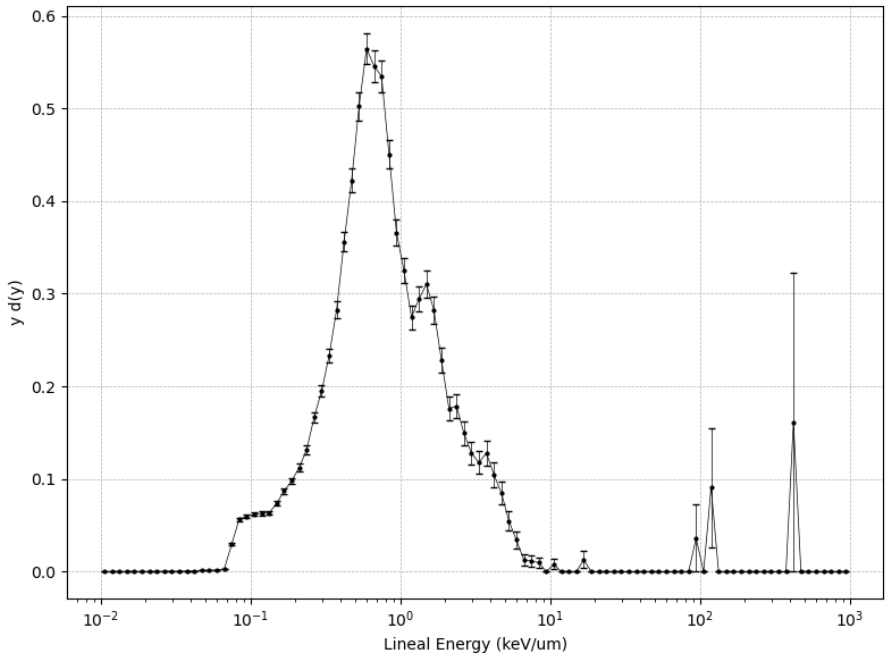

(a) Sphere number 4

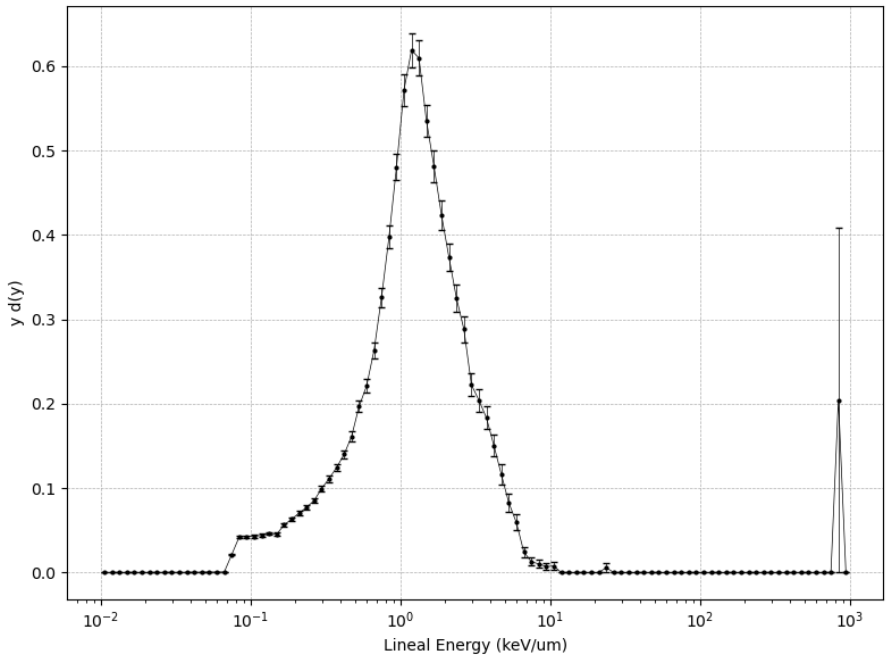

(b) Sphere number 8

Figure 5.4: Microdosimetric spectra for water spheres of 1 μm radius

When a proton terminates within a spherical detector, the conventional microdosimetric formulation encounters a geometric inconsistency. The lineal energy calculation assumes

that particles traverse the entire sensitive volume. However, when particles stop within the volume, their actual path length becomes shorter than the assumed mean chord length, resulting in reduced lineal energy values. This effect becomes more pronounced in larger spheres, where the stopping probability is higher due to the increased geometric cross section. The 1 μm spheres exhibit the highest $\bar{y}_d$ values in the Bragg peak region because their small dimensions minimize the probability of stopping events. Consequently, the majority of energy deposition events in these small volumes correspond to traversal events, where the mean chord length represents the particle path geometry. This geometric consideration becomes critical for accurate microdosimetric interpretation, as only crossing events provide meaningful lineal energy measurements that properly reflect the linear energy transfer characteristics of the radiation field.

The analysis of stopping energy fractions presented in Figure 5.5 demonstrates the influence of detector geometry on proton stopping events along the beam path. The data reveals that the fraction of energy deposited by stopping protons remains negligible across all sphere sizes at shallow depths, with values close to 0% up to the Bragg peak position. This observation confirms that the majority of energy deposition in these regions results from protons traversing the detector volumes rather than terminating within them. The most striking differences between sphere sizes emerge in the distal region beyond the Bragg peak, where the stopping energy fraction increases dramatically. The larger spheres exhibit stopping energy percentages reaching approximately 12% of the total deposited energy. In contrast, the smallest 1 μm spheres demonstrate a different behavior, with stopping energy fractions peaking at only 1-2% even at the most distal positions.

This size-dependent variation in stopping energy fraction provides quantitative validation for the previously observed differences in lineal energy values. The stopping energy contributions in larger spheres explain the reduced $\bar{y}_d$ values observed in these detectors within the Bragg peak region. When protons terminate within the detector volume, the effective path length becomes shorter than the assumed mean chord length, reducing the calculated lineal energy despite the high energy deposition. Conversely, the minimal stopping energy fraction in 1 μm spheres confirms that these detectors primarily register crossing events, yielding more accurate lineal energy measurements that reflect the radiation quality characteristics. The correlation between stopping energy fraction and detector size demonstrates the fundamental geometric constraint that governs microdosimetric measurements in high LET regions. The results confirm that the size of the microdosimeter directly impacts measurement accuracy. This highlights the need to choose an appropriate detector volume, especially in the Bragg peak region, where variations in proton stopping positions become important and can skew measurements.

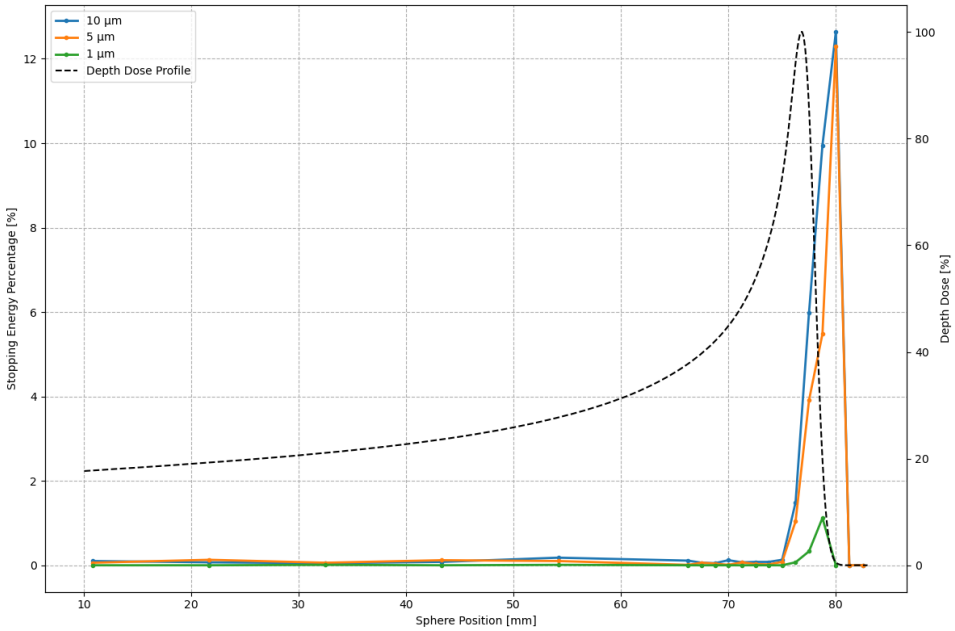

Figure 5.5: Stopping energy percentage as a function of depth for 10 μm, 5 μm, and 1 μm spheres, showing a sharp increase near the Bragg peak, especially for larger spheres.

The distinction between crossing and stopping events represents a fundamental consideration in microdosimetric analysis, particularly in regions of high stopping power such as the Bragg peak. Accurate $\bar{y}_d$ determinations require careful discrimination between these event types, with emphasis placed on crossing events where the geometric assumptions underlying the lineal energy calculation remain valid. This consideration motivates the focused analysis of the Bragg peak region using the high density sphere configuration.

The $\bar{y}_d$ values in the Bragg peak region, presented in Figure 5.6, reveal a pronounced and rapid increase occurring only after the Bragg peak, specifically between 1 and 2 mm beyond the maximum dose. This behaviour highlights the significant rise in linear energy deposition in the distal edge of the Bragg peak, where the proton fluence drops sharply and the contribution from high LET particles becomes dominant. The uncertainties in this region are large, primarily due to the limited number of traversing particles and the effect of rare, high LET events on the mean value.

In Figure 5.7, the microdosimetric spectra are shown for all spheres in the high density configuration. As the depth increases, the main proton peak in each spectrum shifts towards higher lineal energy values, reflecting the continuous energy loss and increasing LET of protons as they approach the end of their range. This shift is a direct consequence of the decreasing proton energy and the associated increase in stopping power. Additionally, heavy ion recoils are still present at these depths, further broadening the spectra

and contributing to the overall uncertainties, especially in the distal region where their relative influence is enhanced.

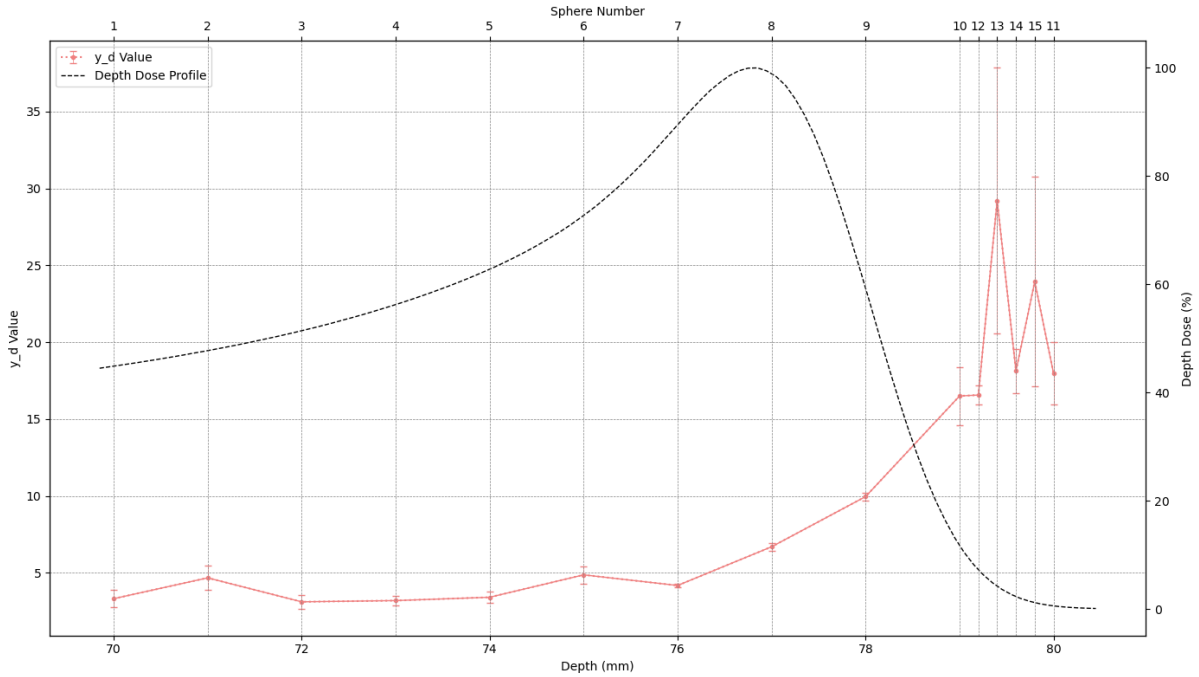

Figure 5.6: $\bar{y}_d$ values for spheres of 1 μm radius positioned at the Bragg peak of a 100 MeV proton beam, with corresponding depth dose profile using Livermore.

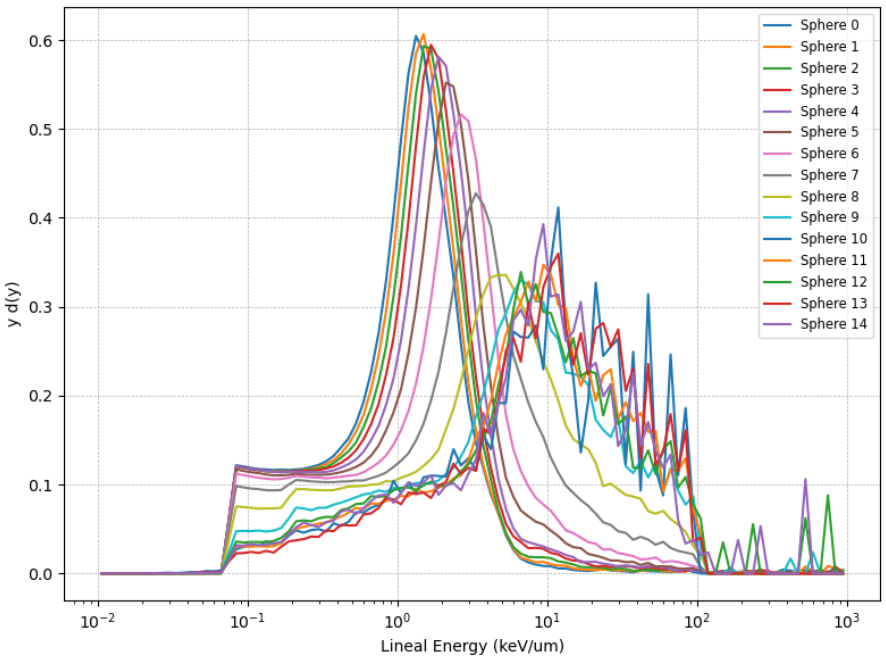

Figure 5.7: yd(y) distributions for 15 spheres in the Bragg peak region.

5.3. RBE analysis

In this section, the evaluation of RBE is carried out using different models, with particular attention given to the comparison between the MKM and biological weighting function models. As previously discussed, the MKM model exhibits direct dependence on the $\bar{y}_d$, rendering it more sensitive than the BWF models to the presence of heavy ion recoils and high LET particles, particularly in the shallow depths before the Bragg peak. This sensitivity often leads to RBE overestimation in areas where rare, high LET events dominate the microdosimetric spectra and statistical uncertainties become significant. To address this limitation, the modified version of the MKM model developed by Kase et al. [29] has been employed in this work, incorporating corrections that mitigate the influence of these extreme events through the introduction of a saturation parameter. The subsequent analysis compares the predictions of the modified MKM and the BWF models, highlighting their respective responses to variations in radiation quality and the implications for accurate RBE estimation in proton therapy.

The comparison was conducted using the V79 cell line with numerical values of the MKM and modified MKM parameters as previously determined by Sato et al. [65]: $\alpha_0 = 0.105$ Gy^{-1}, $\alpha_{ref} = 0.184$ Gy^{-1}, $\beta_{ref} = 0.02$ Gy^{-2}, $r_d = 0.232$ μm, and $y_0 = 133.1$ $keV/\mu m$.

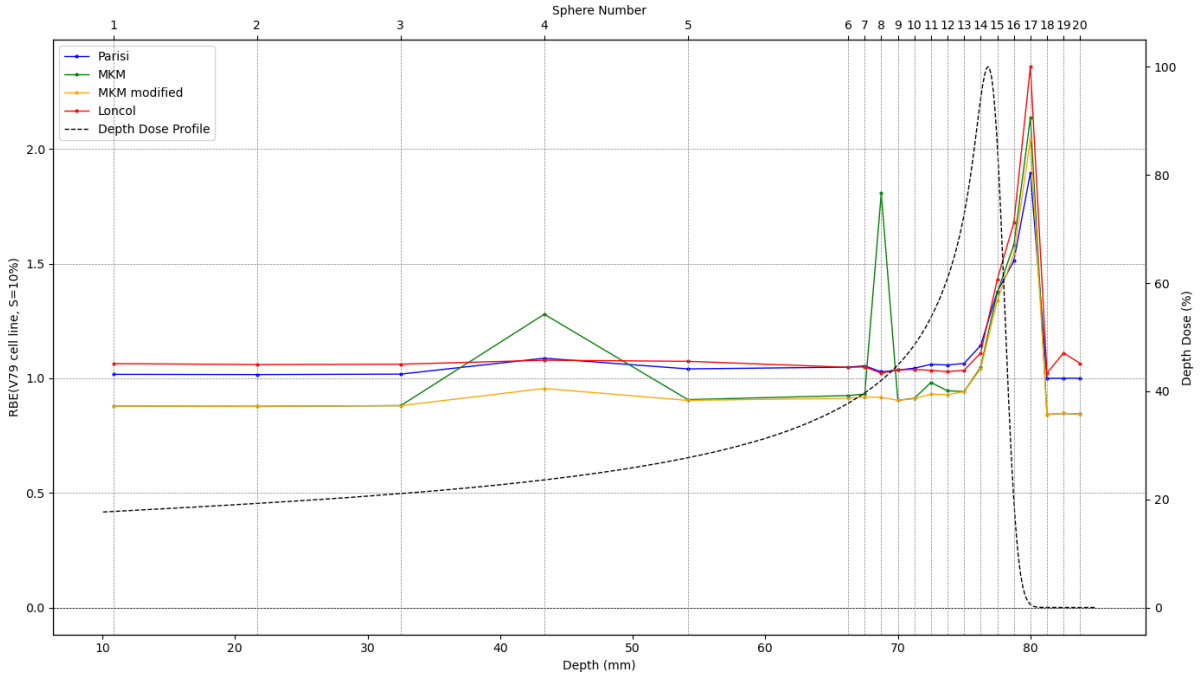

Figure 5.8: Depth-dependent RBE_{10} values for V79 cells calculated using different models with 1 μm radius spheres.

Figure 5.8 presents the RBE values for V79 cells along the proton beam path, comparing the predictions of the Parisi, MKM, modified MKM and Loncol models. Both the standard and modified MKM models predict RBE values below unity in the entrance regions, indicating that protons could be less biologically effective than photons at shallow depths. This behavior is consistent with the range reported by Paganetti [28], who found RBE values as low as 0.7 in some experimental conditions. In contrast, the Parisi IBWF and Loncol models maintain RBE values at or above unity throughout the beam path. Within the Bragg peak region, all models demonstrate convergence to similar RBE values, indicating agreement in the high LET regime where biological enhancement is most pronounced. The Loncol model exhibits slightly elevated RBE values beyond the Bragg peak, corresponding to the region of highest $\bar{y}_d$ values as observed in Figure 5.3. The comparison between the original and modified MKM models reveals the effectiveness of the saturation correction, particularly evident at measurement positions where anomalously high LET events were recorded (such as spheres 4 and 8). The modified MKM model demonstrates reduced sensitivity to these statistical outliers, producing RBE values more consistent with neighboring measurement positions where such extreme events were absent, thereby providing a more stable RBE assessment.

The most critical conclusion is that the RBE of proton beams exhibits significant variability along the beam path, despite the clinical use of spread out Bragg peaks (SOBPs) rather than monoenergetic beams. Crucially, the RBE demonstrates a pronounced exponential increase at the distal edge of the Bragg peak, reaching values as high as 2.0-2.5 in this simulation work. This elevated RBE persists within a narrow region extending 2–3 mm beyond the physical Bragg peak, effectively creating a biological hot zone that extends the biologically effective range beyond what is predicted by physical dose calculations alone. Consequently, treatment planning must account for this distal enhancement, as critical structures immediately beyond the target volume may experience higher biological damage than indicated by physical dose distributions. The necessity of integrating variable RBE modeling into proton therapy planning is underscored by the evidence that RBE is not constant along the proton path, particularly near and just beyond the Bragg peak. As highlighted in recent research and clinical surveys, there is growing recognition that adopting variable RBE models, rather than a constant value, can improve the accuracy of treatment planning and better protect healthy tissues, especially in anatomically sensitive regions where end of range effects are most pronounced [66].

5.4. Physics comparison

This section presents an analysis comparing the electromagnetic physics models Livermore and Penelope. Both models were implemented with identical cut range parameters of 250 nm applied within the spherical SVs to ensure consistent computational frameworks for comparison. The results demonstrate consistency between the Livermore and Penelope models. As demonstrated in Figure 5.9, the primary source of divergence stems from heavy ion recoil events, which significantly influence the $\bar{y}_d$ calculations. These rare, high LET interactions introduce statistical fluctuations, particularly in the distal portion of the Bragg peak where scoring events decrease. The increased statistical uncertainties associated with these heavy ion recoil events create differences between the models that are more pronounced due to the error bars rather than fundamental physics differences.

The direct relationship between the RBE calculated via the MKM model and $\bar{y}_d$ means that any observed discrepancies in microdosimetric quantities propagate consistently to RBE evaluations. Consequently, the differences shown in Figure 5.9 would manifest similarly in RBE calculations using the MKM model. When excluding these infrequent high LET occurrences, both models yield concordant results, indicating their functional equivalence for microdosimetric applications. Studies have documented that differences between Livermore and Penelope models are generally below 2% for most applications [63].

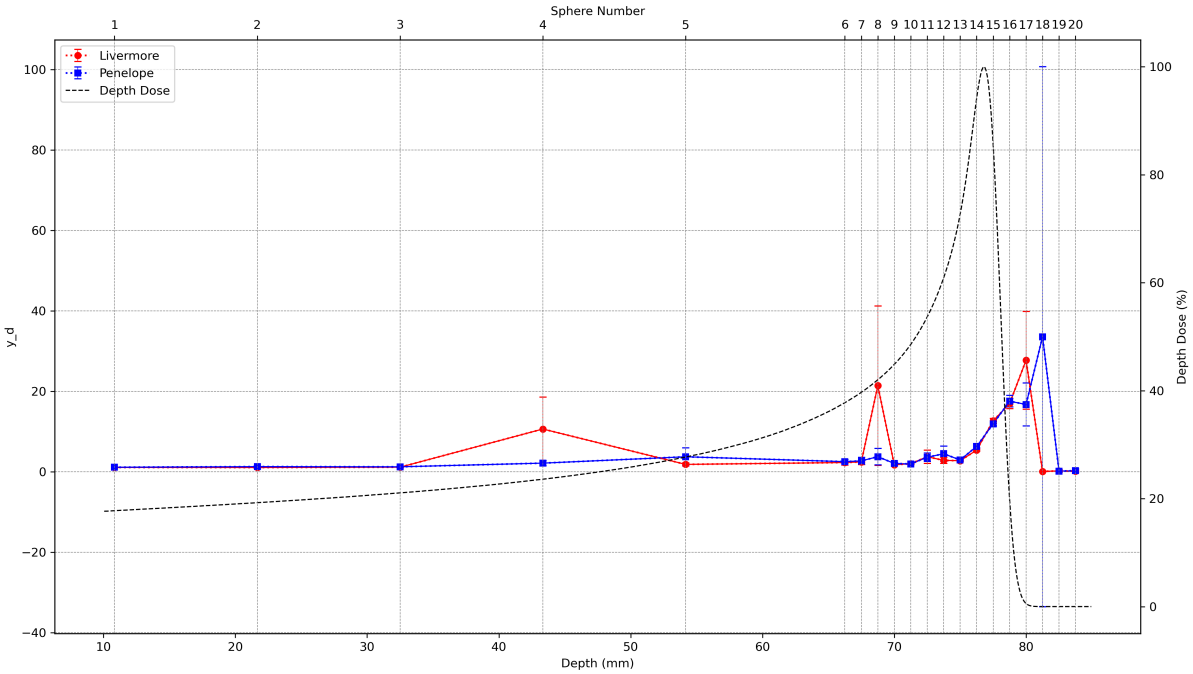

Figure 5.9: Comparison of $\bar{y}_d$ values as a function of depth for Livermore and Penelope, overlaid with the normalized depth dose profile for a 1 μm radius geometry.

Further analysis of RBE using the Loncol model is illustrated in Figure 5.10. Throughout the proximal regions of the Bragg peak, both electromagnetic models produce statistically indistinguishable RBE values, confirming their equivalence. However, in the distal portion of the Bragg peak, apparent differences emerge that are attributable to limited sampling statistics rather than fundamental physics differences. Monte Carlo studies have shown that the distal region is particularly sensitive to statistical uncertainties due to the reduced number of primary particles and secondary interactions in this region [67]. The statistical nature of these differences is evidenced by the fact that they cannot be directly associated with physics model differences but rather reflect the limitations of Monte Carlo sampling in regions of low event density.

The convergence of results across both $\bar{y}_d$ and RBE metrics validates that neither electromagnetic model introduces systematic bias, provided that statistical uncertainties are accounted for in regions of low event density. The practical implications of these findings confirm that both the Livermore and Penelope electromagnetic models provide equivalent reliability for microdosimetric studies when statistical uncertainties are carefully considered. The choice between models can be guided by specific requirements, with both offering robust results. The observed equivalence in both microdosimetric quantities and RBE calculations underscores the reliability of either model.

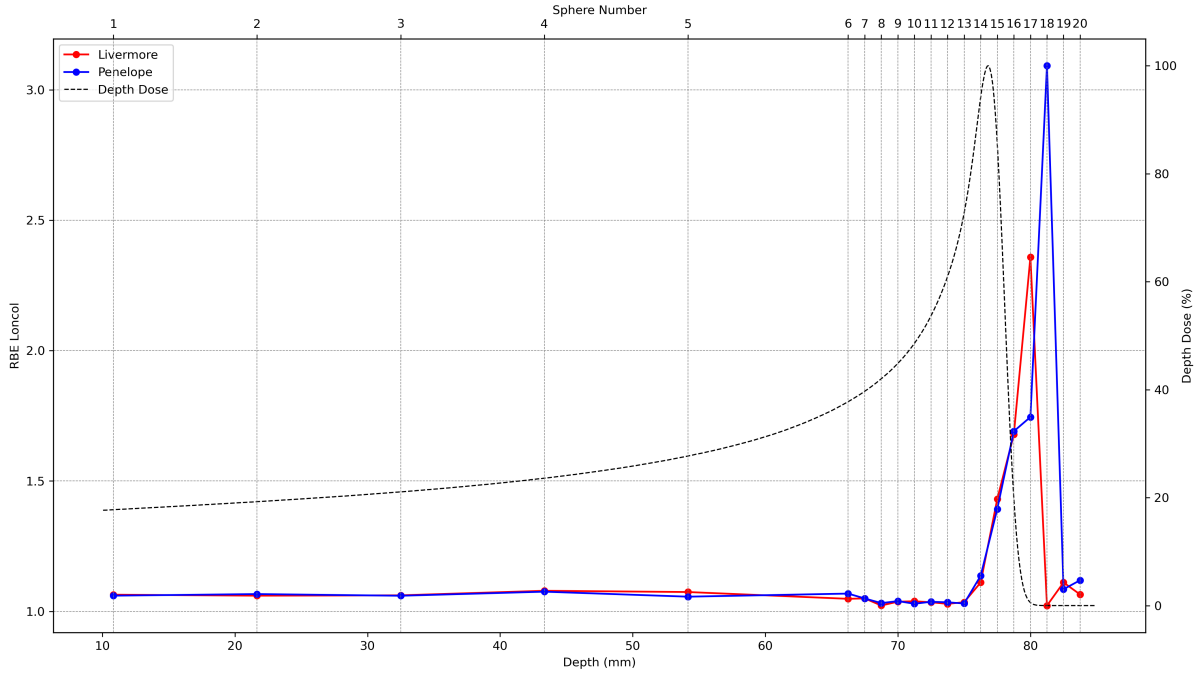

Figure 5.10: RBE evaluated with Loncol model as a function of depth for Livermore and Penelope, overlaid with the normalized depth dose profile for a 1 μm radius geometry.

5.5. Discussion

This chapter centers on the microdosimetric evaluation of RBE along the Bragg peak in proton therapy. It focuses on both the physical and biological complexities that arise near the end of the proton range. The findings reinforce that the widely used clinical assumption of a constant RBE value of 1.1 is a simplification that does not reflect the true variability of biological effectiveness along the proton path. Simulation data show that RBE increases sharply at the distal edge of the Bragg peak, coinciding with a rise in LET. This increase is especially significant for tissues just beyond the tumor, where a higher RBE could lead to underestimation of biological dose and a risk of secondary tumor if not properly accounted for in treatment planning. The analysis highlights the important role of heavy ion recoils, which are generated by nuclear interactions and can deposit large amounts of energy in small volumes. These rare but impactful events cause localized spikes in energy deposited, resulting in complex DNA damage and elevating RBE. The microdosimetric spectra reveal that such events, while infrequent, can dominate the $\bar{y}_d$ calculations and introduce substantial statistical uncertainty, particularly in smaller detector volumes where single high LET events have a proportionally greater effect.

The positioning of the scoring spheres in this study was a critical choice, designed to maximize the accuracy of the microdosimetric analysis. By concentrating the majority of spheres in the Bragg peak and distal edge regions, where the proton LET changes most rapidly, the setup ensured high spatial resolution where the biological and physical gradients are steepest. This dense sampling allowed for the characterization of sharp LET variations, which are essential for understanding the evolution of RBE and the impact of rare, high LET events. The advantage of this approach lies in its ability to resolve significant changes in energy deposition that would be missed with coarser sampling, providing a more accurate basis for interpreting microdosimetric spectra.

The distinction between stopping and crossing events emerges as a fundamental consideration for accurate microdosimetric analysis. The lineal energy calculation assumes particles traverse the entire sensitive volume, but when protons stop within the detector, the actual path length is shorter than the mean chord length used in the calculation, leading to artificially reduced lineal energy values. This effect is observed in larger spheres, where the geometric cross section increases the likelihood of stopping events. The analysis of stopping energy fractions confirms that larger spheres register a significant proportion of energy from stopping protons in the distal Bragg peak region, while the smallest spheres maintain a minimal stopping fraction even at these depths. This behavior validates the use of small sensitive volumes for capturing the true traversal events that best represent

the radiation field's quality, particularly in high LET regions where accurate characterization is most critical. The investigation of crossing versus stopping events is not only a technical nuance but a fundamental aspect of microdosimetry.

Turning to the RBE analysis, the results demonstrates that the biological effectiveness of proton beams is not constant along the beam path. All evaluated models, including the MKM, its modified version and empirical biological weighting function approaches, reveal a pronounced increase in RBE at the distal edge of the Bragg peak, with values reaching as high as 2.0–2.5 within a narrow region just beyond the maximum physical dose. This creates a biological "hot zone" that extends the effective range of the beam beyond what is predicted by the physical dose profile. The modified MKM, with its saturation correction, demonstrates improved stability by reducing the influence of rare, high LET outliers, while the BWF models provide an empirical framework that aligns with the MKM in high LET regions. The convergence of these models in the Bragg peak region lends confidence to their use, but their divergence elsewhere highlights the need for validation and further experimental data.

The comparison between different electromagnetic physics models, Livermore and Penelope, shows that both yield consistent microdosimetric and RBE results. The observed differences can be attributed primarily to statistical fluctuations from rare heavy ion recoil events rather than fundamental differences in physical modeling. This finding supports the reliability of both models for detailed microdosimetric studies, provided that statistical uncertainties are properly managed.

Overall, the chapter demonstrates that RBE is not constant along the proton beam path but exhibits variations at the distal edge of the Bragg peak. The presence of a biological "hot zone" beyond the physical dose maximum has implications for treatment planning and patient safety. Integrating variable RBE models is essential for accurately assessing biological dose distributions and minimizing the risk to healthy tissues adjacent to the target. The results also highlight the need for experimental validation to refine microdosimetric models and reduce uncertainties in the distal region of the Bragg peak.

Conclusions and future developments

This thesis has explored the microdosimetric characterization of proton therapy modalities, focusing on both the enhancement of dose via neutron capture (NCEPT) and the evaluation of RBE along the proton Bragg peak. The work combines Monte Carlo simulations with detector modeling, aiming to bridge the gap between physical dose distributions and biological impact at the microscopic scale. The microdosimetric approach is essential for quantifying the stochastic nature of energy deposition in volumes of cell size, providing a more accurate understanding of radiation quality compared to conventional macroscopic metrics. Simulating microdosimetric spectra has made it possible to identify and quantify the contributions of high LET components originating from both secondary particles and nuclear reactions within the radiation field. This characterization is crucial, as it enables a direct connection between the physical quality of the radiation and its biological impact. By applying radiobiological models to the microdosimetric data, these high LET contributions can be related to specific biological endpoints. Thereby they can provide a more comprehensive understanding of how microscopic patterns of energy deposition influence cellular response and treatment effectiveness.

In the context of NCEPT, the results confirm that the presence of ^{10}B, whether uniformly distributed within the sensitive volume or introduced via a $^{10}B_4C$ converter, leads to a significant enhancement of dose through the ^{10}B(n,α)^{7}Li reaction. This effect is maximized with larger beam cross sections, which increase the thermal neutron flux at the detector. Both the uniform ^{10}B and $^{10}B_4C$ converter configurations produce clear microdosimetric signatures and an increase in dose-mean lineal energy, indicating a potential for complex DNA damage. The principal advantage of this technique is its potential to confine the additional high LET dose to the tumor region, provided that ^{10}B accumulates selectively within malignant tissue. Clinically, the effectiveness and safety of NCEPT depend on the ability to achieve a specific uptake of ^{10}B in the tumor, as any significant presence of the capture agent in healthy tissues would result in unwanted dose enhancement and increased risk of toxicity. Therefore, the therapeutic benefit of NCEPT is linked to the precision of boron delivery and any off target accumulation could compromise the selectivity of the treatment.

In this work, the introduction of a tungsten slab upstream of the target was used as a tool to artificially enhance the production of thermal neutrons and thereby amplify the contribution of neutron capture events. This approach proved effective in simulation, as it significantly increased the neutron flux and the resulting dose enhancement. It made possible to observe and analyze the impact of neutron capture on the detector response and to optimize the SOI microdosimeter configurations. However, it is important to emphasize that such a strategy is not feasible in a clinical environment, as the presence of tungsten also leads to a rise in unwanted neutron dose to healthy tissues, potentially doubling the neutron background and increasing the risk of late effects such as secondary tumors. This is concerning for fast neutrons produced via spallation, which have long ranges and can deposit dose far from the tumor site. The analysis presented here demonstrates that, while the addition of tungsten serves as a useful investigative tool for studying the effects of neutron capture in a controlled simulation and experimental setting, any clinical implementation of NCEPT must balance the goal of tumor dose amplification against the imperative to avoid introducing additional risks to normal tissues.

The second major focus of this thesis has been the analysis of RBE variations along the proton Bragg peak. Simulations using water microdosimetric spheres of varying sizes demonstrated that the dose-mean lineal energy increases sharply in the distal region of the Bragg peak, as expected due to the higher LET and low energy protons. This evolution in microdosimetric spectra reflects the changing composition of the radiation field. Application of radiobiological models, including the MKM and Loncol's model, to these spectra yielded RBE profiles that are depth dependent. These profiles show RBE peaking just beyond the Bragg peak and decreasing in the entrance regions, aligning with established physical principles. These results underscore the inadequacy of a constant clinical RBE equal to 1.1 for protons, particularly as it fails to capture the elevated RBE in the distal edge where biological effectiveness is maximized. This discrepancy poses a clinical risk: if critical organs lie immediately beyond the target volume, the underprediction of biological dose in the distal region could lead to unexpected toxicity. While this analysis used monoenergetic beams for fundamental characterization, future work must extend these microdosimetry RBE models to clinical SOBP beams at proton therapy facilities. Validation of these models is crucial because it would allow to incorporate depth-dependent RBE values into clinical treatment planning software. This integration ensures that the biological dose is optimized based on how radiation quality changes along the path of the proton beam.

Experimental validation is important for establishing the reliability of simulation results. For NCEPT, benchmarking against measured microdosimetric spectra and neutron fluxes,

obtained using SOI microdosimeters and neutron detectors in clinical proton therapy environments, is essential to verify the accuracy of simulated thermal neutron yields and dose-mean lineal energy enhancements. This validation ensures that Geant4 predictions of neutron capture events and their spatial distribution align with experimental observations. This would confirm the feasibility of tumor dose amplification while minimizing secondary neutron risks. Similarly, for RBE evaluation along the Bragg peak, experimental validation of microdosimetric spectra is critical to verify simulated $\bar{y}_d$ evolution and spectral shifts at distal edges. Matching measured $\bar{y}_d$ and RBE values against experimental data would confirm the inadequacy of a constant RBE and underscores the necessity of variable RBE integration into treatment planning systems for accurate biological dose optimization. Without such benchmarking, clinical translation of RBE models driven by microdosimetry risks misrepresenting the RBE in critical regions.

Looking forward, further work should include the optimization of detector configurations for both neutron sensitivity and microdosimetric resolution; the modeling of secondary cancer risks from fast neutrons using microdosimetric spectra; the integration of RBE values based on microdosimetry and varying along the beam path into clinical treatment planning systems. Additionally, alternative strategies for enhancing thermal neutron flux should be explored to avoid excessive neutron production in healthy tissues. The ultimate goal is to translate the insights gained from microdosimetry into safer and more effective proton therapy, maximizing tumor control while minimizing risks to healthy tissues.

In summary, this work demonstrates the power of microdosimetry for both fundamental understanding and practical optimization of proton therapy techniques. The results highlight the promise of NCEPT for localized dose enhancement, while also cautioning against approaches that may introduce risks to healthy tissue. The rigorous evaluation of RBE along the Bragg peak further supports the move toward biologically optimized, patient specific treatment planning in hadron therapy.

Bibliography

[1] Mitra Safavi-Naeini, Andrew Chacon, Susanna Guatelli, Daniel R. Franklin, Keith Bambery, Marie Claude Gregoire, and Anatoly Rosenfeld. Opportunistic dose amplification for proton and carbon ion therapy via capture of internally generated thermal neutrons. *Scientific Reports*, 8, 12 2018.

[2] Nicholas Howell, Ryan J. Middleton, Frederic Sierro, Benjamin H. Fraser, Naomi A. Wyatt, Andrew Chacon, Keith R. Bambery, Elle Livio, Christopher Dobie, Joseph J. Bevitt, Justin Davies, Anthony Dosseto, Daniel R. Franklin, Ulf Garbe, Susanna Guatelli, Ryoichi Hirayama, Naruhiro Matsufuji, Akram Mohammadi, Karl Mutimer, Louis M. Rendina, Anatoly B. Rosenfeld, and Mitra Safavi-Naeini. Neutron capture enhances dose and reduces cancer cell viability in and out of beam during helium and carbon ion therapy. *International Journal of Radiation Oncology Biology Physics*, 120:229–242, 9 2024.

[3] Wayne D. Newhauser and Rui Zhang. The physics of proton therapy, 4 2015.

[4] D.. Filges and Frank. Goldenbaum. *Handbook of spallation research : theory, experiments and applications*. Wiley-VCH, 2009.

[5] Jemila Habainy, Yongjoong Lee, Yong Dai, and Srinivasan Iyengar. Tungsten as spallation material at the european spallation source. In *Proceedings of the 14th International Workshop on Spallation Materials Technology*. Journal of the Physical Society of Japan, 2 2020.

[6] Jaegwon Yoo. Neutron production from spallation reactions. Technical report, 1998.

[7] Glenn F Knoll. *Radiation detection and measurement*. John Wiley & Sons, 2010.

[8] Robert R Wilson. Radiological use of fast protons. Technical report.

[9] Eric Ojerholm and Justin E. Bekelman. Finding value for protons: The case of prostate cancer?, 4 2018.

[10] Jerry D Slater. Clinical applications of proton radiation treatment at loma linda

university: review of a fifteen-year experience. *Technology in cancer research & treatment*, 5(2):81–89, 2006.

[11] AM Koehler, RJ Schneider, and JM Sisterson. Range modulators for protons and heavy ions. *Nuclear Instruments and Methods*, 131(3):437–440, 1975.

[12] Harald Paganetti. *Proton Therapy Physics*, volume 20115763. CRC Press, 12 2011.

[13] Antony Lomax. Intensity modulation methods for proton radiotherapy. *Physics in Medicine & Biology*, 44(1):185, 1999.

[14] D. J. Thomas. Icru report 85: fundamental quantities and units for ionizing radiation. *Radiation Protection Dosimetry*, 150:550–552, 7 2012.

[15] Dieter Schardt, Thilo Elsässer, and Daniela Schulz-Ertner. Heavy-ion tumor therapy: Physical and radiobiological benefits, 2 2010.

[16] F. Bloch. Zur bremsung rasch bewegter teilchen beim durchgang durch materie. *Annalen der Physik*, 408:285–320, 1 1933.

[17] Douglas Hanahan and Robert A. Weinberg. Hallmarks of cancer: The next generation, 3 2011.

[18] Y Furusawa, K Fukutsu, M Aoki, H Itsukaichi, K Eguchi-Kasai, H Ohara, F Yatagai, T Kanai, and K Ando. Inactivation of aerobic and hypoxic cells from three different cell lines by accelerated $^{3}He-$, $^{12}C-$ and $^{20}Ne-Ion$ beams. Technical report, 2000.

[19] Kuan Hu, Zhimin Yang, Lingling Zhang, Lin Xie, Lu Wang, Hao Xu, Lee Josephson, Steven H. Liang, and Ming Rong Zhang. Boron agents for neutron capture therapy, 2 2020.

[20] Wolfgang A. G. Sauerwein. *Principles and Roots of Neutron Capture Therapy*, pages 1–16. Springer Berlin Heidelberg, 2012.

[21] G. A.P. Cirrone, L. Manti, D. Margarone, G. Petringa, L. Giuffrida, A. Minopoli, A. Picciotto, G. Russo, F. Cammarata, P. Pisciotta, F. M. Perozziello, F. Romano, V. Marchese, G. Milluzzo, V. Scuderi, G. Cuttone, and G. Korn. First experimental proof of proton boron capture therapy (pbct) to enhance protontherapy effectiveness. *Scientific Reports*, 8, 12 2018.

[22] Pavel Bláha, Chiara Feoli, Stefano Agosteo, Marco Calvaruso, Francesco Paolo Cammarata, Roberto Catalano, Mario Ciocca, Giuseppe Antonio Pablo Cirrone, Valeria Conte, Giacomo Cuttone, Angelica Facoetti, Giusi Irma Forte, Lorenzo Giuffrida, Giuseppe Magro, Daniele Margarone, Luigi Minafra, Giada Petringa, Gaia Pucci, Va-

lerio Ricciardi, Enrico Rosa, Giorgio Russo, and Lorenzo Manti. The proton-boron reaction increases the radiobiological effectiveness of clinical low- and high-energy proton beams: Novel experimental evidence and perspectives. *Frontiers in Oncology*, 11, 6 2021.

[23] Juris Meija, Tyler B. Coplen, Michael Berglund, Willi A. Brand, Paul De Bièvre, Manfred Gröning, Norman E. Holden, Johanna Irrgeher, Robert D. Loss, Thomas Walczyk, and Thomas Prohaska. Isotopic compositions of the elements 2013 (iupac technical report), 3 2016.

[24] Villads Lundsteen Jacobsen, Jacob G. Johansen, Hans O.U. Fynbo, and Niels Bassler. A monte carlo study of high-let particle production in proton boron therapy. *European Physical Journal Plus*, 138, 7 2023.

[25] Harald H. Rossi and Marco Zaider. *Microdosimetry and Its Applications*. Springer Berlin Heidelberg, 1996.

[26] L. A. Braby, V. Conte, M. Dingfelder, D. T. Goodhead, L. S. Pinsky, A. B. Rosenfeld, T. Sato, A. J. Waker, S. Guatelli, G. Magrin, H.-G. Menzel, M.-E. Brandan, and P. Olko. Icru report 98, stochastic nature of radiation interactions: Microdosimetry. *Journal of the ICRU*, 23:1–168, 12 2023.

[27] Eric J Hall, Amato J Giaccia, et al. Radiobiology for the radiologist. *Int J Radiat Oncol Biol Phys*, 66(627):10–1016, 2006.

[28] Harald Paganetti, Andrzej Niemierko, Marek Ancukiewicz, Leo E Gerweck, Michael Goitein, Jay S Loeffler, and Herman D Suit. Relative biological effectiveness (rbe) values for proton beam therapy. Technical report, 2002.

[29] Yuki Kase, Tatsuaki Kanai, Yoshitaka Matsumoto, Yoshiya Furusawa, Hiroyuki Okamoto, Toru Asaba, Makoto Sakama, and Hiroshi Shinoda. Microdosimetric measurements and estimation of human cell survival for heavy-ion beams. Technical report, 2006.

[30] Kellerer and AM. The theory of dual radiation action, current topics. *Radiat. Res. Quarterly*, 8:73, 1972.

[31] Michael Scholz and Gerhard Kraft. Track structure and the calculation of biological effects of heavy charged particles. *Advances in Space Research*, 18(1-2):5–14, 1996.

[32] Roland B. Hawkins. A statistical theory of cell killing by radiation of varying linear energy transfer. *Radiation Research*, 140:366, 12 1994.

[33] T. Loncol, V. Cosgrove, J.M. Denis, J. Gueulette, A. Mazal, H.G. Menzel, P. Pihet, and R. Sabattier. Radiobiological effectiveness of radiation beams with broad let spectra: Microdosimetric analysis using biological weighting functions. *Radiation Protection Dosimetry*, 52:347–352, 4 1994.

[34] James F. Ziegler, M.D. Ziegler, and J.P. Biersack. Srim – the stopping and range of ions in matter (2010). *Nuclear Instruments and Methods in Physics Research Section B: Beam Interactions with Materials and Atoms*, 268:1818–1823, 6 2010.

[35] Alessio Parisi, Tatsuhiko Sato, Yusuke Matsuya, Yuki Kase, Giulio Magrin, Claudio Verona, Linh Tran, Anatoly Rosenfeld, Anna Bianchi, Pawel Olko, Lara Struelens, and Filip Vanhavere. Development of a new microdosimetric biological weighting function for the rbe10 assessment in case of the v79 cell line exposed to ions from 1h to 238u. *Physics in Medicine and Biology*, 65, 11 2020.

[36] S. Agostinelli, J. Allison, K. Amako, J. Apostolakis, H. Araujo, P. Arce, M. Asai, D. Axen, S. Banerjee, G. Barrand, F. Behner, L. Bellagamba, J. Boudreau, L. Broglia, A. Brunengo, H. Burkhardt, S. Chauvie, J. Chuma, R. Chytracek, G. Cooperman, G. Cosmo, P. Degtyarenko, A. Dell'Acqua, G. Depaola, D. Dietrich, R. Enami, A. Feliciello, C. Ferguson, H. Fesefeldt, G. Folger, F. Foppiano, A. Forti, S. Garelli, S. Giani, R. Giannitrapani, D. Gibin, J.J. Gómez Cadenas, I. González, G. Gracia Abril, G. Greeniaus, W. Greiner, V. Grichine, A. Grossheim, S. Guatelli, P. Gumplinger, R. Hamatsu, K. Hashimoto, H. Hasui, A. Heikkinen, A. Howard, V. Ivanchenko, A. Johnson, F.W. Jones, J. Kallenbach, N. Kanaya, M. Kawabata, Y. Kawabata, M. Kawaguti, S. Kelner, P. Kent, A. Kimura, T. Kodama, R. Kokoulin, M. Kossov, H. Kurashige, E. Lamanna, T. Lampén, V. Lara, V. Lefebure, F. Lei, M. Liendl, W. Lockman, F. Longo, S. Magni, M. Maire, E. Medernach, K. Minamimoto, P. Mora de Freitas, Y. Morita, K. Murakami, M. Nagamatu, R. Nartallo, P. Nieminen, T. Nishimura, K. Ohtsubo, M. Okamura, S. O'Neale, Y. Oohata, K. Paech, J. Perl, A. Pfeiffer, M.G. Pia, F. Ranjard, A. Rybin, S. Sadilov, E. Di Salvo, G. Santin, T. Sasaki, N. Savvas, Y. Sawada, S. Scherer, S. Sei, V. Sirotenko, D. Smith, N. Starkov, H. Stoecker, J. Sulkimo, M. Takahata, S. Tanaka, E. Tcherniaev, E. Safai Tehrani, M. Tropeano, P. Truscott, H. Uno, L. Urban, P. Urban, M. Verderi, A. Walkden, W. Wander, H. Weber, J.P. Wellisch, T. Wenaus, D.C. Williams, D. Wright, T. Yamada, H. Yoshida, and D. Zschiesche. Geant4—a simulation toolkit. *Nuclear Instruments and Methods in Physics Research Section A: Accelerators, Spectrometers, Detectors and Associated Equipment*, 506:250–303, 7 2003.

[37] J. Allison, K. Amako, J. Apostolakis, H. Araujo, P. Arce Dubois, M. Asai,

G. Barrand, R. Capra, S. Chauvie, R. Chytracek, G.A.P. Cirrone, G. Cooperman, G. Cosmo, G. Cuttone, G.G. Daquino, M. Donszelmann, M. Dressel, G. Folger, F. Foppiano, J. Generowicz, V. Grichine, S. Guatelli, P. Gumplinger, A. Heikkinen, I. Hrivnacova, A. Howard, S. Incerti, V. Ivanchenko, T. Johnson, F. Jones, T. Koi, R. Kokoulin, M. Kossov, H. Kurashige, V. Lara, S. Larsson, F. Lei, O. Link, F. Longo, M. Maire, A. Mantero, B. Mascialino, I. McLaren, P. Mendez Lorenzo, K. Minamimoto, K. Murakami, P. Nieminen, L. Pandola, S. Parlati, L. Peralta, J. Perl, A. Pfeiffer, M.G. Pia, A. Ribon, P. Rodrigues, G. Russo, S. Sadilov, G. Santin, T. Sasaki, D. Smith, N. Starkov, S. Tanaka, E. Tcherniaev, B. Tome, A. Trindade, P. Truscott, L. Urban, M. Verderi, A. Walkden, J.P. Wellisch, D.C. Williams, D. Wright, and H. Yoshida. Geant4 developments and applications. *IEEE Transactions on Nuclear Science*, 53:270–278, 2 2006.

[38] J. Allison, K. Amako, J. Apostolakis, P. Arce, M. Asai, T. Aso, E. Bagli, A. Bagulya, S. Banerjee, G. Barrand, B.R. Beck, A.G. Bogdanov, D. Brandt, J.M.C. Brown, H. Burkhardt, Ph. Canal, D. Cano-Ott, S. Chauvie, K. Cho, G.A.P. Cirrone, G. Cooperman, M.A. Cortés-Giraldo, G. Cosmo, G. Cuttone, G. Depaola, L. Desorgher, X. Dong, A. Dotti, V.D. Elvira, G. Folger, Z. Francis, A. Galoyan, L. Garnier, M. Gayer, K.L. Genser, V.M. Grichine, S. Guatelli, P. Guèye, P. Gumplinger, A.S. Howard, I. Hřivnáčová, S. Hwang, S. Incerti, A. Ivanchenko, V.N. Ivanchenko, F.W. Jones, S.Y. Jun, P. Kaitaniemi, N. Karakatsanis, M. Karamitros, M. Kelsey, A. Kimura, T. Koi, H. Kurashige, A. Lechner, S.B. Lee, F. Longo, M. Maire, D. Mancusi, A. Mantero, E. Mendoza, B. Morgan, K. Murakami, T. Nikitina, L. Pandola, P. Paprocki, J. Perl, I. Petrović, M.G. Pia, W. Pokorski, J.M. Quesada, M. Raine, M.A. Reis, A. Ribon, A. Ristić Fira, F. Romano, G. Russo, G. Santin, T. Sasaki, D. Sawkey, J.I. Shin, I.I. Strakovsky, A. Taborda, S. Tanaka, B. Tomé, T. Toshito, H.N. Tran, P.R. Truscott, L. Urban, V. Uzhinsky, J.M. Verbeke, M. Verderi, B.L. Wendt, H. Wenzel, D.H. Wright, D.M. Wright, T. Yamashita, J. Yarba, and H. Yoshida. Recent developments in geant4. *Nuclear Instruments and Methods in Physics Research Section A: Accelerators, Spectrometers, Detectors and Associated Equipment*, 835:186–225, 11 2016.

[39] Berger M.J., Coursey J.S., Zucker M.A., and Chang J. Estar, pstar, and astar: Computer programs for calculating stopping-power and range tables for electrons, protons, and helium ions (version 2.0.1). [online] available: http://physics.nist.gov/star national institute of standards and technology, gaithersburg, md., 2017.

[40] P.D. Bradley, A.B. Rosenfeld, and M. Zaider. Solid state microdosimetry. *Nuclear*

Instruments and Methods in Physics Research Section B: Beam Interactions with Materials and Atoms, 184:135–157, 9 2001.

[41] Dušan Srdoč. Experimental technique of measurement of microscopic energy distribution in irradiated matter using rossi counters. *Radiation Research*, 43:302, 8 1970.

[42] Harald H. Rossi. *Energy Distribution in the Absorption of Radiation*, pages 27–85. 1967.

[43] Albrecht M. Kellerer. An assessment of wall effects in microdosimetric measurements. *Radiation Research*, 47:377, 8 1971.

[44] Anatoly B. Rosenfeld. Novel detectors for silicon based microdosimetry, their concepts and applications. *Nuclear Instruments and Methods in Physics Research, Section A: Accelerators, Spectrometers, Detectors and Associated Equipment*, 809:156–170, 2 2016.

[45] J. F. Dicello, H. I. Amols, M. Zaider, and G. Tripard. A comparison of microdosimetric measurements with spherical proportional counters and solid-state detectors. *Radiation Research*, 82:441, 6 1980.

[46] P. D. Bradley and A. B. Rosenfeld. Tissue equivalence correction for silicon microdosimetry detectors in boron neutron capture therapy. *Medical Physics*, 25:2220–2225, 11 1998.

[47] S. Guatelli, M. I. Reinhard, B. Mascialino, D. A. Prokopovich, A. S. Dzurak, M. Zaider, and A. B. Rosenfeld. Tissue equivalence correction in silicon microdosimetry for protons characteristic of the leo space environment. *IEEE Transactions on Nuclear Science*, 55:3407–3413, 12 2008.

[48] David Bolst, Susanna Guatelli, Linh T. Tran, Lachlan Chartier, Michael L.F. Lerch, Naruhiro Matsufuji, and Anatoly B. Rosenfeld. Correction factors to convert microdosimetry measurements in silicon to tissue in 12c ion therapy. *Physics in Medicine and Biology*, 62:2055–2069, 2 2017.

[49] Linh T. Tran, Lachlan Chartier, Dale A. Prokopovich, David Bolst, Marco Povoli, Anand Summanwar, Angela Kok, Alex Pogossov, Marco Petasecca, Susanna Guatelli, Mark I. Reinhard, Michael Lerch, Mitchell Nancarrow, Naruhiro Matsufuji, Michael Jackson, and Anatoly B. Rosenfeld. Thin silicon microdosimeter utilizing 3-d mems fabrication technology: Charge collection study and its application in mixed radiation fields. *IEEE Transactions on Nuclear Science*, 65:467–472, 1 2018.

[50] Linh T. Tran, David Bolst, Benjamin James, Vladimir Pan, James Vohradsky, Stefania Peracchi, Lachlan Chartier, Emily Debrot, Susana Guatelli, Marco Petasecca, Michael Lerch, Dale Prokopovich, Željko Pastuović, Marco Povoli, Angela Kok, Taku Inaniwa, Sung Hyun Lee, Naruhiro Matsufuji, and Anatoly B. Rosenfeld. Silicon 3d microdosimeters for advanced quality assurance in particle therapy. *Applied Sciences*, 12:328, 12 2021.

[51] Carina Höglund, Jens Birch, Ken Andersen, Thierry Bigault, Jean Claude Buffet, Jonathan Correa, Patrick Van Esch, Bruno Guerard, Richard Hall-Wilton, Jens Jensen, Anton Khaplanov, Francesco Piscitelli, Christian Vettier, Wilhelmus Vollenberg, and Lars Hultman. B 4c thin films for neutron detection. In *Journal of Applied Physics*, volume 111, 5 2012.

[52] James Vohradsky, Susanna Guatelli, Jeremy A. Davis, Linh T. Tran, and Anatoly B. Rosenfeld. Evaluation of silicon based microdosimetry for boron neutron capture therapy quality assurance. *Physica Medica*, 66:8–14, 10 2019.

[53] Linh T. Tran, David Bolst, Susanna Guatelli, Alex Pogossov, Marco Petasecca, Michael L. F. Lerch, Lachlan Chartier, Dale A. Prokopovich, Mark I. Reinhard, Marco Povoli, Angela Kok, Vladimir L. Perevertaylo, Naruhiro Matsufuji, Tatsuaki Kanai, Michael Jackson, and Anatoly B. Rosenfeld. The relative biological effectiveness for carbon, nitrogen, and oxygen ion beams using passive and scanning techniques evaluated with fully 3d silicon microdosimeters. *Medical Physics*, 45:2299–2308, 5 2018.

[54] James Vohradsky, Linh T. Tran, Susanna Guatelli, Lachlan Chartier, Charlot Vandevoorde, Evan Alexander de Kock, Jaime Nieto-Camero, David Bolst, Stefania Peracchi, Carina Höglund, and Anatoly B. Rosenfeld. Response of soi microdosimeter in fast neutron beams: experiment and monte carlo simulations. *Physica Medica*, 90:176–187, 10 2021.

[55] Carmen Jacobs. Simulation of a proton beam through a phantom of water using geant4. Technical report.

[56] Francis A. Cucinotta and Sungmin Pak. Isotopic production cross sections in proton-16o and proton-12c interactions for energies from 10 mev/u to 100 gev/u. *Nuclear Instruments and Methods in Physics Research Section B: Beam Interactions with Materials and Atoms*, 534:26–34, 1 2023.

[57] Uwe Schneider and Roger Hälg. The impact of neutrons in clinical proton therapy. *Frontiers in Oncology*, 5, 10 2015.

[58] Roger Antoine Hälg and Uwe Schneider. Neutron dose and its measurement in proton therapy—current state of knowledge. *The British Journal of Radiology*, 93, 3 2020.

[59] Xueying Zhang, Yanbin Zhang, Fei Ma, Yongqin Ju, Liang Chen, Hongbin Zhang, Yanyan Li, Bo Wan, Jianguo Wang, and Honglin Ge. Neutron production for 250 mev protons bombarding on thick grain-made tungsten target. *European Physical Journal A*, 51, 8 2015.

[60] Zacharenia Nikitaki, Anastasia Velalopoulou, Vassiliki Zanni, Ioanna Tremi, Sophia Havaki, Michael Kokkoris, Vassilis G. Gorgoulis, Constantinos Koumenis, and Alexandros G. Georgakilas. Key biological mechanisms involved in high-let radiation therapies with a focus on dna damage and repair. *Expert Reviews in Molecular Medicine*, 24:e15, 3 2022.

[61] Pankaj Chaudhary, Thomas I. Marshall, Francesca M. Perozziello, Lorenzo Manti, Frederick J. Currell, Fiona Hanton, Stephen J. McMahon, Joy N. Kavanagh, Giuseppe Antonio Pablo Cirrone, Francesco Romano, Kevin M. Prise, and Giuseppe Schettino. Relative biological effectiveness variation along monoenergetic and modulated bragg peaks of a 62-mev therapeutic proton beam: A preclinical assessment. *International Journal of Radiation Oncology*Biology*Physics*, 90:27–35, 9 2014.

[62] M. J. Berger, J. S. Coursey, M. A. Zucker, and J. Chang. ESTAR, stopping power and range tables for electrons. `https://physics.nist.gov/Star`, 2005. National Institute of Standards and Technology, Gaithersburg, MD.

[63] Saeed Rajabpour, Hassan Saberi, Javad Rasouli, and Nasrollah Jabbari. Comparing geant4 physics models for proton-induced dose deposition and radiolysis enhancement from a gold nanoparticle. *Scientific Reports*, 12:1779, 2 2022.

[64] Geant4 Collaboration. Cuts per region — geant4 documentation, 2025.

[65] T. Sato, R. Watanabe, Y. Kase, C. Tsuruoka, M. Suzuki, Y. Furusawa, and K. Niita. Analysis of cell-survival fractions for heavy-ion irradiations based on microdosimetric kinetic model implemented in the particle and heavy ion transport code system. *Radiation Protection Dosimetry*, 143:491–496, 2 2011.

[66] Aimee McNamara, Henning Willers, and Harald Paganetti. Modelling variable proton relative biological effectiveness for treatment planning. *The British Journal of Radiology*, 93, 3 2020.

[67] Nicholas Koch, Wayne D Newhauser, Uwe Titt, Dan Gombos, Kevin Coombes, and George Starkschall. Monte carlo calculations and measurements of absorbed dose per

monitor unit for the treatment of uveal melanoma with proton therapy. *Physics in Medicine and Biology*, 53:1581–1594, 3 2008.

List of Figures

List of Tables